Università degli Studi di Catania
Scuola Superiore di Catania

International PhD in Nanoscience
XXIV Cycle

Emission and amplification of light from novel Si-based materials

Paolo Cardile

Tutor: Prof. Francesco Priolo
Coordinator: Prof. Maria Grazia Grimaldi

Triennium 2008/2011

Cover

Top left: *SEM picture of a photonic crystal, characterized by a triangular lattice. More details on the structural and electrical characterization of these artificial crystals can be found in section 3.3.*

Top right: *SEM picture of the electroluminescent device described in section 3.5. In the insets the image of the same device recorded by using an infrared camera in OFF and ON states are shown.*

Bottom left: *Schematic of the efficient quantum cutting process occurring in* $Y_{2-x}Er_xSi_2O_7$ *thin films. All the possible cross-relaxations are depicted. More details can be found in section 5.3.*

Bottom right: *Photoluminescence excitation spectroscopy performed on* $Yb_2Si_2O_7$, $Y_{2-x}Er_xSi_2O_7$ *and on* $Yb_{2-x}Er_xSi_2O_7$. *More details on this subject can be found in sections 5.5 and 5.6.*

Emission and amplification of light from novel Si-based materials
Paolo Cardile
PhD Thesis – Università degli studi di Catania – Scuola Superiore di Catania
Printed in Catania – 5th December 2011

Wissenschaft ohne Religion ist lahm,
Religion ohne Wissenschaft ist blind.
A. Einstein

La scienza senza la religione è zoppa,
la religione senza la scienza è cieca.
A. Einstein

Table of Contents

Chapter 5: Er compounds for optical amplifiers 125

1. Introduction

1.1 The fortune and the bottleneck of microelectronics

The fortune of microelectronics since its birth to nowadays is certainly due to Moore's Law, regulating the progressive miniaturization [1]: since the sixties of the last century, starting from the invention of the first transistor, in fact, a growing number of devices were implemented in the same silicon chip, by reducing continuously their size, with the aim of reducing the production costs and of increasing the performances of the chips.

The advances we assisted in the last fifty years allow now to have faster, smaller and cheaper microprocessors, thus improving remarkably the performances of our computers. This is the nanotechnology era, which deeply changed our daily life, since it gave us portable laptops or smart phones, permitting us to be connected to the world everywhere at any time.

The high performances of our modern devices are ruled not only by the miniaturization, but also by the multi-core systems. In fact, over the last three decades, the microprocessor performances scaled from devices that could perform tens of thousands of instructions per second to tens of billions of instructions per second in today's products. The architectures inside the microprocessors had to be changed, moving both towards the miniaturization of the single device and towards parallel cores, working together to improve the performances. Thanks to these multi-core systems, now we are approaching the era of Tera-scale computing. The next goal of a big company, like Intel, is in fact the realization of 10 Tera-instructions per second by 2015.

A particular representation of the recent progress of microelectronics is reported in fig. 1.1. Suppose that the number of components or transistors inside a microprocessor is represented by people. We can associate this number (as it was in 1970) to the people that can be placed in a big music hall, 2300 people. With time, the number grows more and more: year by year the population becomes too large and has to be inserted in a large stadium (1990) or in a big city like Tokyo (2000). Today we can imagine that the population is of the order of the Chinese one (about 1.3 billion inhabitants). Now suppose that all of these people are still confined in the original music hall. This gives the idea of the progressive scaling down of the device size during the decades. In fact the number of transistors in a chip increased by seven orders of magnitude, while the minimal feature of lithographic design has been reduced from 30 μm to 16 nm and this is the reason why we talk about nanoelectronics, nowadays.

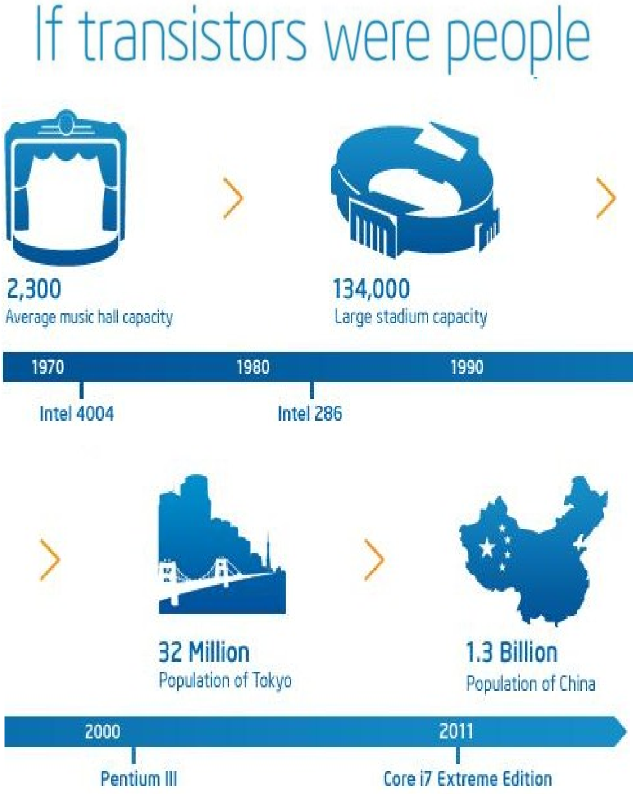

Figure 1.1: Miniaturization during the last forty years, according to the developments obtained by Intel. Adapted from [2].

However, as a consequence of the continuous reduction in size, much longer electrical connections are required in order to let all the components talk each other, and at a larger scale to link different microprocessors integrated in the same circuit board. The total length of the metallic interconnections is now of the order of 10 km in a micrometric area and therefore the wired network is so complicated that many levels of metal are required. This dramatic increase of the total length of the metallic circuitry leads to a consequent huge increase of signal delays, signal cross-talks and electromagnetic interferences causing power dissipation. This is the most important limitation for further developments.

Therefore the entire scientific community defines this problem as an electronic bottleneck, because soon it will be very hard to further reduce the minimal feature size.

A possible solution to this problem is represented by replacing the electrical interconnections with optical ones for linking chip-to-chip and board-to-board [3]. Photons, in fact, do not suffer the same problems of the metallic connections, having the possibility to travel at the light speed in the medium they pass through.

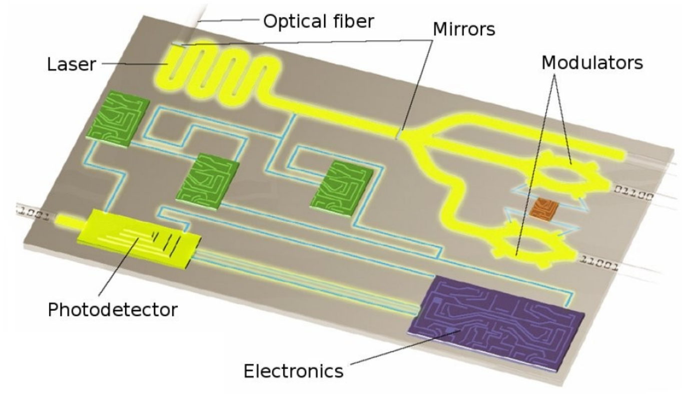

Figure 1.2: Schematic picture of an ideal optoelectronic device, in which optical and electrical elements cooperate in a single chip [3].

The success of optical fibers in long-range communications started off the research in the micrometric photonic circuitry. As it happens for the long-haul communication system, also at the micrometric scale the basic components necessary to have an optical network are a light source (a laser), a channel for carrying information (waveguides), a detector, a modulator of the signal. These devices must be integrated together in the same substrate in order to cooperate and make a working circuit, as depicted in fig. 1.2: this is the dream of integrated photonics. However these devices usually require different materials in order to optimize their functions, namely the generation, the control and the detection of photons.

The most common materials are direct band gap III-V or II-VI semiconductors for light emission and other materials, such as lithium niobate, for modulation, and they are not fully compatible with the Silicon technology. The realization of these components with Si-compatible materials is a very important issue, since this can provide a remarkable reduction of the production costs, the achievement of global diffusion and a compatibility with the electronic devices, which are currently integrated into the Silicon chips.

Nowadays the fabrication of passive devices, such as waveguides, splitters or multiplexers, is well developed on Silicon. However a necessary step forward is certainly the realization of active devices, like a laser, which is an efficient and coherent light source, or an optical amplifier.

Lasers and amplifiers are fundamental components and they are important for two independent reasons: the former is the generation of light-dark signals that can be associated to the logic values 1-0; the latter is the compensation of optical losses when light passes through passive components. Unfortunately Silicon is not an efficient light emitter, and this is a limitation that is hard to be overcome. Despite the achievement of optical gain [4, 5] or of a Raman-based stimulated emission [6, 7], a proper electrically-driven Silicon laser is still lacking. Some III-V nanolasers [8-11] are claimed to be the solution to the problem, since they can be actually grown on a Si substrate. However this is not going to be pursued by the current society, since the idea of making every optoelectronic device with Silicon is still the (cheapest and the) most fascinating.

Therefore it is necessary to find efficient strategies, in order to achieve the realization of new efficient active devices compatible with the Si-based technology: this is the object of this thesis.

1.2 Content of this thesis

The aim of this thesis is to study in detail novel Silicon-based nanostructured materials which allow to obtain the emission and the amplification of infrared light. In both fields we achieved interesting results: by using the advantages of Photonic Crystals, a prototype electroluminescent device is presented, with the highest spectral density and the lowest linewidth ever measured for Silicon at room temperature and at telecommunications wavelengths. Moreover, by exploiting the advantages of the rare earth compounds, a promising material is proposed for the realization of an optical planar amplifier.

The thesis is organized as follows:

In **Chapter 2** the physics of Photonic Crystals (PhC) will be introduced. These "artificial crystals" are characterized by a periodic distribution of the refractive index and were proposed in the late eighties of the last century. In this chapter the properties of PhC are described in detail by using Maxwell equations. It will be shown that PhC can efficiently control the propagation of light in the periodically patterned structure, acting with photons similarly to how the solid state crystals do with electrons. They can guide light and they can be used to realize cavities, in which light is trapped, travelling forward and backward. We present the ultimate ultra-high Q factor cavities that can be found in the recent literature, showing the advantages of different approaches in the design. In these cavities, which are actually cavities at the nanometer scale, it is possible to control also the spontaneous emission of an emitter placed inside them. This is the Purcell effect and it will be shown how it can be used for. Some recent PhC-based devices are also reported, showing that the many properties of the PhC can be used for third-harmonic generation or for the achievement of low-threshold lasing.

Chapter 3 will show how it is possible to obtain efficient light emission from nanopatterned Silicon. During the fabrication of SOI wafers, in fact, some defects are introduced by Hydrogen implantation. These defects are optically active and their photoluminescence can be extracted with a PhC structure. By treating the samples with a Hydrogen-rich plasma, a much stronger photoluminescence is obtained. This is due to a passivation of the Silicon surface and to the introduction of a further amount of defects in the Silicon slab. A discussion on the electrical conduction across a Photonic Crystals is then reported and finally the fabrication of the most efficient electrically-driven nanolight source in Silicon ever registered is described. This source works at room temperature and at telecommunication wavelengths. The measured linewidth and the spectral density of our light emitting device are seriously comparable with those of III-V nanolasers, working at cryogenic temperatures. We believe that this is going to be a milestone in the future story of Si-based photonics.

On the other hand, the second part of the thesis will be focused on the light amplification at 1.54 μm, by making use of erbium, a rare earth ion that is characterized by a radiative transition exactly at this wavelength.

In **Chapter 4** it will be discussed why this wavelength (and erbium, consequently) is so important and at the same time all the problems of incorporating erbium in a silicon based material will be reviewed. Among these problems, clustering and Er-Er interactions are described in detail. A strategy to improves the number of optically active Er ions is reported, by making use of Er compounds, such as oxides and silicates, in which the Er concentration can be varied continuously from the typical dopant regimes ($\sim 10^{19}$ Er/cm^3) up to the compound values ($\sim 10^{22}$ Er/cm^3).

In **Chapter 5**, the last chapter, it will be shown how it is possible to incorporate a large amount of erbium in Er-based materials, namely Y-Er disilicate and Yb-Er disilicate, grown by sputtering. These materials are studied in detail, by performing a complex structural characterization, with Rutherford Backscattering Spectrometry and X-ray Diffraction Analyses. The optical properties of these materials are also studied extensively. We demonstrate that Y-Er silicate is a very interesting material with good properties for applications in photovoltaics, being characterized by the occurrence of a quantum cutting phenomenon. Yb-Er disilicate, on the other hand, is more advantageous for light amplification at 1.54 μm. In this compound a strong energy transfer from Yb to Er is demonstrated, with noticeable efficiencies. This silicate is in fact proposed as a very promising material for realizing a planar amplifier onto a Silicon substrate.

References

[1] G. E. Moore, Electronics **38** (1965).
[2] Intel website www.intel.com
[3] M. Paniccia and S. Koehl, IEEE Spectrum **42**, 38 (2005).
[4] S. G. Cloutier, P. A. Kossyrev and J. Xu, Nat. Mater. **4**, 887 (2005).
[5] L. Pavesi, L. Dal Negro, C. Mazzoleni, G. Franzò and F. Priolo, Nature **408**, 440 (2000).
[6] H. Rong, A. Liu, R. Jones, O. Cohen, D. Hak, R. Nicolaescu, A. Fang and M. Paniccia, Nature **433**, 292 (2005).
[7] H. Rong, R. Jones, A. Liu, O. Cohen, D. Hak, A. Fang and M. Paniccia, Nature **433**, 725 (2005).
[8] H. Altug, D. Englund and J. Vuckovic, Nature Phys. **2**, 484 (2006).
[9] A. Tandaechanurat, S. Ishida, D. Guimard, M. Nomura, S. Iwamoto and I. Arakawa, Nature Phot. **5**, 91 (2010).
[10] B. Ellis, M. A. Mayer, G. Shambat, T. Sarmiento, J. Harris, E. E. Haller and J. Vuckovic, Nature Phot. **5**, 297 (2011).
[11] R. Chen, T.-T. D. Tran, K. W. Ng, W. S. Ko, L. C. Chuang, F. G. Sedgwick and C. Chang-Hasnain, Nature Phot. **5**, 170 (2011).

2. Photonic crystals

Photonic crystals are artificial structures in which photons behave as electrons do in a solid state crystal. They are characterized by a periodic distribution of the refractive index in one, two or three dimensions. It has been demonstrated that it is actually possible to engineer these structures, in order to have a complete control of light. The equations regulating this property are Maxwell equations solved in this particular periodic medium.

By considering the analogy between electrons in a solid and photons in a photonic crystal, it is easy to understand the existence of a photonic band gap and all the properties coming from it. One of the most interesting effects regards the control of the spontaneous emission from two-dimensional photonic crystal slabs, and this is well exploited in many applications.

A further control of the spontaneous emission rate is achieved by realizing photonic crystal nanocavities: these cavities are characterized by a very high Q factor and a very small mode volume, thus being very promising for the occurrence of a strong Purcell effect, which significantly enhances the spontaneous emission rate.

It is possible to engineer the cavities, simply by modifying the local geometry of the photonic crystals. Therefore it is possible to have either a higher Q factor by gently confining the optical mode in the cavity or to have a stronger out-of-plane coupling, in order to optimize the light emission of a photonic crystal device. In any case a slight modification of the geometry is required, meaning that photonic crystals are very versatile for different kind of applications. Additionally some other properties of photonic crystal waveguides can be used, like the slow light effect, which increases the light-matter interaction by orders of magnitude, thus enhancing non linear effects like visible third harmonic generation in Silicon.

Finally some photonic crystals-based lasers can be realized with low lasing threshold and very high modulation rates. All these lasers generally work with III-V semiconductors. The new challenge is then to demonstrate an efficient light source in silicon. Are photonic crystals the right way to pursue this goal?

2.1 Molding the flow of light

One of the most fascinating subjects of the research in photonics during the last decades concerns the complete control of light by making use of Photonic Crystals (PhC). A crystal is a spatial arrangement of atoms, placed in well-defined position in a periodic way, according to specific patterns, called crystal lattices. A lattice is actually an infinite array of discrete points which appears to be exactly the same from whichever of the points the array is viewed. From the Quantum Mechanics point of view, it is possible to treat such crystals as periodic distributions of the Coulomb potential: this explains why electrons in a perfect crystal know exactly how to move, without hurting any atom in the lattice, being interpreted like waves.

Moreover the solid state semiconductor lattices can also forbid the propagation of some particular electronic waves. In fact by considering their dispersion relation, i.e. the function linking energy and momentum of electrons, some "electronic states" can be actually prohibited. These are the so-called semiconductor energy gaps, which separate the valence band and the conduction band and define an ensemble of forbidden electronic states. For Silicon, for instance, the diamond-like lattice allows to have an energy gap about 1.1 eV large at room temperature.

The deep knowledge of solid state physics allowed to perfectly understand how to control the electrical properties of semiconductors, thus opening the route to a progressive development in the microelectronic technology. Therefore in the eighties of the last century a new interesting idea came out, answering the question: is it possible to realize artificial materials in which photons are subjected to similar laws than those of electrons in crystals? In other words, is it possible to perfectly control the light propagation in a certain material? The answer is yes, as it will be discussed. Photonic crystals, in fact, do to photons what semiconductor crystals do to electrons, creating a situation in which photonic modes are not permitted [1].

2.1.1 Maxwell equations and PhC

In a PhC the periodic atomic Coulomb potential is replaced by a periodic dielectric function. In order to solve this problem from a mathematical point of view, it is possible to use Maxwell equations, instead of Quantum Mechanics. In fact Maxwell equations perfectly describe a physical system in which there is a defined distribution of dielectric functions. In the particular case of photonic crystals, this distribution is periodic, and it involves two media with a sufficient difference in the refractive index (i.e. in the dielectric constant).

The dielectric unit can be repeated either in one dimension (the quarter-wave stacks, for instance) or in two dimensions (the most used photonic crystals), or even in three dimensions (a woodpile structure is a famous artificial example, while opals are the most known three dimensional PhC existing in nature), as depicted in fig. 2.1.

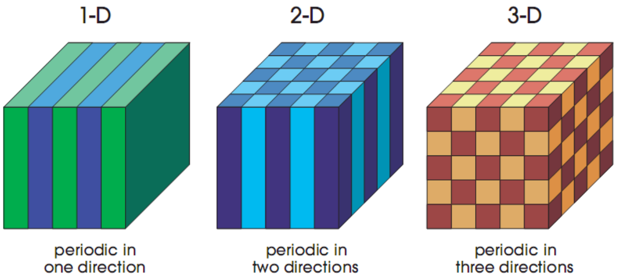

Figure 2.1: Pictures of different periodic structures in one, two or three dimensions [2].

The local Maxwell equations in a medium, expressed for each point in the space and for each instant, are well known [2, 3] and are here reported:

$$\begin{aligned}
&\nabla\cdot\mathbf{B} = \\
&\nabla\cdot\mathbf{D} = \\
&\nabla\times\mathbf{H} = \mathbf{J} + \frac{\partial\mathbf{D}}{\partial} \\
&\nabla\times\mathbf{E} = -\frac{\partial\mathbf{B}}{\partial}
\end{aligned} \tag{2.1}$$

where **E** and **H** are the microscopic electric and magnetic fields, **D** and **B** are the displacement and the magnetic induction fields, and finally ρ and **J** are the free charges and the current densities. We will consider the propagation in a mixed dielectric medium, whose structure does not vary with time and, without any sources (ρ=**0** and **J**=**0**). Moreover we will consider the simplest relation of proportionality between **D** and **E** and between **B** and **H**, assuming that the material is isotropic, without any dispersion, and transparent. In this specific case, we have that **D**(**r**) = $\varepsilon_0\varepsilon(\mathbf{r})\mathbf{E}(\mathbf{r})$ and **B**(**r**) = $\mu_0\mu(\mathbf{r})\mathbf{H}(\mathbf{r})$.

For almost all the dielectrics of interest, however, μ(**r**) = 1. By considering all these assumptions, it is possible to re-write the equations in the following way:

$$\begin{aligned}
&\nabla\cdot\mathbf{H}\ \mathbf{r} \quad = 0\\
&\nabla\cdot \quad \mathbf{r}\ \mathbf{E}\ \mathbf{r}, \mathrm{t})) = 0\\
&\nabla\times\mathbf{H}\ \mathbf{r} \quad = \varepsilon_0\varepsilon(\mathbf{r})\frac{\partial\mathbf{E}\ \mathbf{r}}{\partial}\\
&\nabla\times\mathbf{E}\ \mathbf{r} \quad - \quad \frac{\mathbf{H}\ \mathbf{r}}{\partial} -
\end{aligned} \qquad (2.2)$$

In general, the electric and the magnetic fields are complex functions of space and time. However, since the equations are linear, it is possible to separate the time dependence from space, by expanding the fields in harmonic modes. This is not a limitation, because it is known from the Fourier analysis that any function can be written as a linear combination of these modes. Therefore, by using the complex exponentials:

$$\begin{aligned}
&\mathbf{H}(\mathbf{r}, \mathrm{t}) = \mathbf{H}(\mathbf{r})e^{-}\\
&\mathbf{E}(\mathbf{r}, \mathrm{t}) = \mathbf{E}(\mathbf{r})e^{-}
\end{aligned} \qquad (2.3)$$

and by substituting them into Eq. (2.2), we obtain for the first two equations:

$$\begin{aligned}
&\nabla\cdot\mathbf{H}\ \mathbf{r} \quad 0\\
&\nabla\cdot \quad \mathbf{r}\ \mathbf{E}\ \mathbf{r}, \mathrm{t})) = 0
\end{aligned} \qquad (2.4)$$

These results mean that there are no sources in the material, either electric or magnetic. If the fields are plane waves, i.e. if the dependence on the space is **H**(**r**) = **a** exp(i**k**·**r**), then it means that the fields are transverse. The other curl equations, on the other hand, become:

$$\begin{aligned}&\nabla\times\mathbf{H}\ \mathbf{r} \qquad - \qquad \mathbf{r}\ \mathbf{E}(\mathbf{r})\\ &\nabla\times\mathbf{E}\ \mathbf{r} \qquad + \qquad \mathbf{H}\ \mathbf{r})\end{aligned} \qquad (2.5)$$

mutually relating the electric field and the magnetic one. It is possible however to decouple them, by dividing the first equation by ε(**r**) and by applying again the curl. In this way, by using also the second equation, it is possible to eliminate the electric field. Given that $\varepsilon_0\mu_0 = 1/c^2$, being c the light speed in the vacuum, we thus obtain:

$$\nabla\times\left(\frac{}{\mathbf{r}}\qquad \mathbf{H}\ \mathbf{r}\right)\left(\quad\right)\mathbf{H}\ \mathbf{r} \qquad (2.6)$$

This is the so-called master equation and it describes the behavior of the magnetic field. For a given ε(**r**), the master equation can be solved, thus finding the modes **H**(**r**) and the corresponding frequencies, by taking care of the transversality condition. After that it is possible to find also **E**(**r**), just by taking the curl of **H**(**r**) according to Eq. (2.5). In this case, however, **E**(**r**) is already transversal, since it is expressed as the curl of **H**(**r**), and the divergence of a curl is always zero.

This is a general discussion, arising just from generic considerations about a medium in which light is propagating. In the specific case of the photonic crystals, we already said that the refractive index is distributed in a periodic way. In other words, the dielectric function ε(**r**) is a periodic function of **r**. Let us have a look again at Eq. (2.6): the first term is nothing but an operator for the magnetic field: it consists in a curl, a multiplication and another curl. If the dielectric function is periodic, this operator keeps the spatial periodicity of ε(**r**), thus being a periodic operator. Therefore we can see that the master equation is analogous to the Schrödinger equation for the electrons in a crystal:

$$\left(\qquad\qquad\qquad \mathbf{r}\right)\ \mathbf{r}\qquad\quad \mathbf{r} \qquad (2.7)$$

where ψ is the electronic wave function, the first term in parenthesis is the kinetic energy operator, while V(**r**) is the periodic Coulomb potential. Note that solving the master equation is an eigenvalue problem, similar to that of Quantum Mechanics. The analogy is complete since, both for electrons and light, the eigenvalues are energies[1]. For the photons, these eigenvalues are the frequencies of the electromagnetic field, and the eigenfunctions are the fields themselves.

There are two main differences however: the first is that there is not any quantistic effect in the propagation of photons in a periodic medium. It is just a classical physical effect, though the mathematics lying beyond is similar. The second is that the master equation is scale invariant and this property comes from Maxwell equations: there is no a fundamental length scale and this is very important from the practical point of view. In fact it is always possible to rescale the system in order to have a certain eigenvalue [2].

All the solutions of the Schrödinger equation as a function of the momentum vector of the wave function permit to construct the band structure of the solid under investigation. From the same equations it is possible to justify the existence of the energy band gap for semiconductors and insulators. As it happens for semiconductors, this behavior can be seen also for photonic crystals. This property provides the opportunity to shape and mould the flow of light for photonic information technology.

By properly adjusting the photonic crystal structure, it is then possible to obtain a certain range of wavelengths for which photons cannot propagate in a photonic crystal. The existence of such photonic band gap materials in 3D was demonstrated in the early nineties [4-6], and the first experimental proof was found by using an array of holes drilled into a high refractive index material [6]. That centimetre-scale face-centred cubic artificial crystal, known also as Yablonovite[2], showed a stop band for the transmission of microwave radiation from 13 to 16 GHz, independently of the direction. Later on, the first structures working in the near IR (between 1.35 μm and 1.95 μm) were also demonstrated [7].

---

[1] Note that in the master equation, ω is an energy divided by $\hbar$.

[2] After the name of its inventor E. Yablonovitch.

Recently lasing was shown from a III-V semiconductors-based woodpile structure, i.e. an alternate sequence of GaAs thin layers (each containing line and space), with InAs quantum dots as active medium [8].

On the other hand, 2D PhC structures are much more interesting and we will show them in more details. The reason is that 2D artificial crystals are much easier to be fabricated, in particular thanks to the development of lithography and etching techniques. Additionally, lower dimensionality helps in modifying the crystals (for instance introducing defects deliberately) or in interfacing the PhC to any microphotonic device.

2.2 Photonic band structure in 2D PhC

A two dimensional PhC is characterized by an in-plane periodicity of the refractive index and by a light confinement in the third dimension, like a quantum well for electrons. A 2D PhC can be realized by making holes in a semiconductor material, by using electron beam lithography and a strong directional etching technique with high resolution. Such a material is then a sequence of ordered holes that can be arranged as reported in fig. 2.2, representing a schematic of a triangular lattice with a lattice parameter *a* and a hole radius *r* [2]; a SEM picture of the same lattice designed in AlGaAs is also shown [9].

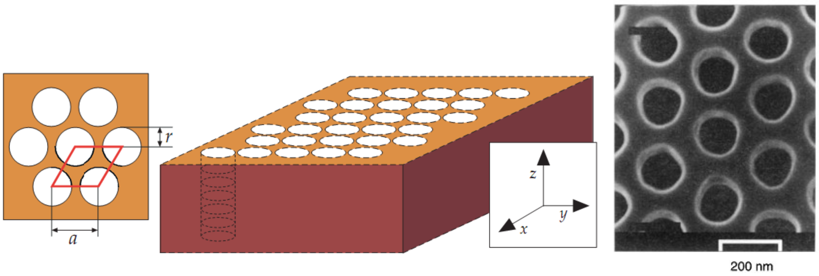

Figure 2.2: Example of two-dimensional PhC with a triangular lattice [2]. An SEM picture, showing the first attempt of using this lattice in AlGaAs is also reported [9].

In the case of 2D PhC, the master equation can be solved and the eigenfunction are characterized by the wave vector $\underline{k}$ and by a band index *n*, therefore we identify the modes as $\omega_n(\mathbf{k})$. Sometimes the frequency is expressed as a dimensionless ratio $\omega a/2\pi c$.

The comparison of two different lattices from the band gap point of view is reported in fig. 2.3. The top panel is the band structure of a square lattice of alumina rods (ε = 8.9), surrounded by air (ε = 1.0). The rods have a diameter of 0.74 mm and a length of 100 mm and are arranged in a square array with lattice constant a = 1.87 mm. This band structure was calculated (continuous lines in the graph) and experimentally measured (square points). The x axis shows the values of the in-plane wave vector $\mathbf{k}_{\parallel}$. Note that in the x axis some specific points are indicated: Γ, X, M. They correspond to the directions in the lattice $\mathbf{k}_{\parallel} = 0$, $\mathbf{k}_{\parallel} = \pi/a$, and $\mathbf{k}_{\parallel} = \pi/a + \pi/a$.

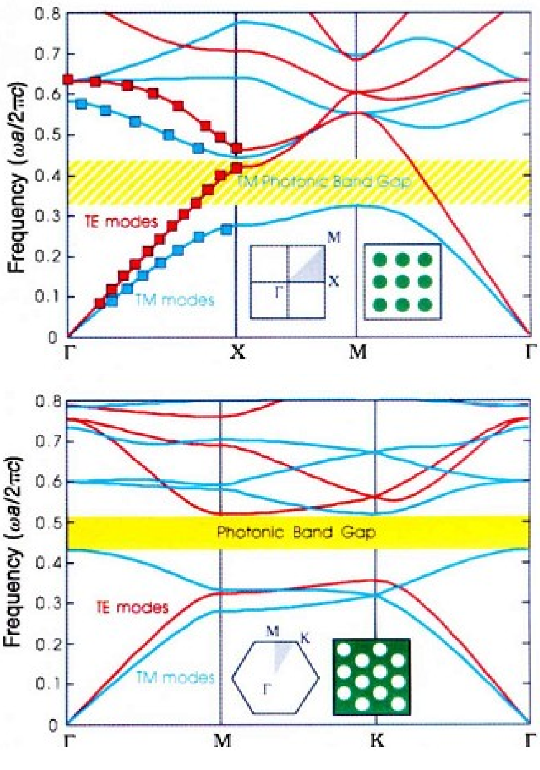

Figure 2.3: Band structure of an array of alumina columns surrounded by air in a square lattice distribution (top panel) and of a triangular lattice with holes of air in a dielectric (bottom panel) [10].

For both the components of the electromagnetic field, namely the transverse electric (TE) and the transverse magnetic (TM) modes[3], there is a perfect agreement between experiment and theory. Moreover it is clear that only for TM modes there is the existence of a large photonic band gap between the first band and the second one. This does not happen for TE modes. In fact, for the lowest TM band, the field is concentrated in the dielectric regions, while for the second band, it is concentrated in the air regions. By considered **k** fixed, for instance at the X point, the two associated frequencies are therefore noticeably splitted.

On the contrary, for the TE case, both the low band and the top band modes are significantly placed in the air, with a high frequency. This fact can be explained by considerations regarding the distribution of energy coming from Maxwell equations [2]. Exactly the opposite behavior is seen for a connected dielectric square lattice. Therefore TM band gaps are favoured in a lattice of isolated high-ε regions and TE gaps are favoured in a connected high-ε lattice.

In order to have a complete band gap photonic crystal, it is necessary to make a compromise on the geometry: the crystal needs to be connected but at the same time the high-ε regions must be practically isolated. An example of this system is the triangular lattice of air columns, as that shown in fig. 2.2. In fact for this system the band structure reported in fig. 2.3 (bottom panel) has a complete band gap for both TE and TM polarizations. In the region highlighted in yellow, where $\omega a/2\pi c$ is between 0.4 and 0.5, light cannot propagate in the medium, whatever is its propagation direction **k**.

Besides the lattice configuration, the other main factor that determines the properties of the band gap of a 2D PhC is the refractive index contrast. In general, the higher the refractive index contrast, the larger the band gap achievable.

---

[3] TE (TM) means that there is no electric (magnetic) field in the direction of propagation.

2.2.1 2D PhC slabs and control of the spontaneous emission

In this section we will show how it is important the existence of a photonic band gap (we will call it PBG, for the sake of simplicity).

In a two dimensional photonic crystal, light propagation in the orthogonal direction (with respect to the 2D periodicity) cannot be controlled by the photonic band gap effect, because no periodicity is registered in that direction. In order to use this dimensionality for feasible applications, a thin slab structure was suggested. This slab is a freestanding membrane being surrounded by air (or another low-index dielectric, eventually) and it is realized in order to achieve a strong optical confinement in the vertical direction.

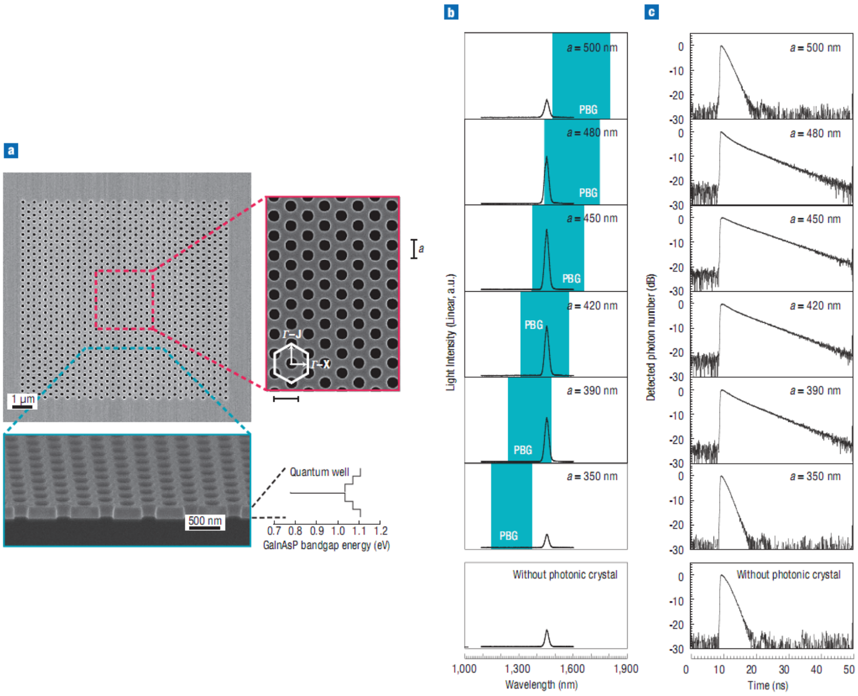

Figure 2.4: (a) SEM picture of a GaInAsP 2D photonic crystal slab. A 5 nm QW layer is inserted in the middle of the slab, being the active emitting layer. (b) Emission spectra for samples with lattice constant between 350 and 500 nm. The blue region denotes the PBG. (c) Time-resolved measurements for all the samples investigated. [11, 12].

Owing to this property it was demonstrated that such slabs successfully manage the manipulation of light, by controlling in particular spontaneous emission [11]. Noda and coworkers fabricated a GaInAsP 2D PhC slab (245 nm thick) structure with a single quantum well (QW) light emitting layer, as reported in the SEM pictures in fig. 2.4 (a) [12].

Many samples with the same triangular lattice but with a different lattice parameter a were realized. In all cases the holes radius is $r = 0.29a$. As shown in fig. 2.4 (b) the photonic band gap (denoted as PBG) shifts to larger wavelengths by increasing a. The lifetime of the excited carriers are also reported in panel (c) of the same figure. When the emission wavelength is inside the band gap ($a = 390 - 480$ nm) the lifetime increases (i.e. the emission probability decreases) compared with the lifetime without the PBG effect. At the same time the vertical emission peak increases significantly (see fig. 2.4 (b)). Therefore this particular geometry was remarkably able to reduce the in-plane spontaneous emission rate, while the light extraction in the vertical direction was enhanced. Therefore when the spontaneous emission is inhibited by the PBG effect, the energy is saved and re-distributed in other mechanisms, such as the emission out-of-plane. This effect is very useful for many applications in photonics, such as illuminations or solar cells.

We can then conclude that a PhC slab is able itself to inhibit spontaneous emission, just because of its PBG. Recent experiments have demonstrated that it is possible to suppress spontaneous emission by roughly the theoretical limit (~15 times) [13].

2.3 Point defects in a PhC: nanocavities for photons

It is well known for semiconductors that, once point defects are inserted in the lattice, new states appear in the semiconductor band gap, associated to the breaking of the symmetry in some points of the crystal. This behaviour can be seen also for photonic crystals. The perturbation of a point defect, deliberately introduced in the artificial crystal, is responsible of the creation of localized modes, having a frequency in the forbidden band gap. This perturbation can be realized for instance by changing the dielectric constant of a column in a PhC realized by identical columns surrounded by air. Another possible configuration is realized by avoiding to make holes in a lithographically defined PhC, in which columns of air are etched down in a semiconductor.

The as-created photonic mode cannot propagate in the rest of the crystal, because there it falls inside the band gap: therefore this defect-related mode is spatially localized where the physical defect lies. So the mode decays exponentially and evanescently out of the defect. These modes are localized in the *xy* plane, and they are extended in *z*. The boundaries of the defect actually act as mirrors and therefore the point defect is nothing but a cavity for the photons, because light cannot escape from it.

The two most important features of a cavity are the Q factor, that is the energy loss per cycle divided by the energy stored inside, and the modal volume V_{eff}, i.e. a measure of the spatial extent and energy density of the mode. The Q factor represents how strong is the confinement inside the cavity.

Light confinement in a generic photonic cavity is a very important topic for several applications, since it can enhance the electron-photon interaction [14] or non linear optics [15] or the occurrence of other quantum effects, useful for quantum information technology [16]. Very high Q factors (of the order of $\sim 10^8$) were measured in micrometric ring resonators [17], but in that case the dimension of the ring is much larger than the wavelengths used. Photonic crystals are very interesting because they can offer a very high Q with very small modal volumes, of the order of a cubic half-wavelength in the host material. Therefore they allow to strongly reduce the dimension of the cavity, without suffering scattering losses, as it would happen by scaling down the dimension of a microring.

Fig. 2.5 reports two SEM pictures: one is referred to a silica microring resonator with a 10^8 Q factor [17], while the second is a PhC cavity [18]. They are reported together in order to see effectively from the markers which is their difference in size. This particular PhC cavity is realized in InAsP by grading the size of the holes in order to induce the formation of a point defect in the crystal. This was the first demonstration that the Q factor of PhC cavities can be in excess of 10^4 [18].

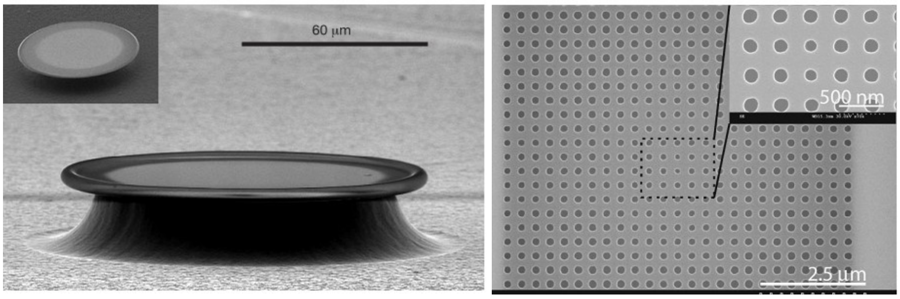

Figure 2.5: SEM pictures representing a ultra-high Q microring resonator [17] and a PhC cavity [18]. Note the difference of the two markers.

At a first glance it would seems that microrings are much more efficient cavities. On the other hand the mode volume in the case of PhC is much smaller. This is crucial, because the ratio Q/V_{eff} determines the strength of the various cavity interactions, as it will be pointed out later. In this case, PhC cavities work better than microring resonators and, being very small, they enable large-scale integration.

2.3.1 The Purcell effect

We have seen previously that the PBG can itself provide a control of the spontaneous emission rate. However another fundamental and more powerful mechanism that is able to control spontaneous emission is the Purcell effect. This effect can be observed when an excited atom is put inside a photonic cavity [19]. In order to explain this effect, let us start from its definition: spontaneous emission occurs when an emitter relaxes from one of its excited states to its ground state, by photon emission into an optical mode that is not occupied by another photon. The rate of this process is determined by Quantum Mechanics, and in particular by using the framework of the Fermi's golden rule, which can be expressed as:

$$\Gamma_{i,f} \quad \frac{2\pi}{\hbar}\left|\langle f|\hat{H}_{I}|i\rangle\right|^{2}\rho(\omega) \tag{2.8}$$

being $\Gamma_{i,f}$ the transition probability that the system in an initial state $|i\rangle$ moved to a final state $|f\rangle$, thanks to the interaction term of the Hamiltonian describing the system, $\hat{H}_i$. The last term, $\rho(\omega)$, is the density of the final states, the number of states per unit of energy and it depends on the energy (or on the frequency ω separating the initial and the final states). This equation comes from the time-dependent perturbation theory in Quantum Mechanics.

Unfortunately, spontaneous emission is in many cases troublesome, since it limits the performance of many devices. For instance, lasers are coherent light sources and when in the active medium a spontaneous emission is not coupled to the lasing modes the lasing threshold becomes higher and there is also some undesired noise. These problems are the basis of the research on how to control and manipulate spontaneous emission in photonic crystals-based systems. We will show now how a photonic cavity can do this.

The volume-normalized mode density $g(\omega)$ (that is $\rho(\omega)/V$) is proportional to ω^2, according to [20]:

$$g_f(\omega) = \frac{\omega^2}{\pi^2 c^3} \tag{2.9}$$

If the emitting atom is in resonance with the cavity, and if the linewidth of the emitter is entirely inside the cavity resonance, then the cavity restricts the modes to a spectral width $\Delta\omega$ and a volume V_{cav} and the density (in the case of Lorentzian shape) can be written as:

$$g_c(\omega) = \frac{2}{\pi}\frac{1}{\Delta\omega V}. \tag{2.10}$$

On the other hand the cavity is characterized by a quality factor Q, which can be written as $Q = \omega/\Delta\omega$. By substituting it in Eq. (2.10), we get:

$$g_c(\omega) = \frac{2Q}{\pi\omega V} \tag{2.11}$$

Therefore the mode density alteration caused by the cavity is given by the ratio g_c/g_f, that is:

$$\frac{g_c}{g_f} = \frac{2Q}{\pi\omega V}\cdot\frac{\pi^2 c^3}{\omega^2} = \frac{2\pi Q c^3}{\omega^3 V} = \frac{Q\lambda^3}{4\pi^2 V} \tag{2.12}$$

The maximum enhancement can be obtained if the emitting radiative dipole is oriented to have the strongest interaction with the cavity mode and this gives an additional factor 3. The enhancement factor, f_P, known also as Purcell factor, can be therefore written as:

$$f_P = \frac{{}^{3}}{4\pi^{2} V} \quad . \tag{2.13}$$

This shows that this factor, enhancing the spontaneous emission rate, is proportional to the ratio of Q factor divided by the cavity mode volume, meaning that PhC can be very promising in this field, having both a high Q and very small volume. Note that, with respect to the best ring resonators [17], PhC nanocavities can show a Q/V factor even two orders of magnitude larger [21-25], thanks to new and efficient designs.

Recently it was experimentally demonstrated that a relatively high f_P can reduce by orders of magnitude the lasing threshold, and this happened in different systems [26-28], but still not in the most important platform, that is Silicon of course. For Silicon, PhC cavities can be realized by using a Silicon-On-Insulator (SOI) wafer: with this kind of support, it is easy to realize slabs, since, after the etching of the holes in the silicon layer (about 200 nm thick), it is possible to membrane the PhC pattern, by means of chemical wet etching. We will show next how to fabricate some examples of PhC nanocavities, allowing a better and better confinement, namely L_n cavities (in particular L_3 with gentle confinement effect), heterostructure cavities, and cavities with local modulation of the holes in a line-defect.

2.3.2 L_n cavities and gentle confinement effect

L_n cavities are realized by removing n holes in the Γ-K direction in a triangular lattice of a PhC slab. In this particular case, by considering a perfect 2D crystal, the lacking of this n holes allows some states inside the band gap. This is the perturbation in the perfect repetition of the dielectric unit constituting the PhC cavity. Advance design techniques actually brought to the realization of different geometries of PhC cavities, in order to achieve a better and better Q/V ratio, thus candidating them for applications in large-scaled devices.

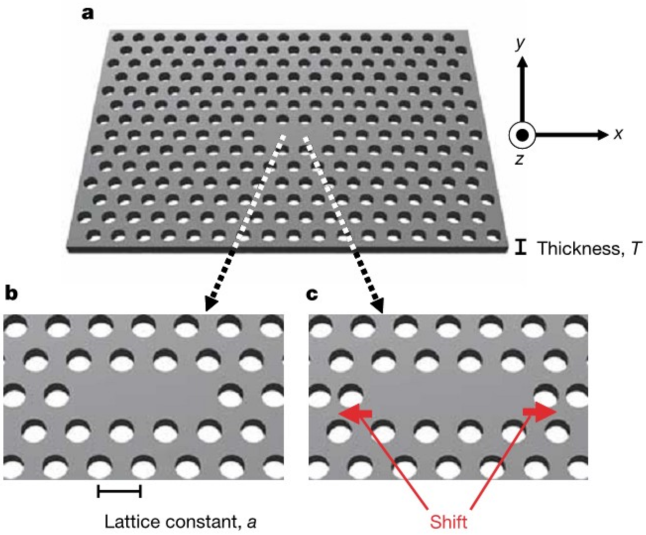

Figure 2.6: 2D PhC cavities realized by using a slab. (a) Schematic of the triangular lattice. (b) Starting cavity with three missing holes in the Γ-K direction and (c) cavity with the holes displaced at both edges [25].

An example of L_n cavities is shown in fig. 2.6 for n = 3: in this scheme an L_3 cavity is depicted, realized in a SOI-based PhC 250 nm thick slab. In this case just 3 holes are missing in the lattice, which is characterized by a = 420 nm and by a holes radius r = 120 nm [25]. With these parameters, the cavity is working around the telecommunication wavelength of 1.5 μm.

In this situation, the physical mechanism of total internal reflection (TIR), which works well in the description of microcavities, has to be reconsidered, since the photonic nanocavity has the dimension of the same order of magnitude of the wavelength. When light is confined in such small cavities, in fact, it consists of numerous plane wave components with different **k**-vectors (both in magnitude and direction). A triangular lattice PhC slab allows the TIR in all the in-plane directions, keeping also the vertical confinement, thanks to the air clad.

The TIR condition states that if the tangential component of **k**, $|\mathbf{k}_{||}|$, has an amplitude lower than $2\pi/\lambda_0$, then the wave can escape from the cavity to the air clad. On the other hand, when $|\mathbf{k}_{||}|$ is larger than $2\pi/\lambda_0$, then the wave is strongly confined in the cavity. Therefore in the former case people talk about a “weak confinement” or “leaky region”. The authors in ref. [25] have shown that the Fourier transformation spectrum of the cavity has a strong component in this leaky region. This is due to the fact that the electric field in the cavity can be expressed as the product of a certain sinusoidal wave function and an envelope function, determined by the cavity itself. If there is an abrupt change of this function, i.e. if the cavity edges behave like perfect mirrors, then this generates Fourier components in the leaky region, thus implying some radiation loss.

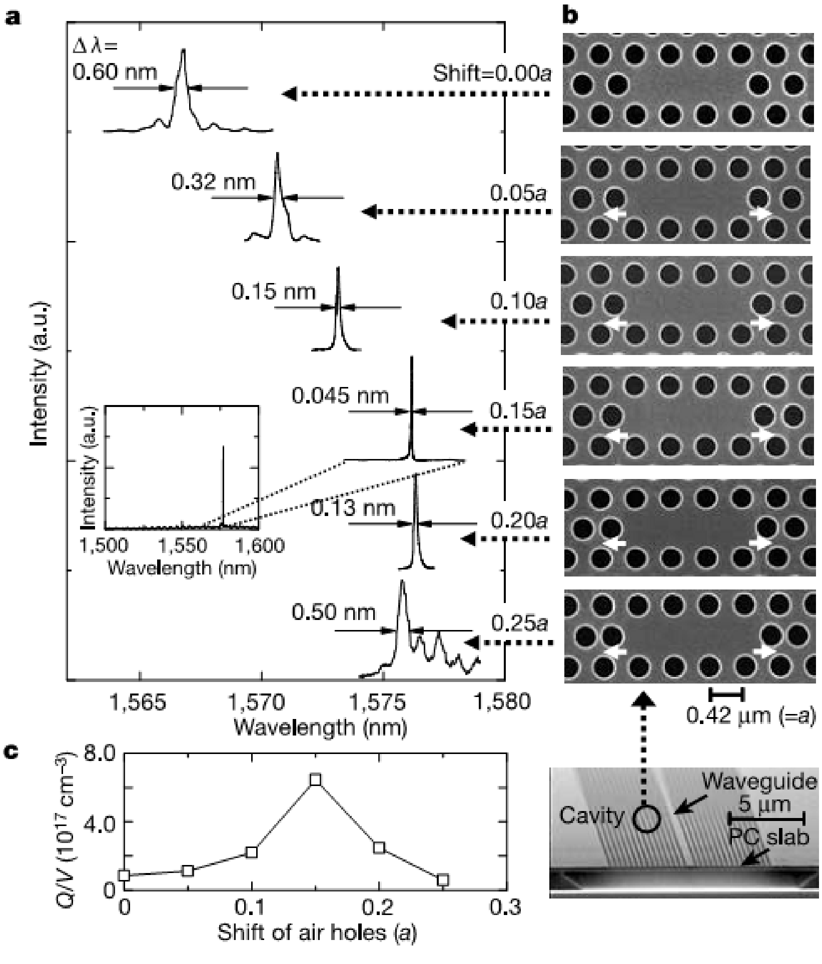

Figure 2.7: (a) Resonant spectra of cavities with different shift of the edge holes and (b) their SEM pictures. (c) Estimated Q/V values as a function of the shift [25].

The sharp change at the cavity edges can be modified, in order to make the confinement gentler. This was done by shifting the holes at both the edges of the cavity (see fig. 2.6 (c) compared to fig. 2.6 (b)). The simulation of the Fourier components has shown that actually in this way the electric field does not have components in the leaky region and the Q factor increases remarkably. In fact the Q factor was measured as a function of the displacement and the results are summarized in fig. 2.7. Panels (a) and (b) show resonant spectra and the corresponding SEM pictures. The width of the resonant peak is strongly modified by the displacement of the edges, and the minimum width observed was 0.045 nm (i.e. a Q factor of 45000). This is the result of an engineered structure that efficiently suppresses the out-of-slab leakage, thus permitting a stronger confinement of the light inside the cavity.

Fig 2.7 (c) reports the Q/V values as a function of the displacement: by considering the volume involved in such cavities, a Q/V as large as 6.4×10^{17} $/\mathrm{cm}^3$ was found, corresponding to $120000/\lambda^3$, two orders of magnitude higher than that reported for microring resonators [17]. These results clearly indicate the potentials of photonic crystals for enhancing the Purcell effect, for instance.

Another important point regards the single-mode operation: in fact the inset of fig. 2.7 (a) shows the resonant spectrum of the best cavity for a very wide wavelength range. This spectrum demonstrates that single-mode operation is possible for a broad range, and this can be useful for many applications in photonics, especially in telecommunications, due to the very low noise level that can be provided.

2.3.3 Heterostructure cavities

A very interesting design that was suggested very recently is the double heterostructure cavity [24]. The basic principle of this ultimate kind of cavities can be understood by looking at the band structure of the PhC.

The first step to realize a double heterostructure cavity is to design a line-defect in the 2D photonic crystal slab: this is done by removing an entire row of air holes. As it is clear from the picture in fig. 2.8 (a) this defect is nothing but a waveguide. In fact the photons propagating through this line cannot go inside the PhC, if their wavelength falls inside the PBG. This trick is very interesting because the confinement of this waveguide is provided by the forbidden states of the photonic band gap and it is very efficient. Light simply cannot escape from the line, because it does not have any allowed state out of it.

The PhC of the heterostructure is not uniform, because it is formed by three parts. We will refer to the first and the third parts as type I. This is a triangular lattice PhC of lattice constant a_1. In contrast, the second part is type II, being characterized by a deformed triangular lattice, in which the lattice constant is a_2, larger than a_1, in the waveguide direction, whilst it does not change in the Γ-M direction, in order to ensure a lattice-matching condition.

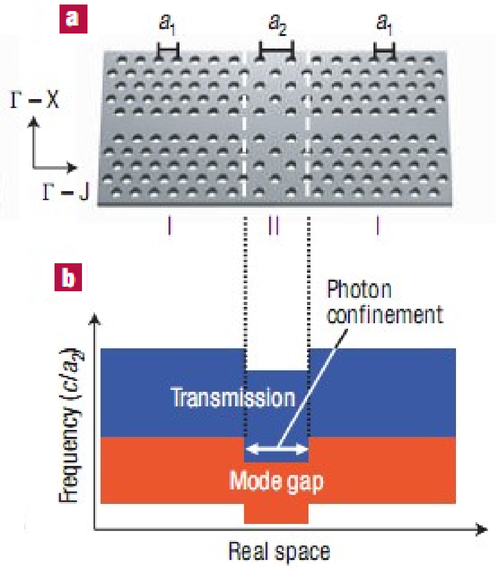

Figure 2.8: (a) Resonant spectra of cavities with different shift of the edge holes and (b) their SEM pictures. (c) Estimated Q/V values as a function of the shift. Adapted from [24].

Such a PhC structure ensures that photons with particular energies can exist only in the waveguide of PhC II. If this region II is small enough the frequencies that photons can take in this region become quantized, as it happens for electrons in quantum hole, and a photonic nanocavity is then realized, as depicted schematically in fig. 2.8 (b). It is very interesting to note that, by using this design, the photonic confinement is not directly provided by the PBG effect. It is a consequence of the mode-gap effect in the waveguide of PhC I, which is due to the mismatch in the lattice constant between the two regions.

Noda and coworkers realized a double heterostructure cavity with a_1 = 410 nm e a_2 = 420 nm and a slab $0.6a_2$ thick in SOI, by means of electron-beam lithography and reactive ion etching; finally the slab was obtained by membraning the cavity with HF. This device, shown in fig. 2.9 (a) in a SEM image, demonstrated the possibility to achieve Q factors of the order of 10^6, one order of magnitude higher than L_3 cavities with gentle confinement effect. The modal volume in this new cavity is about 1.2 $(\lambda_0/n)^3$ in the theoretical calculation, where λ_0 is the resonant wavelength in air and n is the refractive index of the slab.

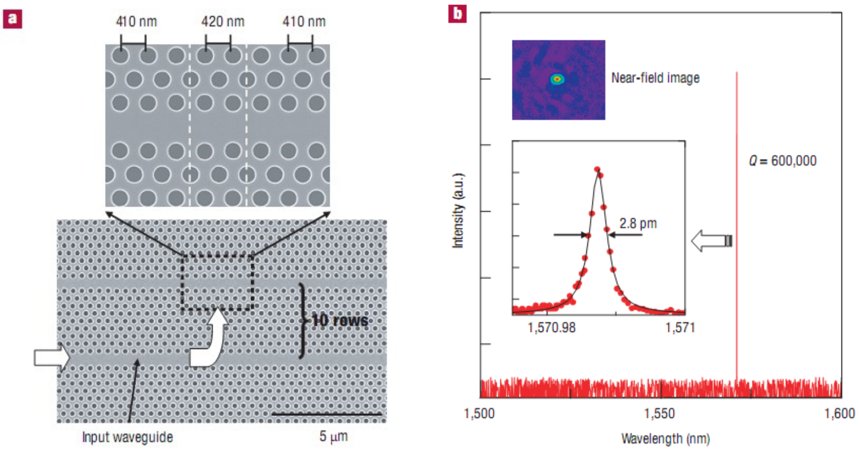

Figure 2.9: (a) A SEM picture of a double heterostructure cavity. In this case a_1 = 410 nm and a_1 = 420 nm. The input waveguide used to feed the cavity is also shown. (b) Resonant spectrum of the cavity. Note that this is a single-mode cavity with a very high Q factor. Adapted from [24].

Note that in order to inject photons in the cavity, an input waveguide had to be designed. The travelling photons in this waveguide are sucked by the cavity when they pass close to it, provided that their photonic state can fit in the cavity. This is the same mechanism used to feed microring resonators with tapered waveguides [17]. In the case of these innovative PhC cavities, the trapped light is characterized by a very narrow spectrum, with a line width as low as 2.8 pm (corresponding to Q = 600000), as reported in fig. 2.9 (b).

A further improvement of this structure can be done by exploiting again the gentle confinement effect. In order to make the edges gentler, an interesting possibility is to realize a multistep heterostructure, by adding another region PhC III, in between regions I and II, with an intermediate lattice parameter. A Q factor as high as 24 millions was calculated, thus demonstrating that new and more efficient innovative designs of PhC cavities are indeed achievable.

2.3.4 Local modulation of a line defect

The last scheme of PhC cavity that we want to briefly describe is the one that exhibits up to now the highest Q factors in SOI: this kind of cavities were obtained by properly produce a local modulation of a line defect. This intriguing design was proposed by Notomi group [21, 23] and it is also based, similarly to the previous case, on a line defect, a waveguide, in a PhC slab.

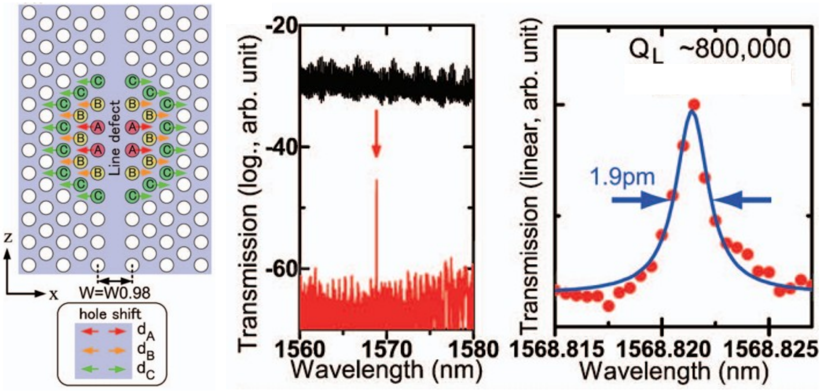

Figure 2.10: Schematic of PhC cavities realized by a waveguide width modulation (left) and transmission measurements (center, right) showing a ultra-high Q factor, as high as 80000. Adapted from [23].

In this case a waveguide is locally modified by performing a shift of some holes, in order to make a local confinement potential. Such a shift can be done with the aim of creating a sort of elliptic distribution of holes, as depicted in the schematic of fig. 2.10 (left panel). The waveguide width at the center of the cavity is increased by displacing the holes called A, B, C, by $d_A > d_B \geq d_C$.

The Q factor was measured by using a tunable laser diode coupled to an input waveguide with a fiber, and a photodetector coupled to an output waveguide. The transmission in such a structure reveals that the linewidth is as narrow as 1.9 pm, corresponding to a loaded Q value of about 800000, at about 1.5 μm (see fig. 2.10, center and right panel).

A key point of these structure is also that it is possible to have very high Q factors even with very thin barriers on the top/bottom sides of the cavity. Some air slots delimitating the PhC at 4 rows of holes already determine an experimental Q even larger than 10^6 [21].

This latter result was obtained by realizing the device depicted in fig. 2.11, where q is the number of the rows, i.e. 4 in this case, a = 420 nm, and ma is the total length of the air slot. By using this particular design a linewidth of just 1.2 pm was measured.

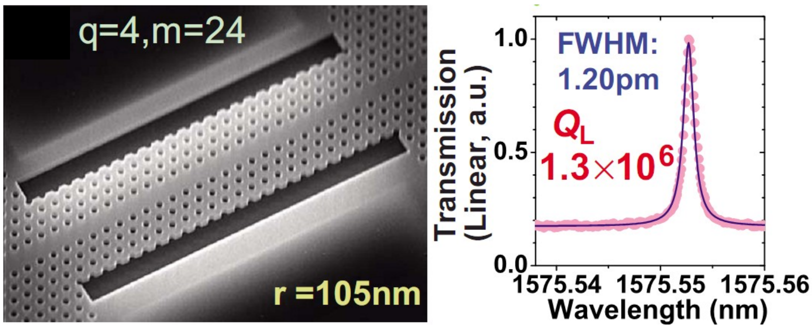

Figure 2.11: SEM picture of a nanocavity with q = 4 and m = 24 and measurement of the fundamental cavity resonance, showing a linewidth of 1.2 pm (a Q exceeding 10^6).

Therefore we can see how effective is a proper design in order to achieve Q factors really comparable with those of the microring resonators, but with a much smaller size and much smaller Q/V values.

2.3.5 Efficient light extraction out of a PhC cavity

The Q factor is a very important feature of the PhC cavities. The ultimate designs showed before demonstrate that it is possible to realize in practice ultra-high Q cavities with unprecedented (diffraction limited) volumes. It is worth reminding that the Q factor represents the number of travels forward and backward that photons can do in the cavity before coming out as losses. A high Q factor is fundamental, because it pushes up the Purcell effect. On the other hand, for practical applications on photonic chips, the off-plane radiation could be useful, in order to control both the in- and the out-coupling of light. This is important in emission experiments, such as photoluminescence from active media within the PhC pattern [29], or for optically pumping nanophotonic devices.

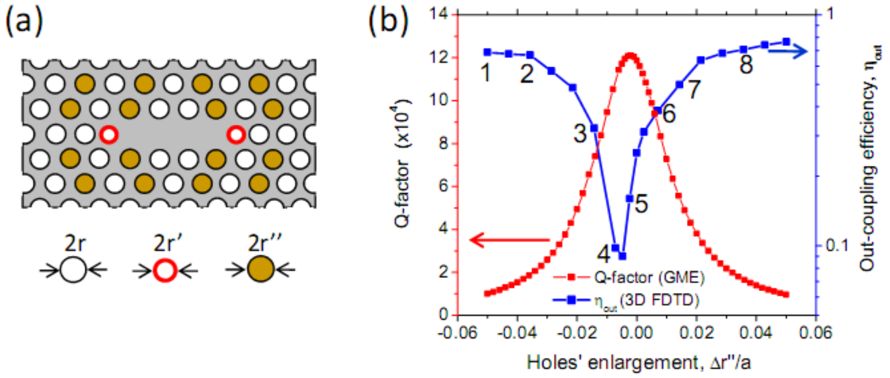

Figure 2.12: (a) Schematic of far-field optimized L_3 PhC cavity. Red holes are shifted and shrunk for the gentle confinement effect. Brown holes increase the out-of-plane coupling. (b) Calculated Q factor and out-coupling efficiency. The parameters are: thickness of the slab th = 220 nm, lattice constant a = 420 nm, holes' radius r = 0.265 a, red holes shift Δx = 0.16 a, red holes shrinking $\Delta r'$ = -0.06 a. Adapted from [30].

We have seen that by performing local adjustment of the geometric distribution of the holes the Q factor is clearly optimized, thanks to the reduction of the coupling to the radiative modes. The same idea can be exploited for another important purpose, that is to keep a relatively high Q factor, increasing at the same time the out-of-plane radiation in a controlled way. A systematic study regarding this issue is reported in ref. [30].

The physics behind the out-of-plane coupling is like that of a grating effect: the Fourier components of the field lying beyond the light cone, can be folded back around |**k**|=0 (i.e. close to the normal direction with respect to the cavity) by superimposing a lattice with twice the periodicity of the basic PhC structure [31]. This trick allows to have a good light extraction from the surface.

The idea of finding a trade-off between the Q factor and the out-of-plane coupling is depicted in fig. 2.12 for L_3 cavities. In fact the cavity is Q-optimized, by applying the gentle confinement effect: in the schematic of panel (a) the edge holes, highlighted in red, are shifted and shrunk, making gentler the cavity boundaries. In the same picture, note that the dark holes are distributed with a longitudinal lattice parameter that is actually $2a$, thus forming the grating. This second lattice is characterized by a different holes radius, and in panel (b) the trends of the calculated Q factor and out-coupling efficiency are plotted as a function of the enlargement $\Delta r''$ of these new holes (highlighted in brown in the picture) with respect to the original ones.

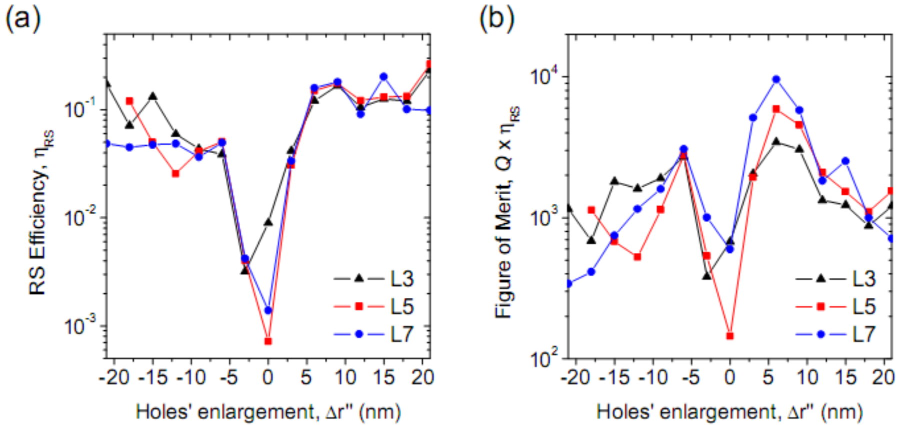

Figure 2.13: (a) Resonant scattering measurement from L3, L5 and L7 cavities, as a function of the enlargement. (b) Corresponding figure of merit, given by the product of the Q factor and of the resonant scattering efficiency [30].

L_n cavities were realized as air-bridges in SOI and the experimental results (see fig. 2.13 (a)), obtained by resonant scattering measurements [32] are comparable with the theory [30]. Additionally, a figure of merit given by the product Q times the efficiency is suggested (see fig. 2.13 (b)). The maximum value of this product, as a function of the holes enlargement represents the solution to the trade off between confinement (the Q) and extraction (the out-coupling efficiency), and it is at about $\Delta r'' = +6$ nm, with Q factors as high as 62000 [30]. This interesting study therefore indicates that it is possible to efficiently engineer the holes distribution in a PhC cavity, achieving a very high Q factor and at the same time a strong out-of-plane coupling efficiency.

2.4 PhC-based nanodevices

In this last section some of the most interesting advantages of PhC and their applications will be shown. Actual devices like lasers were successfully demonstrated recently. Additionally, due to the strong confinement, other interesting effects were observed in PhC waveguides, like slow light. This particular regime, that will be discussed below, allows a strong light-matter interaction, thus increasing the probability of non-linear effects [33].

2.4.1 Slow light

The light speed *c* is very advantageous in photonics, being the main motivation for the research in optoelectronics. The data transmission between two points can be done with photons at their extremely high speed, and this is true whatever is the distance, either on a global scale, or in the same photonic chip. Despite these undoubted advantages, however, due to the ultra-high value, it is very difficult to control light in the time domain. This is a problematic issue if we think at key devices like optical buffers, acting in the all-optical photonic chips of the next generation information networks. This problem occurs also in multiplexing, retiming and in performing convolution integrals. Engineered photonic crystals allow to overcome this difficulty, because they can actually control the speed of light [33-36] and enhance the effect of some weak interactions.

Slow light stands for light with a low group velocity, i.e. a low speed at which an optical pulse envelope propagates. The group velocity is given by:

$$v_g = \frac{d\omega}{dk} \tag{2.14}$$

where $\omega(k)$ is the dispersion relation, linking the frequency ω to the wavevector k. The group index n_g is defined as c/v_g, while on the other hand the phase velocity v_ϕ is the ratio c/n.

The nature of the delay in photonic crystals can be easily described with the picture reported in fig. 2.14. With respect to a normal waveguide, the main advantage of PhC is that light is coherently backscattered at each single unit of the crystal (fig. 2.14 left). The PhC acts like a unidimensional grating. If the forward and the backward waves agree in phase (and they do at the edge of the Brillouin zone, where $k = \pi/a$) a standing wave is formed, which is a wave with a zero group velocity.

If we slightly move away from the edge, we enter in the slow light regime, because the forward and the backward waves are “almost” in phase and the interaction is a slowly moving interference pattern. The field goes $2a$ back and moves $3a$ forward, for instance. This is a slowed down pattern. This is slow light. This phenomenon does not occur anymore when we move further away from $k = \pi/a$, because the two waves cannot interact and the waveguide behaves normally.

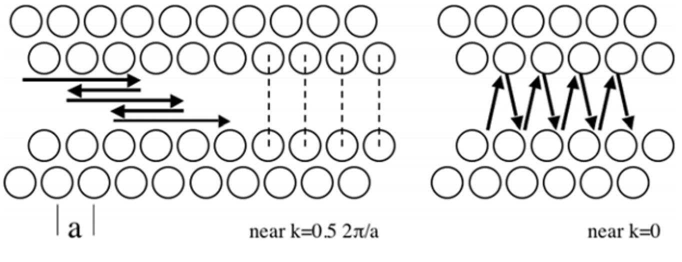

Figure 2.14: Two mechanisms for obtaining slow light in a PhC waveguide: coherent backscattering (left) and omnidirectional reflection (right) [34].

Another possible mechanism is due to the omnidirectional reflection that occurs in a PhC. This means that whatever is the propagation angle (even close to the Γ point, $k \approx 0$) light is reflected. This particular case is depicted in the right panel of fig. 2.14 and shows that these modes have a very small forward component in *k*, thus travelling in a slow light regime.

The slowdown factor S can be defined as the ratio of the phase velocity over the group velocity $S = v_{\phi}/v_g$. A group index $n_g = 100$ corresponds to a slowdown factor of about 50, if the refractive index of the material is 2 (these are typical numbers). Recently this performance was achieved for SOI slabs [37].

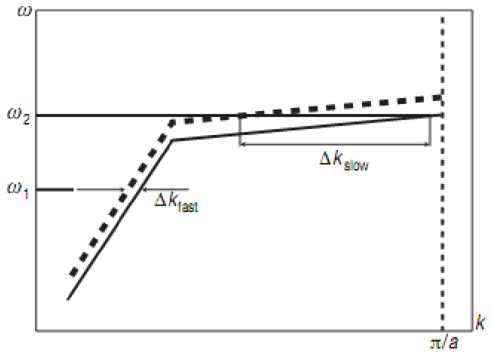

Figure 2.15: Dispersion relation $\omega(k)$ showing the fast light regime and the slow light one [35].

One of the most interesting effects of slow light regards the optical switching of a light signal. Optical switching exploits a phase change, typically expressed by $\Delta\phi = \Delta kL$: in the Mach-Zender interferometer, for instance, for $\Delta kL = \pi$ there is a complete switch on/off [33]. A change of the refractive index is able to modify the dispersion relation, as depicted in fig. 2.15. When the refractive index is tuned, the dispersion relation is shifted upwards (dashed line). In the fast light regime (steep gradient), at the frequency ω_1, the change in Δk is small. On the other side, in the slow light regime (shallow gradient), at the frequency ω_2, the change in Δk is large, thus enhancing the optical switching operation.

A demonstration of this important effect is reported in ref. [38], in which a 5 μm-long optical switch was realized with a change in refractive index $\Delta n = 4\times10^{-3}$. The typical length of a conventional waveguide would be 40 times larger [39].

Another promising application of slow light regards non linear optics. In fact, when an optical pulse travels in a slow light waveguide, it is squeezed in a smaller space, thus increasing its energy density. Therefore in this way, the light-matter interaction can be very high. A very interesting result recently obtained is the third harmonic generation in SOI PhC slab waveguides [40]. This is a non linear effect that means the generation of a light (with intensity $I_{3\omega}$ and frequency 3ω) starting from a fundamental beam (I_ω and ω). It depends on the third-order non linear susceptibility $\chi^{(3)}$ and on the cubic power of I_ω, being actually a transformation of three ω photons into a single 3ω photon (see fig. 2.16(a)).

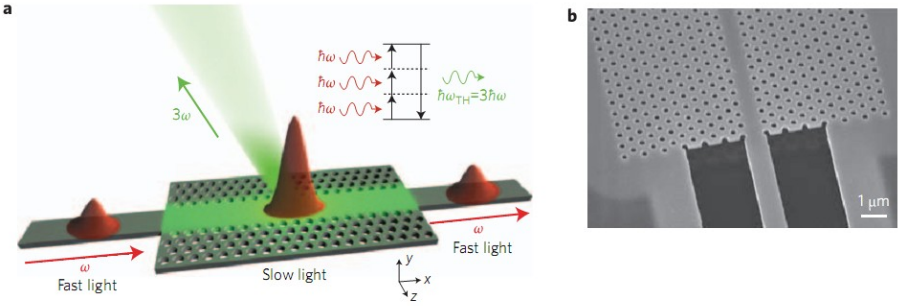

Figure 2.16: (a) Schematic of the slow light PhC waveguide with the third harmonic generation. (b) SEM image of the waveguide feeding the PhC waveguide etched in a thin Si membrane [40].

I_ω is proportional to the pump power and to the group index and it is inversely proportional to the effective area of the fundamental mode. Therefore by using both the light confinement provided by the PhC and the enhanced energy density due to the slow light effect, it is possible to generate third harmonic light. The pump power required for observing light emission at 520 nm in Silicon can be thus reduced to just 10 W [40]. Additionally the PhC around the line defect can be engineered in order to act as a grating, thus helping in the extraction of this light, that on the contrary would be strongly absorbed by the material.

2.4.2 2D PhC-based nanolasers

The most important technological achievements with the use of PhC regard the realization of efficient nanolaser sources. It was already discussed how efficient are PhC nanocavities, since they can provide a ultra-high Q factor in volumes comparable to a cubic-wavelength. In these cavities therefore a strong Purcell effect is expected, and this can reduce the lasing threshold and also increase the modulation rate.

In fact one of the most interesting results that can be found in literature is the demonstration of an optically pumped photonic crystal laser with a threshold as low as few nanowatts [41]. This result was recently published and regards the lasing from just 2-4 InGa quantum dots in a GaAs photonic crystal slab in which an L_3 cavity was realized. Moreover, by indicating with β the fraction of spontaneously emitted photons that is coupled into a single cavity mode, a β of about 0.85 was found in this system. In a conventional semiconductor laser, on the contrary, this value is very small, due to the small Purcell factor [41].

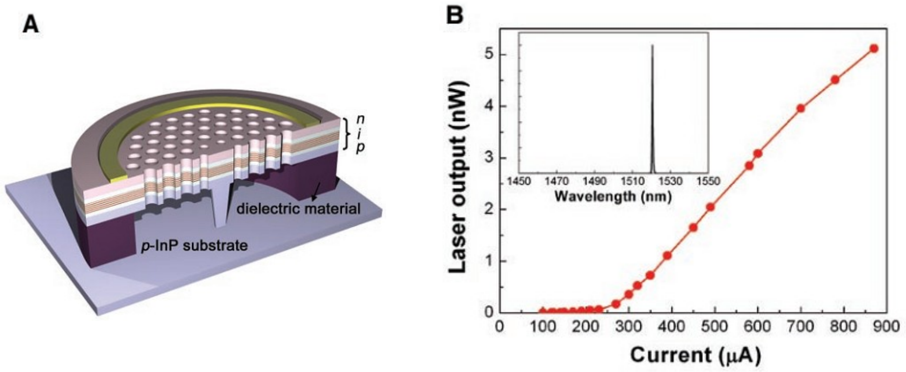

Figure 2.17: (a) Schematic of the electrically driven InP PhC laser. (b) Laser output as a function of the injected current. The threshold is around 260 μA; in the inset a spectrum recorded at 700 μA is reported. Adapted from [26].

Another very important achievement is a modulation rate of the order of 100 GHz [27]. This paper refers to an extremely fast photonic crystal laser, with response time of a few picoseconds. This result indicates that this laser is very promising for applications in high-speed communication technology, though lasing was obtained at cryogenic temperatures and with a material which is not compatible with the Silicon technology.

The natural upgrade of an optically pumped photonic crystal laser is the electrically-driven lasing action. Actually two main different kind of geometries were implemented: the first one is the a vertically injected laser, in which electrical injection is vertical, the second one is a laterally injected laser. In the former structure (see fig. 2.17) a Purcell factor of about 400 is estimated, while a relatively high threshold was measured, around 260 μA. This device is the first electrically-pumped photonic crystal laser and is considered a milestone for all the electrically-driven light sources for optoelectronics. In fact, it is very hard to efficiently pump carriers inside the active region and that solution is really interesting. However, the pillar through which the current is injected reduces the Q factor of the cavity, thus being an actual limitation on the performances of the whole device. Additionally the architecture of the device is really complicated, requiring many careful fabrication steps.

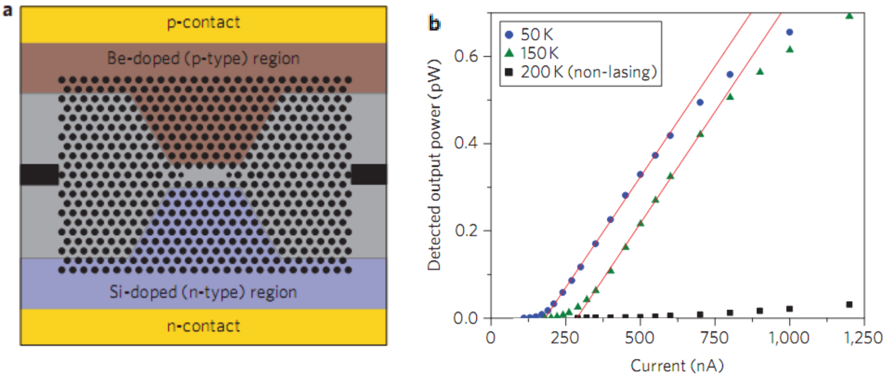

Figure 2.18: (a) Schematic of the lateral injection in the electrically pumped GaAs PhC laser. The doped regions are highlighted in red (p-type) and in blue (n-type). A trench is etched down at the sides of the PhC to avoid current leakage. (b) Measured light output as a function of the injected current at 50 K, 150 K and 200K. Adapted from [28].

A much simpler design was recently suggested [28, 42], in which the lateral carrier injection in a PhC cavity is exploited. This idea allows to define lithographically the electron flow in the cavity and it is compatible with any PhC design. A *p-i-n* structure is easily fabricated by lithography steps and ion implantation.

An efficient electroluminescent device was demonstrated in ref. [42], in which the electrically pumped InAs quantum dots, embedded in a GaAs PhC slab, emit light strongly coupled to the cavity. Afterwards a laser was demonstrated by the same research group [28] by exploiting a similar design. This is reported in fig. 2.18 (a), where the GaAs PhC is shown. The contact pads are realized by ion implanting Be for p-type doping and Si for n-type doping. The two doped pads are very close to the cavity, thus forming the depletion zone of the junction right in the center of the cavity. This is the place where most of the radiative electron-hole recombinations occur and this is a key point of this device. The gain material is a multilayer of InAs quantum dots.

The lasing action at 1175 nm was observed at low temperatures (50 K) with an extremely low threshold, at about 180 nA, as shown in fig. 2.18 (b). This represents the lowest value ever measured in an electrically pumped semiconductor laser, three orders of magnitude less than the vertical laser showed before. Additionally the applied voltage at the threshold is about 1 V, thus implying that this system is really efficient, consuming a few hundreds of nW to be turned on. Note that when the temperature is raised, the quantum dot resonance and the cavity resonance show a redshift with different rates and therefore at 200 K there is no more a lasing action.

We can conclude that this is a very efficient laser, very promising for optical in-chip interconnections. However, it has two important limitations: it is done with a III-V semiconductor and it only works at low temperatures.

In the next chapter it will be shown an electrically-pumped nanolight source realized in Silicon, working at room temperature at 1.5 μm, with a power density comparable with the nanolaser just described.

References

[1] E. Yablonovitch, Phys. Rev. Lett. **58**, 2059 (1987).

[2] J. D. Joannopoulos, S. G. Johnson, J. N. Winn and R. D. Meade, *Photonic Crystals: Molding the flow of light*, Princeton University Press, Princeton, 2008.

[3] J. D. Jackson, *Classical Electrodynamics*, John Wiley & Sons, New York, 1962.

[4] K. M. Ho, C. T. Chan and C. M. Soukoulis, Phys. Rev. Lett. **65**, 3152 (1990).

[5] E. Yablonovitch, T. J. Gmitter and K. M. Leung, Phys. Rev. Lett. **67**, 2295 (1991).

[6] E. Yablonovitch, T. J. Gmitter, R. D. Meade, A. M. Rappe, K. D. Brommer and J. D. Joannopoulos, Phys. Rev. Lett. **67**, 3380 (1991).

[7] J. C. Fleming and S. Y. Lin, Opt. Lett. **24**, 49 (1999).

[8] A. Tandaechanurat, S. Ishida, D. Guimard, M. Nomura, S. Iwamoto and Y. Arakawa, Nature Phot. **5**, 91 (2011).

[9] T. F. Krauss, R. M. De La Rue and S. Brand, Nature **383**, 699 (1996).

[10] J. D. Joannopoulos, P. R. Villeneuve and S. Fan, Nature **386**, 143 (1997).

[11] M. Fujita, S. Takahashi, Y. Tanaka, T. Asano and S. Noda, Science **308**, 1296 (2005).

[12] S. Noda, M. Fujita and T. Asano, Nature Phot. **1**, 449 (2007).

[13] K. Kounoike, M. Yamaguchi, M. Fujita, T. Asano, J. Nakanishi and S. Noda, Electron. Lett. **41**, 1402 (2005).

[14] G. Khitrova, H. M. Gibbs, F. Jahnke, M. Kira and S. W. Koch, Rev. Mod. Phys. **71**, 1591 (1999).

[15] S. M. Spillane, T. J. Kippenberg and K. J. Vahala, Nature **415**, 621 (2002).

[16] P. Michler, A. Kiraz, C. Becher, W. V. Schoenfeld, P. M. Petroff, L. Zhang, E. Hu and A. Imamoglu, Science **290**, 2282 (2000).

[17] D. K. Armani, T. J. Kippenberg, S. M. Spillane and K. J. Vahala, Nature **421**, 925 (2003).

[18] K. Srinivasan, P. E. Barclay, O. Painter, J. Chen, A. Y. Cho and C. Gmachl, Appl. Phys. Lett. **83**, 1915 (2003).

[19] E. M. Purcell, Phys. Rev. **69**, 681 (1946).

[20] R. Loudon, *The Quantum Theory of Light*, Oxford University Press, New York, 1983.

[21] E. Kuramochi, H. Taniyama, T. Tanabe, A. Shinya and M. Notomi, Appl. Phys. Lett. **93**, 111112 (2008).

[22] T. Asano, B. S. Song and S. Noda, Opt. Expr. **14**, 1996 (2006).

[23] E. Kuramochi, N. Notomi, S. Mitsugi, A. Shinya, T. Tanabe and T. Watanabe, Appl. Phys. Lett. **88**, 041112 (2006).

[24] B. Song, S. Noda, T. Asano and Y. Akahane, Nature Mater. **4**, 207 (2005).

[25] Y. Akahane, T. Asano, B. Song and S. Noda, Nature **425**, 944 (2003).

[26] H.-G. Park, S.-H. Kim, S.-H. Kwon, Y.-G. Ju, J.-K. Yang, J.-H. Baek, S.-B. Kim and Y.-H. Lee, Science **305**, 1444 (2004).

[27] H. Altug, D. Englund and J. Vuckovic, Nature Phys. **2**, 484 (2006).

[28] B. Ellis, M. A. Mayer, G. Shambat, T. Sarmiento, J. Harris, E. E. Haller and J. Vuckovic, Nature Phot. **5**, 297 (2011).

[29] C. D. Presti, A. Irrera, G. Franzò, I. Crupi, F. Priolo, F. Iacona, G. Di Stefano, A. Piana, D. Sanfilippo and P. G. Fallica, Appl. Phys. Lett. **88**, 033501 (2006).

[30] S. L. Portalupi, M. Galli, C. Reardon, T. F. Krauss, L. O' Faolain, L. C. Andreani and D. Gerace, Opt. Expr. **18**, 16064 (2010).

[31] N.-V.-Q. Tran, S. Combrié and A. De Rossi, Phys. Rev. B **79**, 041101 (2009).

[32] M. Galli, S. L. Portalupi, M. Belotti, L.C. Andreani, L. O'Faolain and T. F. Krauss, Appl. Phys. Lett. **94**, 071101 (2009).

[33] Y. A. Vlasov, M. O'Boyle, H. F. Hamann and S. J. McNab, Nature **438**, 65 (2005).

[34] T. F. Krauss, J. Phys. D: Appl. Phys. **40**, 2666 (2007).

[35] T. F. Krauss, Nature Phot. **2**, 448 (2008).

[36] T. Baba, Nature Phot. **2**, 465 (2008).

[37] A. Y. Petrov and M. Eich, Appl. Phys. Lett. **85**, 4866 (2004).

[38] D. M. Beggs, T. P. White, L. O'Faolain and T. F. Krauss, Opt. Lett. **33**, 147 (2008).

[39] W. M. J. Green, M. J. Rooks, L. Sekaric and Y. A. Vlasov, Opt. Expr. **15**, 17106 (2006).

[40] B. Corcoran, C. Monat, C. Grillet, D. J. Moss, B. J. Eggleton, T. P. White, L. O'Faolain and T. F. Krauss, Nature Phot. **3**, 206 (2009).
[41] S. Strauf, K. Hennessy, M. T. Rakher, Y.-S. Choi, A. Badolato, L. C. Andreani, E. L. Hu, P. M. Petroff and D. Bouwmeester, Phys. Rev. Lett. **96**, 127404 (2006).
[42] B. Ellis, T. Sarmiento, M. Mayer, B. Zhang, J. Harris, E. Haller and J. Vuckovic, Appl. Phys. Lett. **96**, 181103 (2010).

3. Light emission from Si in PhC nanostructures

Silicon is a bad emitter. This semiconductor is in fact characterized by an indirect band gap. Then a radiative recombination of an electron-hole pair has a negligible probability of occurrence, competing with very efficient non-radiative processes, like SHR and Auger recombinations. In order to induce the luminescence from Silicon, therefore, it is necessary to overcome its intrinsic limitations. Different strategies were proposed in the past, and many results were achieved, indicating that it is possible to get some light out of Silicon.

Among these strategies, a very interesting one regards the possibility to introduce some defects in the Si crystal. These defects can be either luminescent ions, like Er, or luminescent centers like Carbon- or Hydrogen-related bonds. Some of these centers are already inserted in SOI wafers, due to their fabrication procedure known with the name of Smart-cut. Since these defects produce photoluminescence, it is possible to improve their performances, by making a treatment in a H_2*-rich plasma in a reactive ion etching system, for instance. In this way we actually obtained an efficient light source with a broad band emission in the near infrared.*

If this plasma treatment is applied to a nanostructured sample, in which a photonic crystal pattern is etched down, further advantages can be exploited. And in fact, due to Purcell effect, a very intense photoluminescence is recorded from PhC L_3 *nanocavities.*

A question arises, then: what about the possibility to electrically excite these defects? Before answering this question, however, a detailed study on the electrical conduction across PhC is required. Some results about this issue are present in literature for III-V semiconductor, and therefore we studied in detail the electrical conduction across PhC made on Silicon.

By knowing the mechanism of carrier injection in a PhC, some electrically-driven devices can be fabricated. Consequently the electrical excitation of those H_2*-related defects is actually feasible. We present here the fabrication and the optical characterization of a prototype electroluminescent device. This device works very well at room temperature, showing a very high EL intensity and the narrowest linewidth ever measured in Silicon. The performances of this device are comparable with the III-V PhC-based nanolasers.*

3.1 Silicon. A bad emitter.

Silicon is by far the principal material used in microelectronics. Despite the undoubted progress achieved in the miniaturization of Si-based electronic devices for realizing smaller, cheaper and smarter applications in the human life, Silicon is still a bad light emitter. The reason lies in its band diagram: Silicon in fact is an indirect 1.1 eV band gap semiconductor [1]. This means that the highest level in the valence band (the so-called Γ point) and the lowest level in the conduction band (X point) correspond to different **k** vectors, as shown in fig. 3.1. As a consequence an electron-hole (e-h) radiative recombination requires some additional momentum. This can be given for instance by a phonon.

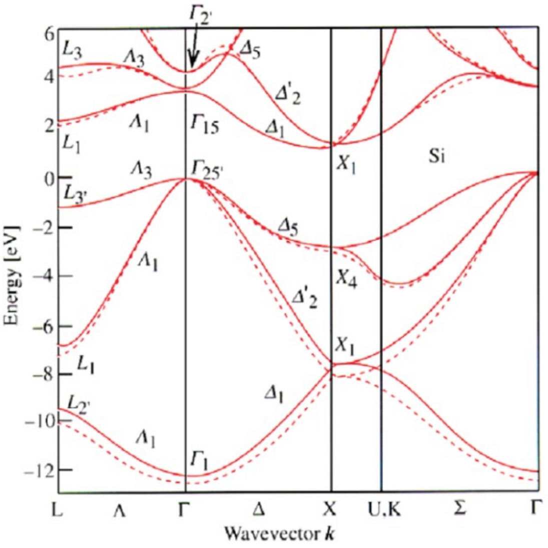

Figure 3.1: Band structure for Silicon, as calculated by using non-local (continuous line) and local (dotted line) pseudo-potential methods. The indirect band gap is clearly visible [1].

Therefore the radiative recombination is a three-particles process, involving the e-h pair, a photon and a phonon (either absorbed or emitted): though it is not forbidden, it is very improbable. In fact, this process is characterized by a lifetime of more than 10 ms at above 20 K [2, 3], which is much longer than the typical lifetime of a III-V semiconductor with direct band gap (100 ns).

The experimental measurements of the carrier lifetime in Si are usually of the order of μs-ms, depending on the impurities or defects concentrations. Thus in Silicon radiative processes have negligible probability of occurrence with respect to the non-radiative ones, since Shockley-Hall-Read [4, 5] and Auger recombinations [6] certainly dominate.

Therefore the quantum efficiency, i.e. the probability of light emission in a recombination process, of c-Si is very low ($10^{-6} – 10^{-7}$), several orders of magnitude less than in III-V semiconductors, which means that bulk Silicon is in itself a bad emitter.

3.1.1 How to get light out of Silicon

In order to overcome the difficulties of getting some light out of Silicon, different approaches were followed, which led to the realization of efficient Si-based light emitting diodes (LED), to the achievement of optical gain in nanostructured Si, to Raman-stimulated lasers, or even to III-V lasers efficiently grown on Silicon.

A first attempt to obtain an efficient LED involved the reduction of the non-radiative processes, by using high quality intrinsic Silicon substrates. Other improvements can be obtained by doing a good passivation of the surfaces or by increasing the light extraction, with a texturized wafer surface, or by reducing the size of the highly doped regions of the device (to reduce the free carriers absorption). By exploiting all these tricks, the most efficient LED realized with Silicon was demonstrated by M. A. Green and coworkers [7, 8]. The device, whose scheme is shown in fig. 3.2 (a), was characterized by an external quantum efficiency as high as 1% at 200 K.

Another very interesting approach for achieving efficient light emission from Silicon is through the deliberate introduction of extended defects, like dislocation loops. By performing a Boron implantation, some dislocation loops are produced in the Si wafer. These loops introduce a local strain field, which locally modifies the band gap, leading to a sort of spatial confinement of the carriers. This confinement strongly reduces the non-radiative recombination, because the carriers diffusion to point defects is prevented and Ng and coworkers observed (see the device in fig. 3.2 (b)) a strong band-edge electroluminescence at room temperature, with an external quantum efficiency of about 2×10^{-4} [9].

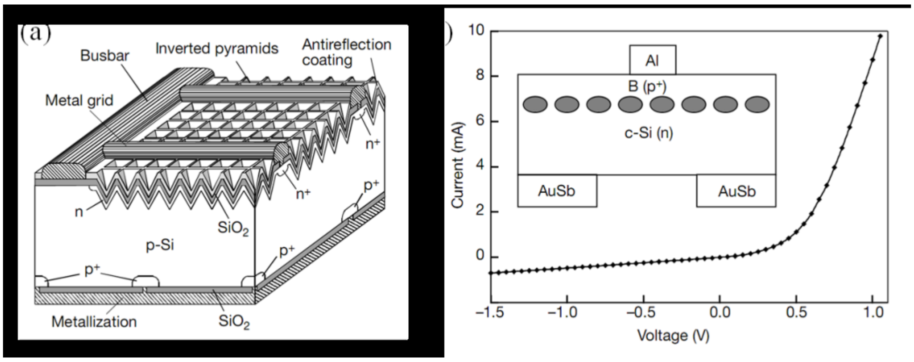

Figure 3.2: (a) Schematic of the LED with texturized surface and narrow highly doped regions [7]. (b) I-V curve at room temperature of the LED with dislocation loops. In the inset the scheme of the device is shown: light is emitted from the bottom region between the AuSb contacts [9].

More recently, the first Silicon laser based on the Raman scattering has been demonstrated. In a crystal a spontaneous Raman scattering process is caused by the interaction between an incoming photon and the thermal lattice oscillations. In the spontaneous Raman scattering, the thermal vibration typical of the Si lattice at a frequency ω_v = 15.6 THz produces a sinusoidal modulation of the susceptibility of the material. If the pump field oscillates at a frequency ω, then the interaction with the material produces induced polarizations at two different frequencies, namely the Stokes one, $\omega_s = \omega - \omega_v$, in which a phonon is generated for the conservation of energy, and the anti-Stokes one, $\omega_a = \omega + \omega_v$, in which a pre-existing phonon is absorbed [10].

When both the pump field and the Stokes waves are present, extra phonons can be generated coherently, thus having a stimulated Raman scattering phenomenon. This is the mechanism responsible of the optical amplification. The interaction of the pump field with the Stokes waves produces a driving force for atomic vibrations; this force enhances a power transfer from the pump field to the Stokes wave in a very efficient way in

Silicon. In an amplifier, an incident beam is amplified at the expenses of the pump beam. In a laser, the spontaneously generated Stokes phonons are resonantly amplified inside a cavity and produce an intense and coherent beam of light at the Stokes wavelength, as soon as the gain equals or exceeds the round-trip losses.

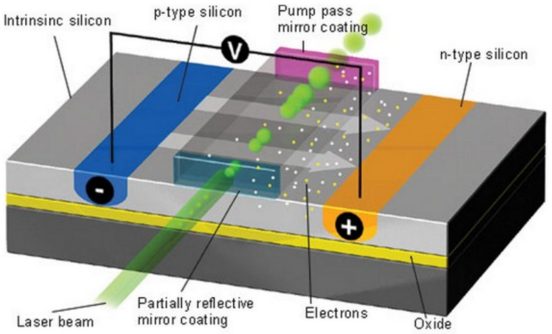

Figure 3.3: Schematic of the continuous-wave Raman-based Silicon laser. The p-i-n diode is placed on the two sides of the light beam, with the purpose of sweeping the free electrons from the central waveguide, thus reducing consistently FCA [15].

The Raman gain, however, is strongly limited by the free-carrier absorption (FCA): at high pumping fluxes, this is a dominant process. Despite this limitation, optical gain was demonstrated in Si waveguides, a few centimeters long, by using short excitation light pulses [11-13], since FCA is a very slow process, with respect to the Raman scattering. By using this method, the first Raman laser in Si was demonstrated in 2005 [14] under pulsed optical excitation.

By combining this method with a p-i-n junction, which in reverse bias can deplete quickly electrons inside a channel waveguide, the same authors demonstrated also the first continuous-wave Raman-based all Silicon laser [15]. A sketch of this particular device is depicted in fig. 3.3.

Another interesting approach to obtain optical gain in Si regards the quantum confinement effect, by using, for instance, Silicon nanocrystals (Si-nc). In such nanostructures, electrons and holes are spatially confined and the momentum conservation law can be in some way relaxed. In this way, the radiative recombination probability of free carriers is increased, leading to a raise of the optical efficiency of the material. Si-nc can be embedded in a silica host and many techniques allow to do that. The most popular way consists in the deposition of a substoichiometric silica film (SiO_x, $x < 2$) with a subsequent thermal annealing at high temperature (< 900 °C), in order to induce the phase separation between the Si in excess and the SiO_2, which are thermodynamically stable [16].

Si-nc are characterized by a broad band luminescence at 700-900 nm, with a wavelength peak that depends on the size of the nanostructures, owing to the quantum confinement effect [17]. Efficient LED were realized with Si-nc embedded in silica in a MOS structure, demonstrating that Si-nc can actually be electrically excited [18, 19]. Internal quantum efficiencies as high as 0.6 % were demonstrated at room temperature [20] and enhanced light extraction was obtained by coupling the emission with a PhC structure [21]. Moreover optical gain was demonstrated with this material by measuring the amplified spontaneous emission using the variable strip length method [22]. Despite all the advantages, Si-nc suffer the competing mechanism of Auger recombination and have the disadvantage of the emission wavelength in the visible region. At these wavelengths Si absorbs too much for having in the end feasible applications.

3.1.2 Luminescence centers in Silicon

A completely different kind of strategies attempted for getting light out from Silicon regards the deliberate introduction of luminescence centers in the Si lattice. As it is known, a defect in the lattice means an allowed localized state in the prohibited band gap. An e-h recombination, therefore, can occur via this defect. This fascinating strategy was followed with the introduction of Er ions, for instance, in Silicon. Erbium is a rare earth ion that emits photons in the near infrared (it is characterized by an emission wavelength at about 1.5 μm, as it will be discussed more extensively in the next chapter). It can be introduced in Silicon via ion implantation [23-25] or molecular beam epitaxy [26, 27]. It was demonstrated that when Er is inserted in a Si wafer, it is excited not by a typical atomic absorption, but by excitation via optically generated e-h pairs that transfer their recombination energy to the Er ions [28]. Electrons are, in fact, trapped at a deep level, introduced by the Er impurity in the Si band gap. Recombination of the formed bound e-h pair then excite the Er ion that can decay emitting photons.

This process is very efficient only at low temperatures, however, because at temperatures higher than 100 K strong non-radiative channels are present, namely energy back-transfer and Auger effect. The first one is particularly effective by raising the temperature: it is exactly the reverse process of the excitation mechanism and it can happen easily when the phonons population is high enough, i.e. by increasing temperature [28].

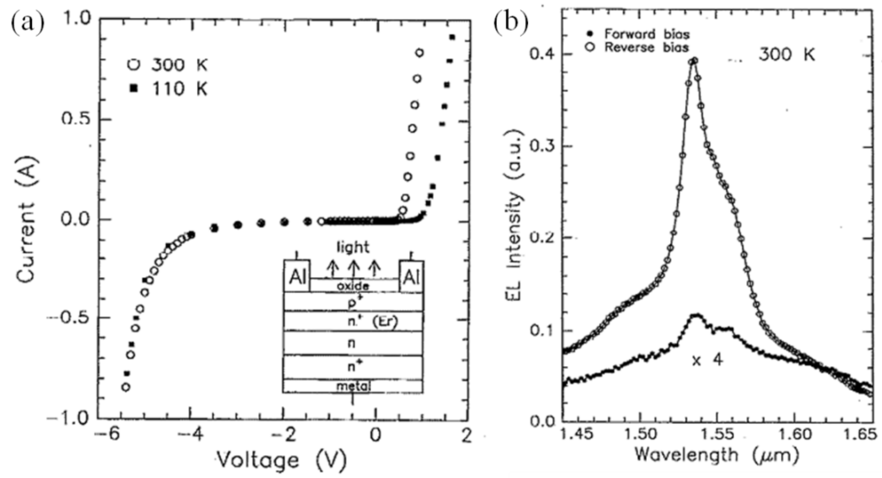

Figure 3.4: (a) I-V characteristic of the device based on Er-O co-implantation in Silicon registered at 110 K and 300 K. The schematic of the device is reported as an inset. (b) EL intensity obtained from this device in forward and reverse bias. The reverse bias EL intensity is much higher. In this case Er is excited via impact ionization from hot carriers. Adapted from ref [30].

By co-implanting Oxygen (together with Erbium), the formation of Er-O complexes is favoured. These complexes are the actual responsible of the emission from Si and therefore the PL intensity is ten times higher at room temperature [29]. This is the reason why room temperature electroluminescence was observed from this system at 1.54 μm in both forward and reverse biased p-n diodes (a schematic and the I-V characteristic are shown in fig. 3.4 (a)). The Er excitation was found to be more efficient in reverse bias (see fig. 3.4 (b)), when Er is excited by impact ionization processes [30]. Despite this promising result, the efficiency of such a system is not so useful for practical applications, due to the competing non-radiative decay paths.

Other defects were demonstrated to induce photoluminescence from Si. Carbon, for instance, makes complexes with many different impurities in Silicon, resulting in a very large variety of emitting centers. Photoluminescence was unambiguously detected from C complexed with another C atom (the so-called G-line, emitting at 969 meV), one O atom (the C-line, emitting at 789 meV), one N atom (745.6 meV band) and so on [31]. In particular, among these centers, the G-line has been used to obtain optical gain in a periodically patterned structure, realized into the top Si layer of a SOI wafer [32].

Another possibility to achieve light emission from Silicon is to do a reactive ion etching (RIE) treatment in Hydrogen-based plasma. Also in this case some levels are introduced in the Silicon band gap and these defects have luminescence properties [33-35]. These levels were investigated by performing Deep Level Transient Spectroscopy (DTLS), but the strategy of inserting them in Silicon has not been well developed, despite the promising results. In fact this is a very easy technique to introduce luminescence centers in Silicon. In the following part of the chapter, we investigate if this is a feasible for practical applications, using for instance Photonic Crystals.

3.2 H_2-related defects obtained by plasma treatment

Among the many advantages of using Photonic Crystals, one of the most important is the Purcell effect [36], through which a nanocavity is able to enhance the radiative emission of a certain emitter. Recently it has been demonstrated that Purcell effect can enhance significantly even the luminescence coming from the defects incorporated in Silicon during the industrial fabrication process of Silicon on Insulator (SOI) wafers [37]. This procedure is called Smart-cut® and is depicted in fig. 3.5 [38]. A key moment of the Smart-cut process is the ion implantation of light ions, like

Hydrogen: the final SOI wafer obtained in this way can thus have some Hydrogen-related defects, lying close to the surface.

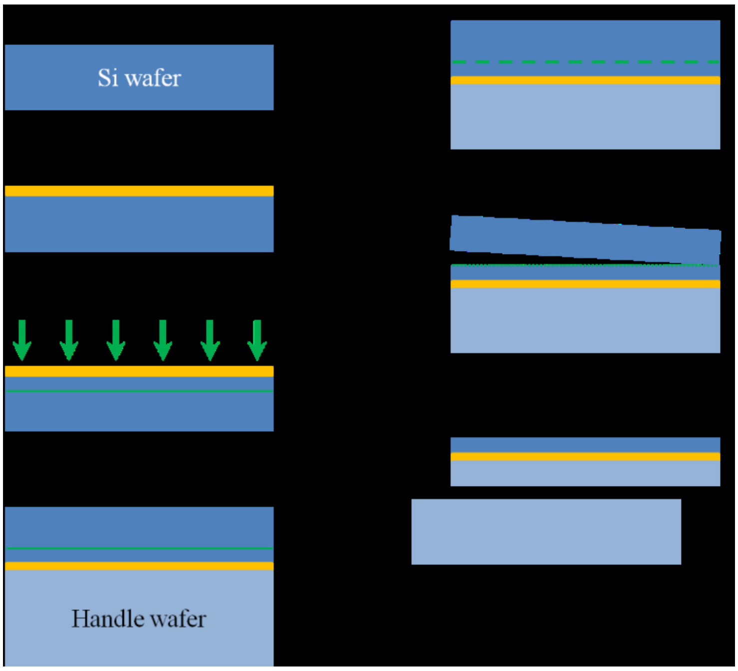

Figure 3.5: Schematic of the complete Smart-cut process. A Si wafer is thermally oxidized; it is implanted with H_2, flipped and bonded to another Si handle wafer; a certain annealing process induce the formation of bubbles at the projected range of the implantation and then the wafer is broken exactly here. The remaining part is polished (chemical-mechanical planarization) and cut.

In fact by looking at the photoluminescence spectrum of an unpatterned Silicon membrane, obtained from an as-bought SOI wafer, it turns out that there is a weak and broad PL signal at sub-band gap wavelengths (with respect to Silicon) between 1300 nm and 1600 nm. This signal is much higher than that observed for instance in a Czochralski-Si (Cz-Si) wafer. These measurements are both reported in fig. 3.6. The authors of this work believe that this emission is due to some defects originating in the Smart-cut process [37].

By patterning this SOI wafer, realizing a PhC, there is an overall increase of the PL intensity, due to the fact that the PhC enhances itself the light extraction. The observed enhancement is shown also in fig. 3.6, and it depends on the wavelength, since it is a function of the electromagnetic density of states available in the photonic stop band. If the pattern is a L_3 far-field optimized PhC cavity there is a further enhancement (about a factor of 300), due to a combination of extraction efficiency and Purcell effect. It is also worth noticing that the PL intensity was registered in all cases at room temperature.

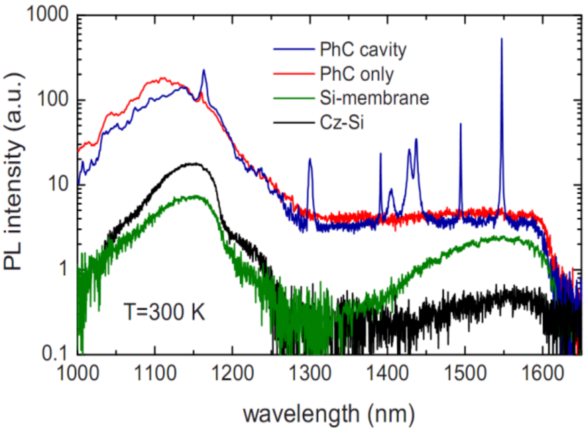

Figure 3.6: Broadband room temperature PL spectra of a far-field optimized L_3 nanocavity, a reference membrane, an unpatterned Si membrane and a reference Cz-Si sample. The sharp drop at 1620 nm is due to the detector cut-off [37].

According to this study and looking also at the Smart-cut process, we want now to introduce some additional active defects, by using for instance a further H_2^+ implantation and H_2 and Ar/H_2 plasma treatments with a Reactive Ion Etching (RIE) system.

Also in this case we used L_3 PhC nanocavities, characterized by a period of 420 nm and r/a = 0.28, being these numbers useful for working around the telecommunication wavelength of 1.5 μm. For these cavities we performed both the gentle confinement effect (for increasing the Q factor) and the far-field optimization (for enhancing the out-of-plane coupling).

We realized the PhC pattern using electron-beam lithography on a 400 nm layer of ZEP-520A (Zeon Chemicals). This pattern was transferred to the silicon layer by reactive ion etching with a SF_6:CHF_3 = 1:1 gas mixture, etching through the entire Silicon layer: the used power is 21 W and the etching time is 1’50’’ [39]. Finally an HF-based solution was used to do an undercut, leaving an air-bridge Silicon PhC slab. The silicon slab is 220 nm thick, and the PhC membrane is sustained at its sides by a 2 μm thick buried oxide. These SOI wafers were purchased from SOITEC, which produces them with the Smart-cut procedure.

A SEM picture of a L_3 cavity is shown in the inset of fig. 3.7. After the fabrication we applied to the cavity a plasma treatment, in a RIE system at 40 W for 30’. The plasma ions are obtained by using pure H_2 and a Ar/H_2 mixture: these gases chemically and physically react with the Si slab and are able to create Hydrogen-related defects, which are known to emit photons [33-35].

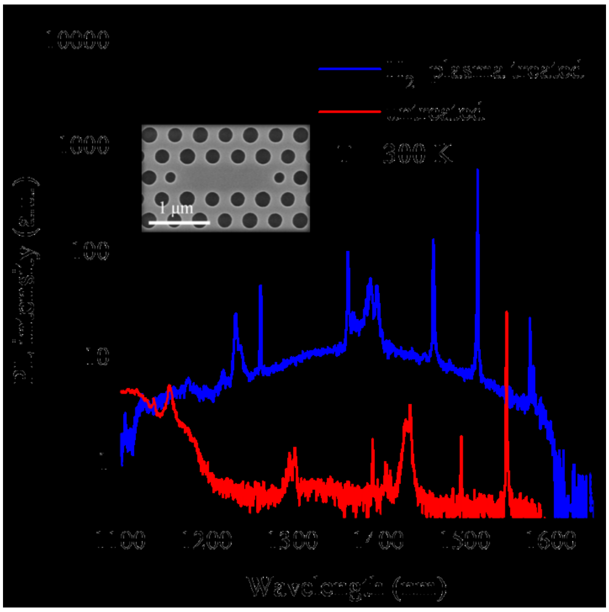

Figure 3.7: μPL measurements at room temperature from a L_3 nanocavity without plasma treatment (red) and after pure Hydrogen plasma treatment at 40 W for 30’ (blue). A SEM picture of the cavity is reported as inset.

In order to investigate the PL emission, we used room temperature confocal μPL measurements and resonant scattering technique for estimating the Q factor. The cavities were excited with a Nd-YAG laser, emitting at 532 nm. Thanks to a microscope objective (NA = 0.8), the laser spot was focused down to an area 1 μm^2 small, thus exciting exactly the center of the cavity. The emitted light was collected back with the same objective and passed to a grating spectrometer. More details on this experimental set up are given elsewhere [40]. The resonant scattering technique consists in measuring the reflectance at normal incidence from the PhC cavity in a crossed-polarization geometry, defined with a polarizer and an analyzer. The cavity must be oriented at 45° with respect to both the polarizer and the analyzer: this allows to achieve a simultaneous coupling of the incoming and outgoing polarizations with the fundamental cavity mode, maximizing the resonant signal over the background.

In fig. 3.7 we reported the comparison of the PL emission from a treated and untreated cavity. The untreated one shows a very weak and broad luminescence and some sharp peaks, corresponding to the cavity modes. The H_2 plasma-treated cavity, on the other hand, is characterized by the same broadband luminescence, but 1-2 orders of magnitude higher. A similar PL signal was observed in Cz-Si at 2 K after a plasma treatment in Deuterium rich environment [35]. If we consider also the Purcell effect, we observed then a 3000 enhancement of the PL intensity at room temperature at telecom wavelengths in Silicon.

This remarkable result led to a detailed investigation of the effects of plasma conditions on the enhancement. We analyzed the PL intensity as a function of the power applied for turning on the plasma, the treatment duration and the composition, investigating both a pure H_2 plasma (gas flow of 200 sccm) and a H_2/Ar one (200 sccm for each gas). A resume of the most significant data is reported in fig. 3.8.

Let us consider a fixed power (20 W) at which the plasma is sustained. By increasing the treatment time the PL intensity of the fundamental peak initially increases (see panel (a)); further processing induces a saturation and a decrease of the PL intensity both for H_2 and H_2/Ar plasmas. This may be due to an excess of physical damage of the Si surface (and of the holes constituting the PhC pattern in particular), since RIE is a severe physical process.

On the other hand, the Q factor of the cavities has a different trend (see panel (b)): it increases by increasing time for the H_2 plasma, while it almost immediately starts to decrease when Ar is thrown in the RIE chamber. The reason is that H_2 is a light molecule and it has an important role of passivation of defects for Si, having thus a good effect on the holes roughness. Ar, instead, is a heavy ion and it can damage Silicon, even at low powers. Therefore it introduces further sources of losses, thus reducing the Q factor. We can conclude that the introduction of Ar in the plasma has detrimental effects on the optical properties of the PhC cavities.

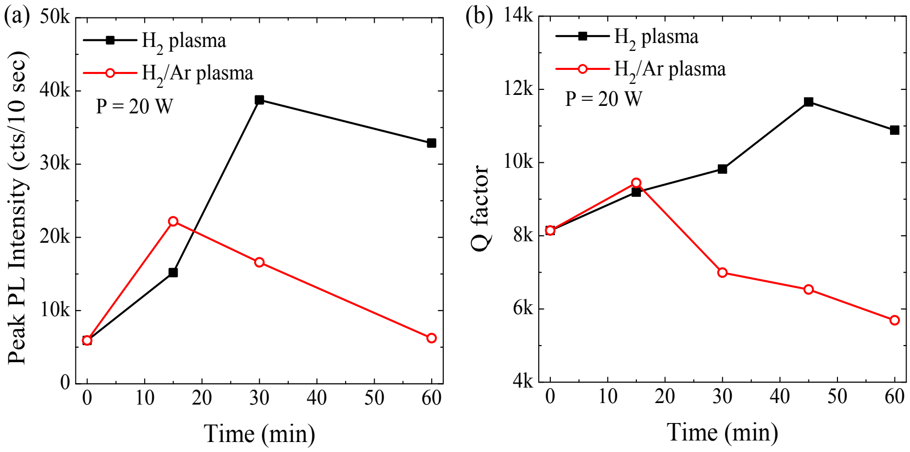

Figure 3.8: (a) PL intensity of the fundamental cavity peak as a function of time for pure H_2 plasma and a H_2/Ar plasma (fluxes ratio 1:1) at 20 W. (b) Trend of the Q factor of the L_3 cavities in the same experimental conditions.

A figure of merit describing the best compromise between Q factor and PL intensity can be calculated by multiplying and normalizing the product Q×PL. This product demonstrates that the best sample is obtained with pure H_2 plasma, with intermediate durations of the treatment (30 min). We also changed the power, but 10 W leads to instability of the plasma, while higher powers lead to a saturation (up to 40 W) and then a decrease of the PL intensity, which is probably due to the introduction of too much physical damage.

We performed the best plasma treatment (40 W, 30 min, H_2 plasma) both before and after the fabrication of the PhC. In the former case, however, the enhancement is reduced (just 3-4 times versus 1-2 orders of magnitude). This may be due to the fact that a PhC offers a much larger surface area to the plasma treatment, thus allowing the creation of a higher number of emitting centers.

By carefully looking at the PL emission in fig. 3.7, we noticed that the fundamental cavity mode suffers a blueshift of about 30-40 nm after the treatment in H_2 plasma. This can be ascribed to a decrease of the refractive index, due to the incorporation of some Hydrogen ions in the silicon [41], and to a slight modification of the holes' size. In fact the holes are modified by the plasma, being subjected to a physical process.

We analyzed the effect of different plasma treatments on the surface of the PhC and some SEM pictures are reported in fig. 3.9. In these pictures we compared the structural features of the PhC holes. Fig. 3.9 (a) reports an untreated PhC, with the holes typical roughness introduced by the RIE etching process. When the sample is treated in H_2 plasma at 20 W for 30' (see fig. 3.9 (b)), the holes have smoother boundaries and a dark shadow appears on top. This represents the penetration depth of Hydrogen in Silicon. The smoothing of the holes is consistent with the increase of Q factor reported in fig. 3.8 (b), because it is a clear evidence that the scattering losses are definitely lower, with respect to the untreated cavity. When both Ar and H_2 are present some damage can be observed, the holes shape becomes asymmetric, essentially because of Ar ions (see panel (c)). This is again consistent with the Q measurements previously shown: in fact the Q factor of the cavity is strongly reduced, because the structural quality of the cavity is degrading. Finally, when the pure H_2 plasma is turned on at high powers, 100 W (see fig. 3.9 (d)), Hydrogen penetrates down to 70 nm in the Si wafer.

When the power is too high we already said that the PL intensity decreases. We estimate that in this case the temperature of the samples during plasma treatment reaches up to 70°C, which is a temperature that is able to induce the Hydrogen out-diffusion, thus reducing the amount of optically active defects.

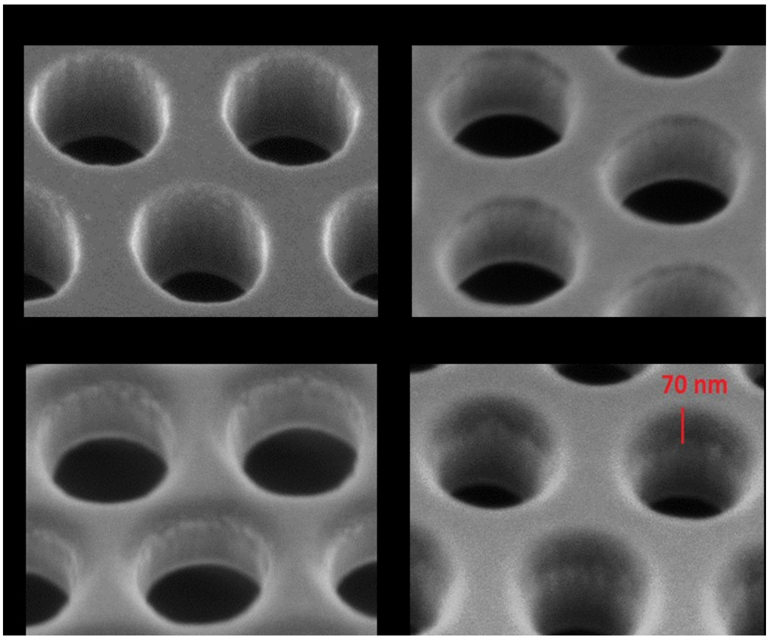

Figure 3.9: High resolution SEM pictures showing the effect of plasma treatment on the Silicon surface of the PhC holes. (a) Untreated PhC; (b) H_2 plasma treated (20 W, 30 min); (c) H_2/Ar plasma treated (20 W, 30 min); (d) H_2 plasma treated (100 W). It is worth noticing the dark shades: these indicate the penetration depth of Hydrogen in Silicon. The damage increases when either Ar is introduced or power is increased. In the last case the penetration depth is about 70 nm.

We can conclude that there is a clear trade-off between the defect quantity and the PhC quality. The pure H_2 plasma is greatly superior to the Ar/H_2 one. The former, in fact, acts as a polishing plasma, reducing the scattering losses from the holes sidewalls.

In addition to these data, we measured the effect of a pure Ar treatment, but this did not improve at all the PL intensity, thus confirming that the role of Hydrogen is fundamental in the introduction of optically active centers. We also heated up at 450 °C the samples in a hotplate, after the H_2 treatment and we observed a permanent redshift of the resonance and a drop of the PL intensity. This is another clear proof that Hydrogen is responsible for the PL signal, since it is known that at this temperature H_2 is completely out-diffused from the Si surface.

We performed planar view (PV) and cross-sectional (CS) transmission electron microscopy (TEM) analyses on the PhC and on the SOI layer, by using a JEOL JEM 2010 instrument, equipped with a LaB_6 thermionic source operating at an acceleration voltage of 200 kV. This instrument achieves a nominal spatial resolution of 0.24 nm.

The H_2-treated samples (40 W, 30 min treatment) were prepared by following the conventional methods, reducing their thickness by applying mechanical methods, using a disc grinder, a dimple grinder, an ultrasonic cutter, and ion milling. After this preparation, the samples were analyzed at the microscope.

Fig. 3.10 reports some images recorded in different conditions: panel (a) reports a PV image of the region of the PhC recorded in off-Bragg conditions. The black spots indicate the presence of defects in the sample. It is quite evident that the defects concentration increases remarkably at the hole sidewalls. This is due to the fact that Hydrogen can act in a large surface there. The region close to a single hole was analyzed more carefully and a PV TEM image is reported in panel (b). We can see different kind of defects, mainly platelets (indicated by red arrows) and extended defects (blue circle), i.e. agglomerate of interstitials like dislocation loops. Platelets are two dimensional defects, originated by the presence of Hydrogen inside the crystalline Si lattice. Platelets were already observed for Hydrogen-implanted Silicon [42], and occupy both the (100) planes (parallel to the surface of the wafer) and the {111} planes family, with a length of about 10-15 nm. Moreover the holes sidewalls appear amorphous in the first ~10 nm. We believe that the CHF_3/SF_6 plasma is so strong that it locally amorphizes the Silicon there.

Panel (c) shows a particular dislocation loop, characterized by the typical coffee bean shape. We observed the H_2-treated SOI substrate in CS view. Panel (d) shows a dark field image, reporting the whole top silicon layer of the wafer. In this situation, the presence of defects is associated with a bright contrast with respect to the crystalline silicon. This picture therefore clearly indicates that the defects are located within a depth of 30-40 nm starting from the surface, in accordance with the SEM picture reported in fig.

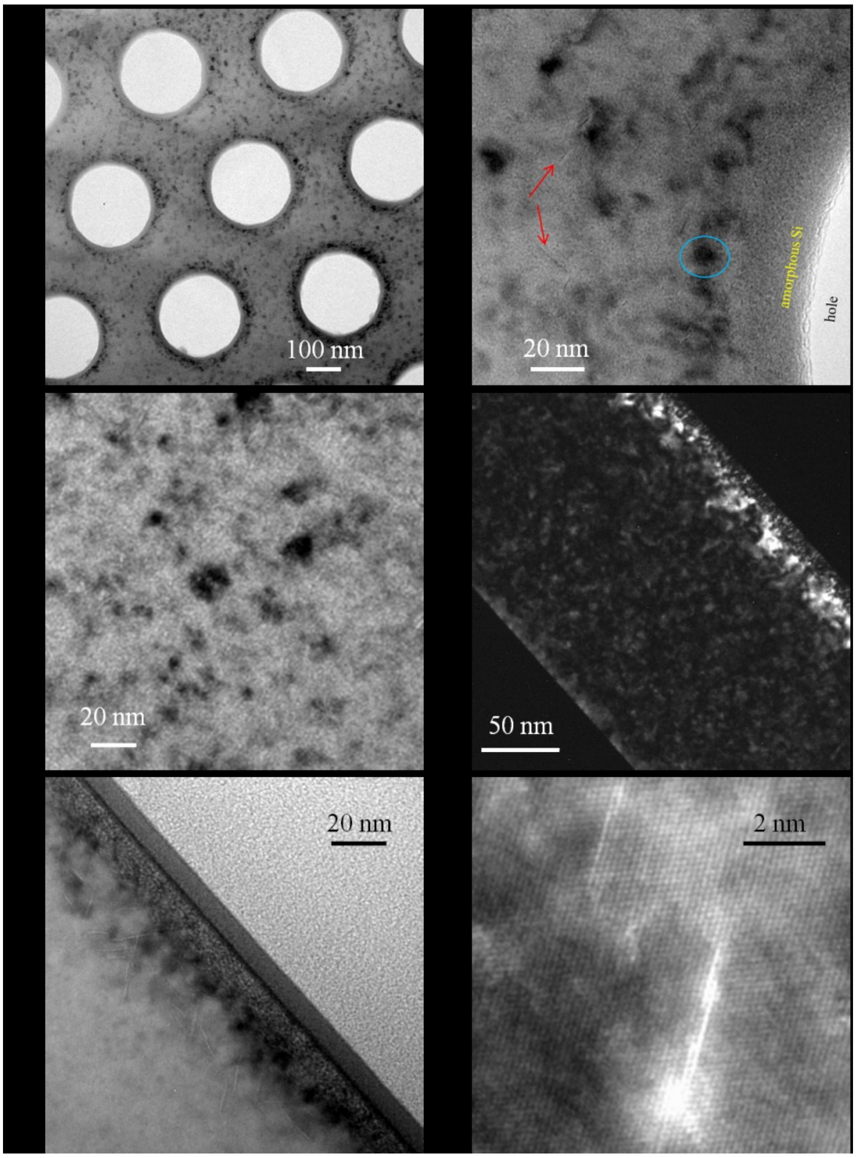

Figure 3.10: PV and CS TEM images of H_2-treated samples. (a) PV on PhC. (b) Region close to a single hole: platelets (red arrows), extended defects (blue circle) and an amorphous zone are visible. (c) Particular coffee bean shape of a dislocation loop. (d) Dark field image, in which defects are evidenced from their brightness. (e) Off-Bragg image of the defects. (f) High resolution image of a platelet.

3.9 (b). The image reported in panel (e) was recorded in off-Bragg conditions, by tilting the sample around the [400] direction, until the diffraction spot became very weak. In this condition, by using a slight defocusing, a mass contrast is highlighted. Particularly we can deduce that the defects present in our sample are characterized by a lower mass with respect to Silicon. This TEM image shows again the kind of defects present in the sample. In fact, beyond the glue necessary for the sample preparation, a thin layer of silicon oxide is present. Immediately below the SiO_2/Si interface, there is some damage: many nanobubbles are clearly evident within a depth of about 10 nm. By considering the mass contrast, it seems that the nanobubbles are an agglomerate of vacancies or they are full of Hydrogen, or both the facts. Going further down in the Silicon layer, we can observe the preponderance the defects observed in PV, the platelet and the extended defects about 10 nm large. Finally a high resolution image is reported in panel (f), in which a couple of platelets are further highlighted. In this latter image the crystalline planes can be observed, and the nature of defects at the nanoscale is visible: it consists of nanometer-sized distortions of the lattice, due to the incorporation of H_2.

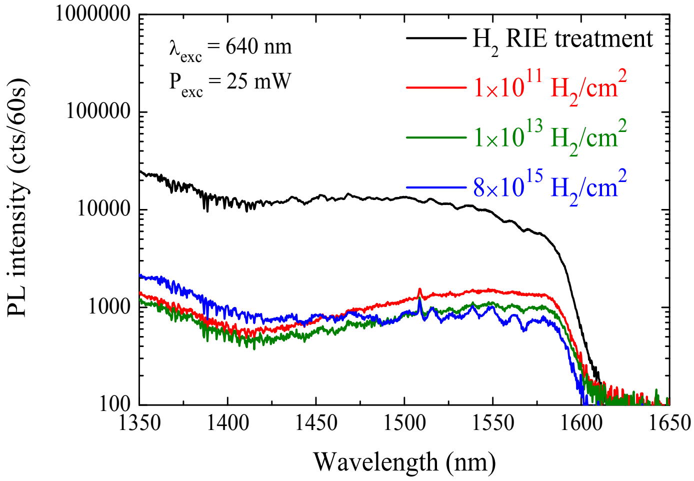

Figure 3.11: PL intensity from SOI implanted with 1×10^{11}, 1×10^{13} and 8×10^{15} H_2/cm^2, compared with the PL from SOI treated with H_2 plasma at 40 W for 30' in RIE.

We also tried to incorporate Hydrogen in another independent way. We implanted H_2^+ ions in bare SOI samples by using a HVEE 400 keV Ion Implanter, at 16 keV with different doses, spanning from 1×10^{11} to 8×10^{15} H_2/cm^3. By using this implantation energy, the Hydrogen dose is peaked at 110 nm inside the SOI, exactly in the middle of the Si layer. In all these cases, however, only a slight enhancement of the broad band emission was registered at high pump powers.

The PL curves are reported in fig. 3.11 and show that there is not any trend with the Hydrogen dose, even by varying it by 6 orders of magnitude. All the curves are much lower in PL intensity than the H_2 plasma treatment. This is probably due to the fact that the plasma treatment at RIE has a double effect: one is the creation of luminescence centers and the other is the passivation of the surface. This is a key point, because it means that the radiative decay rate is likely enhanced by the plasma treatment. Therefore with this procedure we introduce optically active centers increasing at the same time their light emission probability. This does not happens with a strong ion implantation, in which Hydrogen is simply thrown inside the Si slab. There might be the creation of new emitting centers, but the passivation of the surface is not done at all in this way.

3.3 Electrical conduction across a PhC

PhC have been widely used for many applications in photonics, as it was pointed out in the previous chapter. In many cases carrier injection plays a crucial role, for example in modulators [43] and lasers [44], because an efficient injection of the current can seriously improve the performance of the device. For modulators, for instance, it can increase the frequency of operation; for lasers, it can reduce the lasing threshold.

However, despite its undoubted importance, only a few studies on carrier transport through a photonic crystal are reported in literature [45, 46] referred to III-V semiconductors mainly. We will do an accurate study of the physical mechanism of the carrier injection in Si-based PhC, interpreting the results and having in the end good indications for the concrete realization of electrically-pumped PhC-based devices.

3.3.1 Devices fabrication

In order to carry out a complete study of the conductivity across a Si-based PhC, we fabricated p^+-p-p^+ like devices on a SOITEC Silicon-On-Insulator (SOI) wafer, grown by using the Smart-cut process. The as-bought wafer was characterized by an intrinsic resistivity ρ~1-10 $\Omega \cdot$cm, corresponding to a p-type doping level of $\sim 1 \times 10^{15}$ cm^{-3}. The thickness of the silicon layer was 220 nm on a 2 µm thick buried SiO_2 layer.

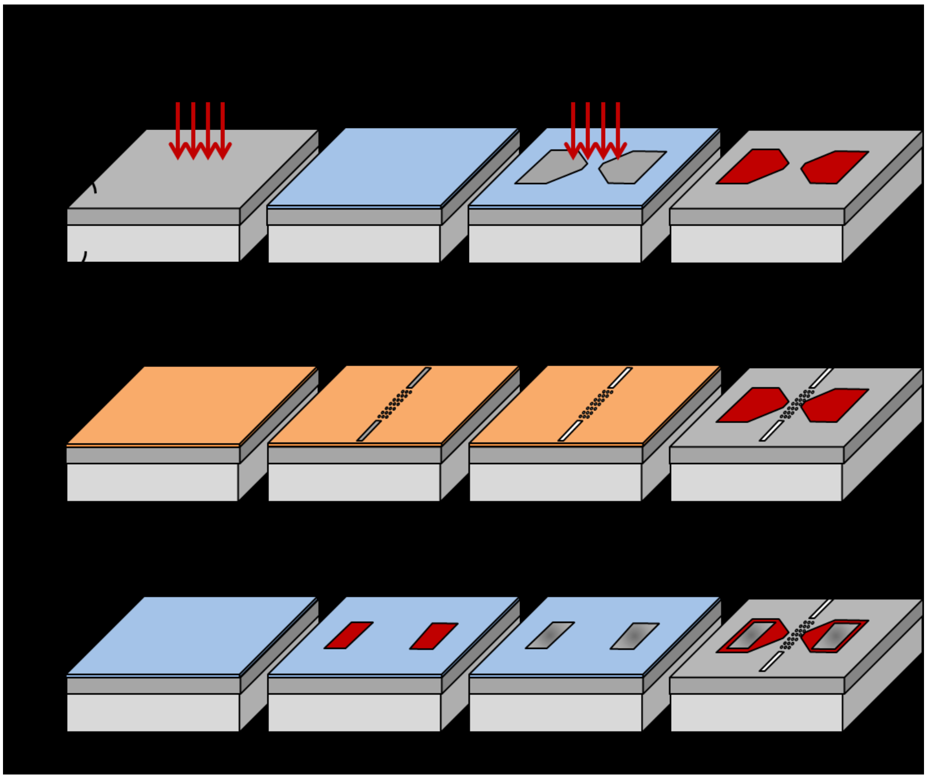

Figure 3.12: Sequence of all the fabrication steps of the PhC devices: multiple ion implantations and standard optical lithography were used for defining the p^+-p-p^+ junction; electron-beam lithography and reactive ion etching were used for the PhC pattern; optical lithography and thermal evaporation of Al were used for depositing the metallic contacts.

The fabrication of these devices was performed by a sequence of optical and electron-beam lithography steps and ion implantations: a schematic of the whole process is depicted in fig. 3.12. Firstly Boron was pre-implanted in the SOI wafer. In particular we performed multiple B implantations at different doses and energies (22 keV, 32 keV and 50 keV) in order to provide a uniform background doping (the p region of the p^+-p-p^+ junction). In the end the background doping level was spanning between 5×10^{16} B/cm^3 and 1×10^{18} B/cm^3. Additionally the devices were realized also in the as-bought wafer, without any pre-implantation.

Afterwards a photolithography step (Shipley S1818 Microposit positive resist ~1.8 μm thick was used as the mask) was performed in order to implant again Boron, for the two p^+ resistive contacts. In this case we chose to perform a single implantation step at 30 keV with 1×10^{19} B/cm^3, since with this single implant good resistive contacts can be realized. By performing sheet resistance measurements on the SOI samples with the four probe method (not shown), we verified that the mask provided by the photo-resist is effective, since it does not allow the ion beam to pass through it. Finally, after removing the mask, we performed a RTA treatment at 1000°C for 30 s in N_2, in order to recover the damage and to activate the dopant [47].

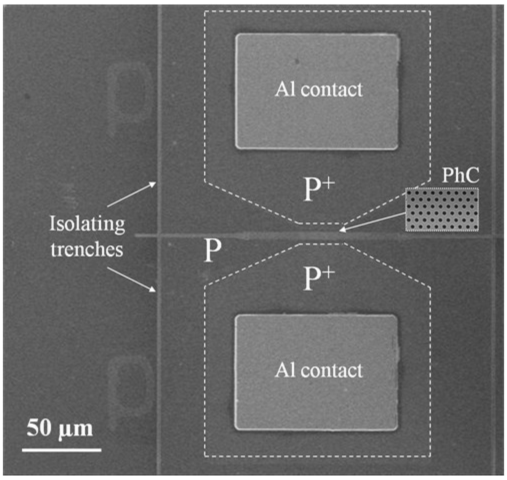

Figure 3.13: SEM picture of the final device, in which the two p^+ pads, the p-region, the PhC pattern, the isolating trenches and the Al contacts are highlighted [48].

The following fabrication steps regard the PhC patterns: they were realized in the p region of the devices using electron-beam lithography with the same recipe already described previously (see section 3.2). Finally, another photolithography step was done, followed by the thermal evaporation of an Al wire, characterized by a purity of 99.99%, and then the aluminum contacts were annealed at 450 °C for 10 min in N_2.

A SEM picture of the final device is reported in fig. 3.13, where the p^+ regions, the contacts, the PhC pattern are highlighted. The p^+ pads are separated by 10 μm. Note also that isolating trenches were etched all around the device, in order to avoid current leakage and to ensure that the electron flow is confined to the photonic crystal as the only possible conductive path.

The PhC pattern is characterized by a triangular lattice and it occupies an area of ~4.5 μm long and 100 μm wide. The geometrical filling factor of the PhC is defined as the ratio between air and the whole volume. In the case of a triangular lattice of lattice parameter *a* and with holes radius *r* it can be written as:

$$ff = \frac{2}{\sqrt{3}} \cdot \left(\quad \right) \tag{3.1}$$

The filling factor was varied by changing the radius *r* and by using two lattice parameters, namely $a = 400$ nm and $a = 800$ nm. The filling factor was estimated by analyzing SEM images, making a statistical analysis of the holes diameter. An ensemble of PhC patterns characterized by $a = 400$ nm and different nominal lattice parameters, namely $r = 70, 90, 110, 120$ nm, is shown in fig. 3.14.

It is worth saying that the actual holes dimension is slightly larger than that designed on the lithography software. This is a systematic error that has to be anyway taken into account. Despite this error, it is important to underline that the holes size is very reproducible, thanks to the well established fabrication procedure for both the electron-beam exposure of the resist and the reactive ion etching recipe. In fact the holes diameter is usually distributed in a Gaussian shape with $\sigma \approx 2\text{-}4$ nm.

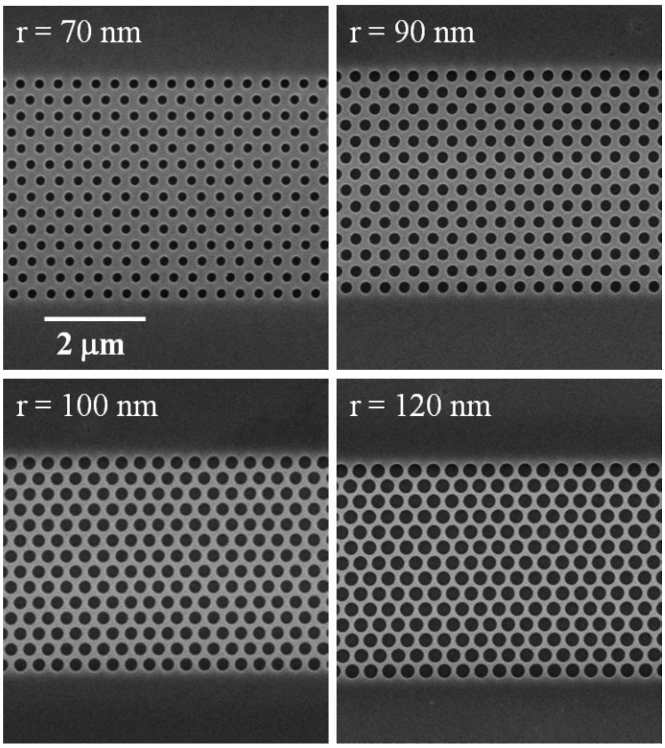

Figure 3.14: SEM pictures of four different PhC patterns, characterized by the same lattice parameter, *a* = 400 nm, but with different nominal holes radius, namely *r* = 70 nm, 90 nm, 110 nm and 120 nm.

Talking in terms of radius, it means that 99.9% of the radii (within the 3σ width of the Gaussian curve) was found to be always within 3-6 nm. A couple of examples, for *a* = 400 nm and nominal *r* = 90 nm and 120 nm are reported in fig. 3.15, where the actual values of the radius (105.6 nm and 138.9 nm, respectively) and of σ (1.4 nm and 1.2 nm, respectively) are shown. Therefore a very good control of *ff* can be achieved, because the error bar in *ff* becomes really negligible.

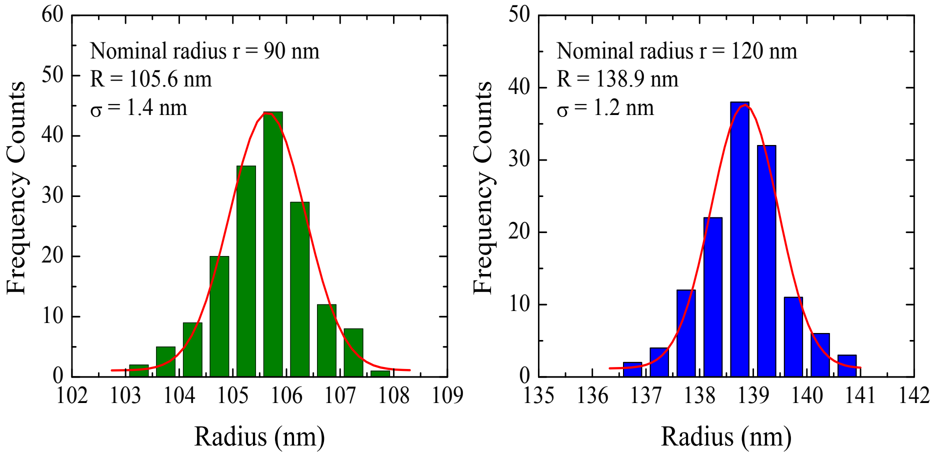

Figure 3.15: Statistical distribution of holes radius for two PhC patterns with *a* = 400 nm and nominal radius of 90 nm and 120 nm. The distributions of the measured size are very narrow, being characterized by σ = 1.0 nm. Note that the actual holes radius is larger than the nominal one, due to the fabrication process.

3.3.2 Electrical characterization

We measured the I-V characteristics of the fabricated devices, by biasing the resistive contacts with metallic probes. The experimental I-V curves are linear and symmetric, as shown in fig. 3.15 for a background doping 6×10^{17} B/cm^3 and for different filling factors. The linearity is due to the fact that this device is basically a resistor. On the other hand, the symmetry is due to the fact that the device is symmetric and forward or backward biasing are the same.

The resistance is given by the slope of the I-V curve and it includes the resistance of the PhC, the unpatterned silicon, and the contacts. The contact resistance was estimated by Transmission Line Measurements (TLM) and it is of about 300 Ω. Additionally we fabricated the very same device without photonic crystals, as reference samples, named in the fig. 3.16 as *ff* = 0 %, for all the doping levels investigated. The resistance clearly increases by increasing the air filling factor, and this is due to the fact that the holes become closer and closer, thus reducing the space available for the electrical conduction.

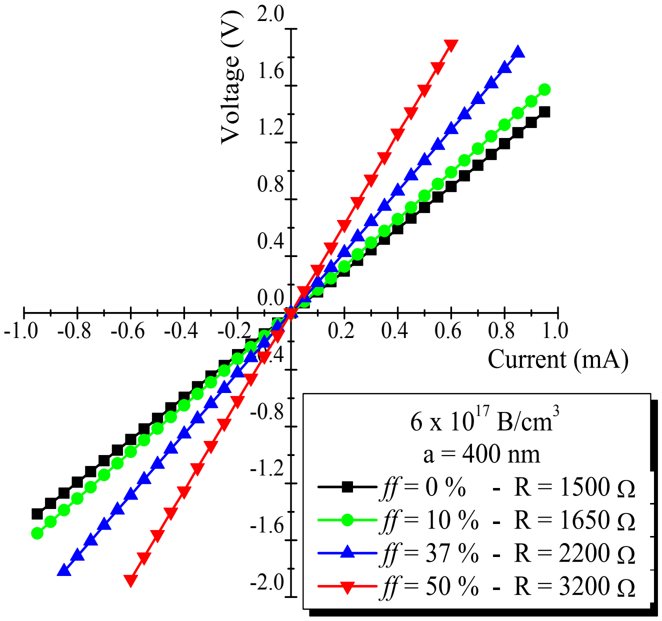

Figure 3.16: I-V curves of a sample with a background doping of 6×10^{16} B/cm^3. The curves refer to four different PhC patterns, with the same lattice parameter (*a* = 400 nm) but with different holes' radius (or equivalently, different *ff*).

A summary of the resistance data (for *a* = 400 nm) as a function of *ff*, expressed in %, is presented in fig. 3.17. The error bars were found by doing a statistical distribution of the resistances, by applying the probes in different points of the metallic contacts. For each point five measurements were made. For a given filling factor, the resistance decreases by more than two orders of magnitude from the as-bought SOI (~1×10^{15} B/cm^3) to the highest boron concentration (1×10^{18} B/cm^3), as a result of the decreasing resistivity. In fact resistivity is 0.041 Ω·cm for the highest B concentration, rising to 0.345 Ω·cm for the lowest dose implanted. The resistance then increases dramatically with increasing *ff*, as already observed.

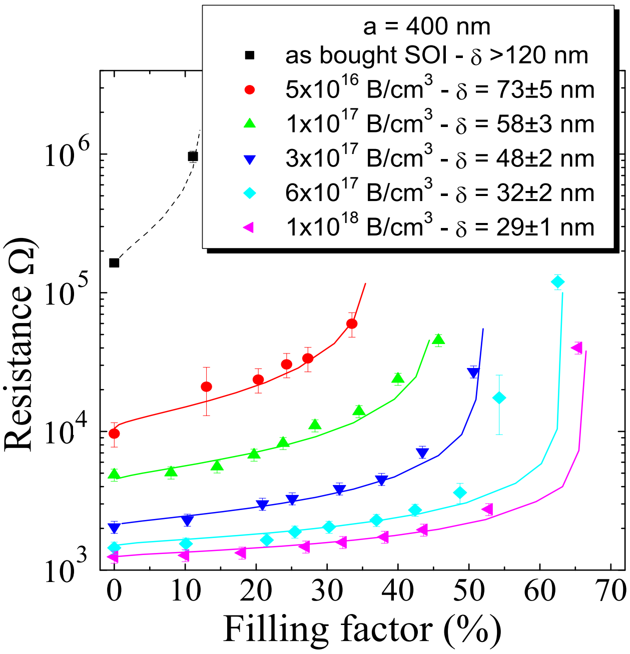

Figure 3.17: Total device resistance (data points) as a function of both the background doping and the PhC air filling factor (keeping fixed *a* = 400 nm). The curves are obtained with COMSOL simulations and the extrapolated *δ* regions are indicated for all the doping levels, with the exception of the as-bought SOI, for which there was insufficient data points [48].

Naïvely, one would expect the curves to diverge (i.e. resistance going to infinity) when the holes touch one another, as the conduction path is completely pinched off at this point. This corresponds to the condition $2r = a$, that is a *ff* ≈ 90%, according to Eq. (3.1). This value is geometrical and it should not depend on the background B concentration. This is clearly not the case, and the curves in fig. 3.17 show that the divergence point strongly depends on the background doping level. For low doping concentration (5×10^{16} B/cm^3) the resistance starts to increase for filling factors as small as *ff* ≈ 30%, while for a relatively high doping concentration (1×10^{18} B/cm^3) the resistance stays low until approximately *ff* ≈ 60%. This suggests that the effective electrical size of the holes is larger than their physical size and that it strongly depends on the doping concentration [48].

With the aim of properly fitting the experimental points, we added an additional electrically inhibited region of dimension *δ*, whose value is also a function of doping. The data points were then fitted by using a COMSOL™ simulation for each doping density, shown as continuous lines in fig. 3.17. From the fits it turned out that *δ* decreases from 73 nm (for 5×10^{16} B/cm^3) to 29 nm (for 1×10^{18} B/cm^3). It was impossible to extrapolate a value for the as-bought SOI, because there were only two points available, but we are able to say in this case that this region is at least 120 nm [48].

3.3.3 The depletion region

We understood that there is an additional electrically isolated region. What is the physical meaning of *δ*? Where does it come from? The answer lies in the fabrication process that led to the realization of the PhC pattern. In fact reactive ion etching provides a very strong physical etching of silicon. This severe process certainly introduces many defects at the holes sidewalls, deeply modifying their surface potential.

We believe that these defects are so many that they fill the silicon band gap, thus pinning the Fermi level position at the surface exactly in the middle of the gap. Moreover we know that far away from the surface, being the silicon doped with B, the Fermi level is close to the valence band. Thus an effect similar to that occurring in MOS structures [49] happens: a depletion region is formed exactly around the holes. This depletion region is an electrically inhibited region for carriers, therefore the holes electrical size is larger than their physical extension. It is possible to calculate this depletion region, that we call Δ, by using Poisson's equation:

$$\Delta = \sqrt{\frac{2\varepsilon\varepsilon}{eN_A}\Phi} \tag{3.2}$$

where ε_r is the relative dielectric constant of silicon, ε_0 is the dielectric permittivity in vacuum, *e* the electron charge, Φ_i is the internal potential of the semiconductor and N_A the boron concentration. The dependence of Δ on the doping is not just the one directly expressed in Eq. (3.2), because also Φ_i is a function of N_A:

$$\Phi = \frac{k\ T}{e}\left(\qquad\right) \tag{3.3}$$

being k_B the Boltzmann constant, T the temperature, n_i the intrinsic carrier concentration of the semiconductor. For Silicon this number is 1.4×10^{10} /cm^3 at room temperature. A schematic of the situation is depicted in fig. 3.18, where the depletion region around the air hole is emphasized. In this picture the position of the Fermi level, E_F, and of the intrinsic level, E_i, are also indicated.

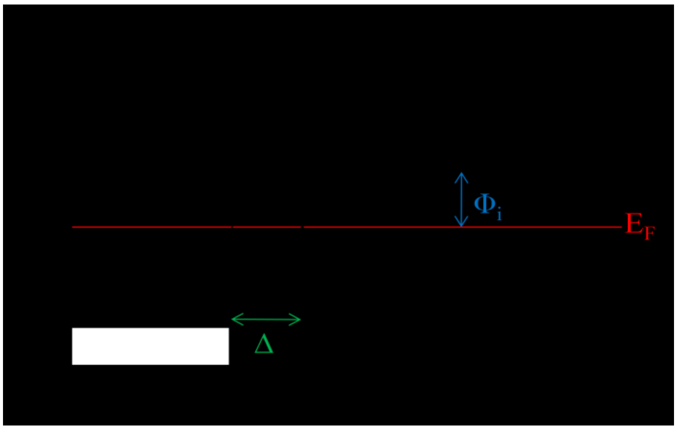

Figure 3.18: Schematic of the air-silicon interface. The hole is an air cylinder. At its interface the Fermi level E_F has to be in the middle of the Si energy gap. On the other hand, in the bulk silicon, E_F is close to the valence band. This band pinning justifies the existence of a depletion region Δ around the hole.

It is now possible to compare the Δ calculated with Eq. (3.2) with the δ obtained by the best fits of the experimental data, for all the Boron concentrations investigated. For example, for a doping density of N_A = 3×10^{17} B/cm^3, in the middle of the range investigated, and for a = 400 nm, δ = 48 ± 2 nm, while Δ = 44 nm, so they are in good agreement, demonstrating that indeed the enlargement in the electrical size of the holes is produced by band pinning (similar agreement was found for the other doping levels) [48].

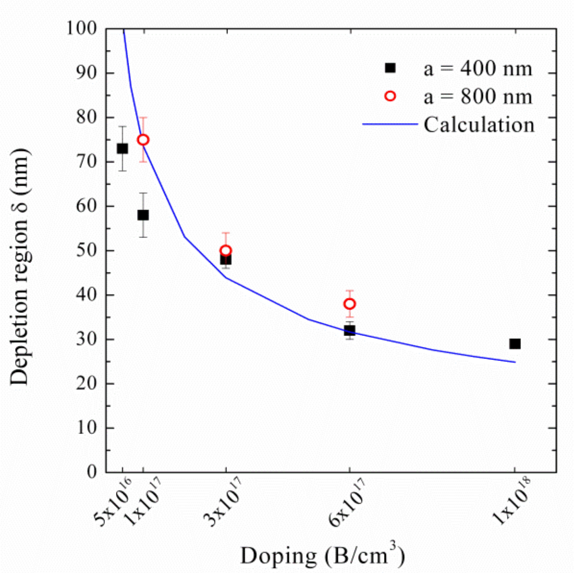

Figure 3.19: Comparison of the extrapolated values of δ for both the lattice constants (red and black data points) and the calculated depletion region Δ (blue continuous line), as a function of the Boron concentration.

A comparison of Δ and δ is reported in fig. 3.19 for both lattice parameters investigated, showing that actually the agreement between model and experiment is good for all the background doping levels: we can conclude therefore that Δ is δ indeed. We believe that such depletion region also exists for the top surface of the SOI, but that surface has not been exposed to a dry etching process, being covered by the e-beam resist layer, so the band pinning effect there is expected to be much weaker. Moreover a similar depletion region around etched holes has already been observed in Indium Phosphide [45] and Gallium Arsenide [46] photonic crystal devices.

An interesting comparison can now be made with the electrical properties of a shallow etched region, as both photonic crystals and shallow etching can be used to confine light. Which one of the two methods is better from an electrical point of view has not yet been made clear. Therefore we have investigated the resistance of some etched shallow trenches, characterized by a fixed etch depth and different lengths. These trenches are typically used to define rib waveguide based ring resonators [50].

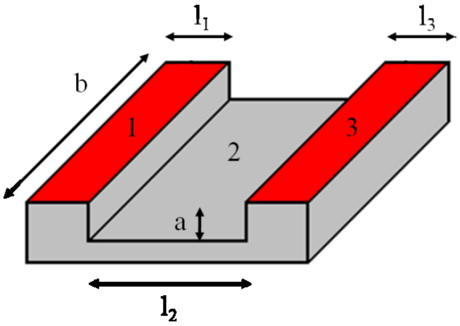

Figure 3.20: Schematic of the shallow trenches etched down in the Si layer, instead of the PhC pattern.

A schematic of the trenches is reported in fig. 3.20. We fixed a = 135 nm (verified by Atomic Force Microscopy) by controlling the etching time of the Si layer, and b = 100 μm, as designed with e-beam lithography. On the other hand we varied the length of region 2 from 1 to 10 μm, and consequently of regions 1 and 3, which are the same symmetrically. All the three regions lye in the p-type part of the p^+-p-p^+ junctions, replacing exactly the PhC pattern. Therefore $l_1+l_2+l_3=10$ μm, according to the device depicted in fig. 3.13.

The resistance *R* of this new device can be calculated analytically:

$$R=\rho\left(\frac{l_1}{S_1}+\frac{l_2}{S_2}+\frac{l_3}{S_3}\right)+R_{contact} \tag{3.4}$$

where ρ is the resistivity of the p-region, S_i, i = 1, 2, 3, are the transverse sections of the Si layer passed by the electron flow and $R_{contact}$ is the contact resistance. We can put together regions 1 and 3, characterized by the same transverse section, thus writing:

$$R=\rho\left(\frac{l_1+l_3}{S_1}+\frac{l_2}{S_2}\right)+R_{contact}=\rho\left(\frac{l_{tot}-l_2}{S_1}+\frac{l_2}{S_2}\right)+R_{contact} \tag{3.5}$$

By separating the resistance R_0 of the reference device, without PhC or trenches, i.e. the resistance of the simple junction p^+-p-p^+, and by considering that the thickness of the Si layer is 220 nm, we get:

$$\begin{aligned} R &= \left[\rho\left(\frac{l_{tot}}{S_1}\right) + R_{contact}\right] + \rho\left(\frac{1}{S_2} - \frac{1}{S_1}\right) = \\ &R_0 + \frac{\rho}{b}\left(\frac{1}{220nm - a - \delta} - \frac{1}{220nm}\right) \end{aligned} \tag{3.6}$$

We can arrange in another way this equation, in order to be able to fit some data points:

$$R - R_0 = y = c\left(\frac{1}{85nm - \delta} - \frac{1}{220nm}\right)x \tag{3.7}$$

This is our equation, in which we have: an independent variable *x*, which is the length we varied l_2, some known parameters R_0 and *c* (equal to ρ/b), a dependent variable *y*, which is measured by measuring *R*, and finally δ, which is the fitting parameter. So the values of δ can be determined from the slope of a resistance-width plot, but δ now refers to the surface rather than the sidewall depletion layer.

By using Eq. (3.7) we fitted the data points for some doping levels and the experimental results are shown in fig. 3.21 (a). Note that the numbers obtained from the fit are quite similar to those obtained for the PhC holes for doping levels between 3×10^{17} and 1×10^{18} B/cm^3.

In order to compare the electrical performances of the PhC with respect to the shallow trenches, we plotted the resistance of a typical photonic crystal pattern, characterized by a *ff* = 30%, together with the resistance of a shallow etched trench, of the same length, i.e. 4.5 μm. As we can see in fig. 3.21 (b) the PhC has a resistance consistently lower than that of the shallow trench.

This result proves that the depletion layer is an important issue. It must be considered for any type of electrically active nanophotonic device, which requires etching steps in the fabrication procedure. We demonstrated also that it is possible to achieve a more than two orders of magnitude improvement of the electrical conductivity of SOI and a strong reduction of this depletion region, by performing a relatively heavy (1×10^{18} B/cm^3) doping.

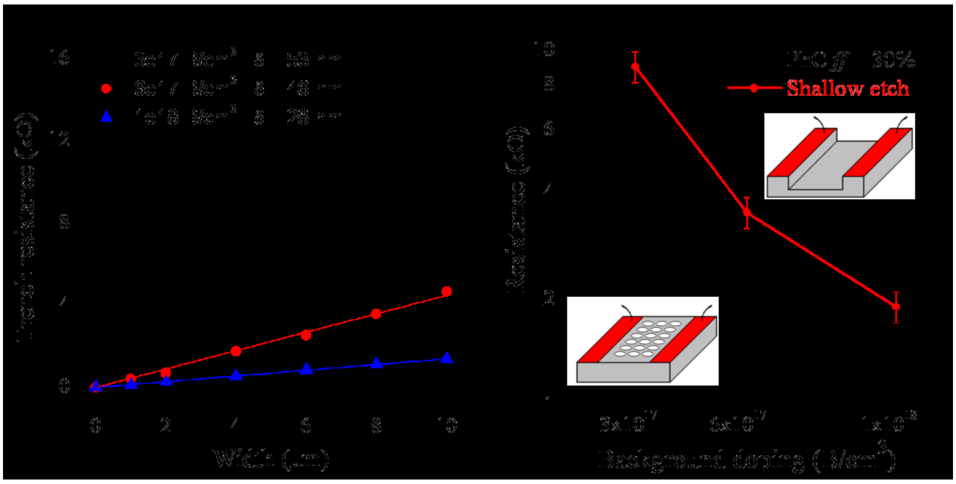

Figure 3.21: (a) Trench resistance as a function of the width (l_2) for three different p-type doping levels. The continuous lines are the linear fits to the data points according to Eq. (3.7). (b) Resistance versus doping density, comparison of PhC with shallow etched trenches. The device length is 4.5 μm in both cases. For a typical air filling factor (*ff* = 30%) the resistance through a PhC is considerably lower [48].

Additionally we demonstrated that PhC are characterized by a lower resistance per length values with respect to the shallow trenches, typically used for modulators. Therefore by considering a modulator with a fixed geometry, PhC allow a better carrier injection in the active region, being more promising for realizing efficient devices [48].

3.4 Quality factor of highly doped SOI PhC L_3 nanocavities

It is clear from the electrical characterization showed in the previous section that increasing doping concentration reduces the resistivity. A high doping level, however, means a high number of free carriers available in the material. Therefore it is expected that optical losses also increase, being carriers strong light absorbers. So there must be a trade-off between electrical and optical properties of doped devices.

In this section, we explore the effect of doping on the cavity losses by measuring their Q factor. For each background doping level analyzed before (from 5×10^{16} to 1×10^{18} B/cm^3, plus the as-bought SOI sample, doped with ~1×10^{15} B/cm^3), we realized L_3 nanocavities, with a lattice parameter of 420 nm and *ff* ≈ 28% that operate at wavelengths around 1.5 μm. These cavities were realized as air-bridges, i.e. by membraning the SOI PhC slab, leaving the samples for 20 min in a 5:100 HF:H_2O solution. HF penetrates in the holes already etched, thus removing the underlying SiO_2 layer. A clear SEM image of this membrane is shown in fig. 3.22 (a), where one of the cavities is shown. Note the shadow all around the PhC pattern: this is the electronic contrast due to the fact that far away from the PhC (below it) there is still the sustaining SiO_2 layer, while it does not exist anymore under the PhC pattern.

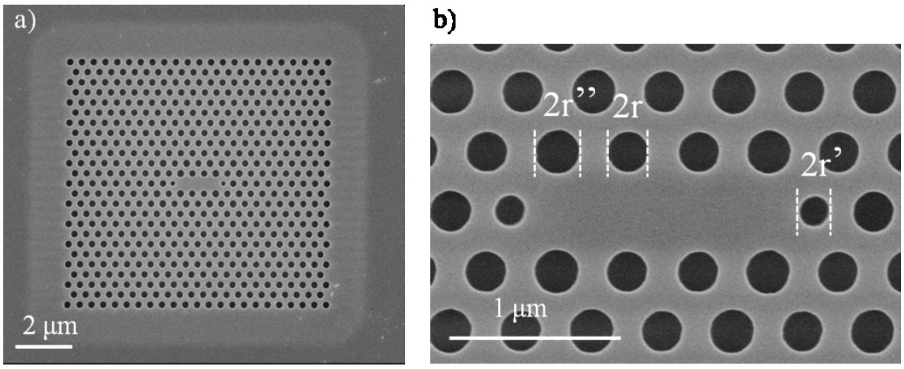

Figure 3.22: (a) SEM image presenting a membraned L_3 cavity. The shadow around the structure indicates how far the HF-based solution penetrates into the SiO_2 layer. (b) Zoom in the cavity region [48]. The radius of the holes (*r*), the enlarged holes for far-field (*r''*) and the side holes for gentle confinement (*r'*) are evidenced.

We designed the cavities with the far-field optimization as discussed in section 2.3.5, using hole enlargements of 0, +3 and +9 nm to improve the out-of-plane coupling efficiency. This hole enlargement ($\Delta r'' = r''-r$) is visible in the SEM image shown in fig. 3.22 (b), in which a cavity is pictured in detail. On the other hand, the end holes at the sides of the cavities were reduced in size by (*r'*-*r*)/*a* = 0.06 and shifted outwards by $\Delta x/a$ = 0.16 to implement the gentle confinement effect, which allows the achievement of very high Q factors [51], as discussed in section 2.3.2.

We characterized the cavities from the optical point of view by measuring their quality factor Q, using the resonant scattering technique [40]. By using this technique, in general, asymmetric Fano shapes are observed, following the relation:

$$F(\omega = \quad + \quad \frac{\quad - \quad \Gamma}{1+ \quad - \quad \Gamma} \tag{3.8}$$

where q is the Fano parameter regulating the asymmetry of the curve, A_0, F_0 are constant factors, ω_0 is the peak wavelength and Γ is the FWHM of the peak. The Q factor is given by the ratio ω_0/Γ.

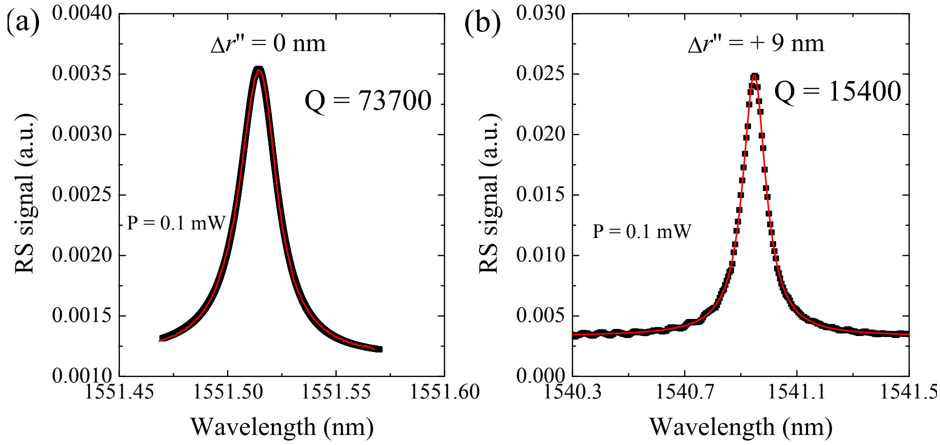

Figure 3.23: RS measurements from a cavity, realized in the as-bought SOI, without far-field optimization (a) and with a hole enlargement of +9nm (b). The red curves are the Fano fits using Eq. (3.8).

We reported in fig. 3.23 two RS spectra referred to the cavity without far-field optimization (a) and the cavity with hole enlargement $\Delta r''$ = +9 nm (b), both for the as-bought SOI cavity. It is evident from the graphs that increasing the holes size results in a decrease of the Q factor, since there is a strong out-of-plane coupling and light can escape from the cavity.

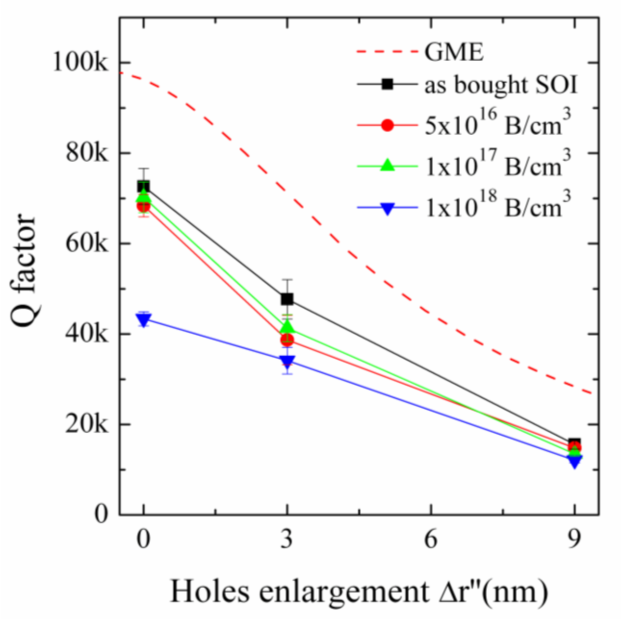

Figure 3.24: Q factor as a function of the holes enlargement for four different doping levels. A calculation performed by using the guided-mode expansion is also reported [48].

A summary of all the experimental Q values are shown in fig. 3.24 for four different doping levels as a function of the Δ*r*’’ parameter and are compared with a calculation, obtained by using the guided-mode expansion (GME) method. Details on this method can be found in ref. [52]. Each experimental point has been obtained by measuring five cavities for each sample; the error bars are also shown and are due to statistics. For doping concentrations up to 1×10^{17} B/cm^3 the Q factors are little affected by doping, and display the same trend as the theoretical curve, i.e. they drop steadily from the maximum value of 75k (theoretical value ~100k) with increasing Δ*r*’’, i.e. by increasing the out-of-plane coupling. As the doping level is raised to 1×10^{18} B/cm^3 , a more pronounced reduction of the Q factor is observed for the cavity without far-field optimization (Δ*r’’*= 0 nm), which nevertheless keeps at the remarkable value of 40k. We also notice that for the case of $\Delta r''$= +9 nm, the Q factor (~15k) does not change significantly even for the highest boron concentration. For this design, the coupling efficiency is estimated to be about 30% [40], which means that the coupling loss is much higher than the absorption loss introduced by the doping.

Therefore we can conclude that a relatively high doping level does not affect too much the experimentally measured unloaded Q of L_3 PhC cavities. This is very important if we want to dope deeply inside the PhC pattern in order to achieve an efficient electroluminescence, for instance from an emitter inside the cavity.

3.5 Highly efficient electrically driven Si-based nanolight source

We have discussed in the previous sections how it is possible to create a defect in Silicon which leads to a strong photoluminescence (PL) intensity at room temperature at telecommunication wavelengths. This kind of defect can be easily introduced by performing just a plasma treatment in a PhC cavity. Though the PL is very intense, it can be very hard in some cases to achieve electroluminescence (EL) from the same source. EL can be obtained if and only if an efficient electron-hole recombination occurs where the defect is present. The only way to achieve it is to realize a system where carriers are not wasted in heating up the devices and where they do not recombine in the wrong place.

We analyzed in detail how the current flows across a PhC and we demonstrated that it is possible to have a relatively high doping level (up to 10^{18} B/cm^3), thus increasing the conductivity, reducing the depletion region, without losing too much in the optical confinement of a L_3 cavity.

We used all this information to carry on the fabrication of a good light emitting device, like that depicted in fig. 3.25. This device was realized by performing a procedure very similar to that already discussed in the previous section. The main difference is that this is a p-i-n junction, where the p resistive contact was obtained by performing the very same Boron implantation described before (10^{14} B/cm^2 at 30 keV), while the n resistive contact was obtained by using the very same dose of Phosphorous (but at 75 keV, being this ion much heavier than Boron). Thus the two pads have a dopant concentration of 1×10^{19} B/cm^3 and 1×10^{19} P/cm^3 respectively.

The two doped pads have a finger-like arm in the end (about 1 µm wide) and these arms are separated by a 500 nm distance, which was carefully controlled by electron-beam lithography. In this no man’s land, Si is slightly p-type doped (~1×10^{15} B/cm^3), being this the original doping level of the as-bought wafers. For the sake of simplicity we will refer to this part as the intrinsic section of the junction.

The PhC pattern was etched down between the p and the n pad and a L_3 cavity was designed exactly in the 500 nm-intrinsic spacing. The scheme of the design in a TCAD-like system is reported in fig. 3.24 (b). In this picture the black lines are some trenches which are etched down to the buffer SiO_2 layer of the SOI wafer, in order to avoid current leakage. A SEM picture is shown also (see panel (c)) to highlight the actual core of the device: the fingers, the PhC cavity and the isolating trenches.

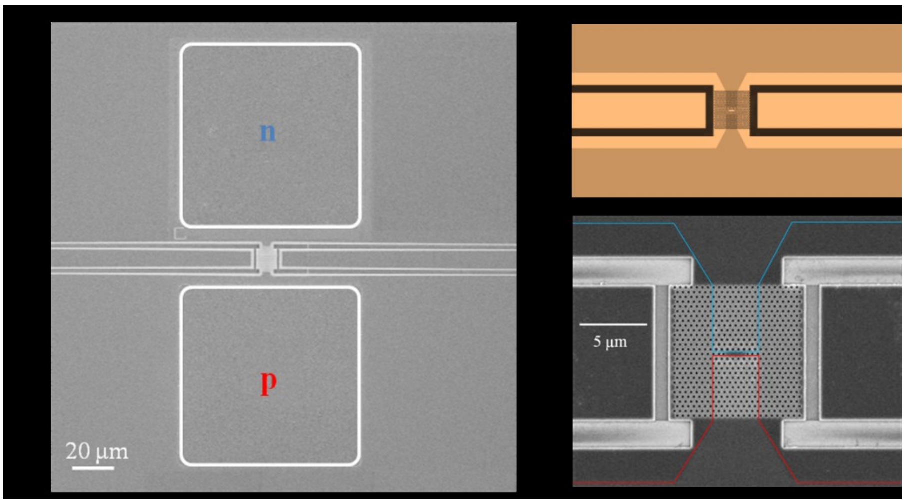

Figure 3.25: (a) SEM picture of the p-i-n device realized for electrically pumping H_2-related defects. (b) Scheme of the device in which the finger-like doped arms are highlighted. (c) SEM picture of the cavity region: the doped arms and the trenches for reducing current leakage are also shown.

After the realization of the resistive contacts and of the PhC cavity, the sample was rinsed in an HF-based solution to membrane the PhC, with the aim of keeping good optical performances of the cavity. Then Al contacts were deposited and annealed at 450 °C for 10 minutes in N_2.

After that, the best plasma treatment (40 W, 30 min, H_2 plasma) was performed in the reactive ion etching, in order to deliberately insert H_2-related defects, as discussed previously. In fact, we have already shown that this plasma treatment improves by several orders of magnitude the PL intensity of the PhC cavity. We had to perform this step at the end of the whole fabrication procedure, because the thermal treatment required for the interdiffusion at the Al/Si interface certainly induces an out-diffusion of Hydrogen from the Si-slab, thus reducing the number of emitting centers.

The particular design of our device was chosen for two main reasons. First of all, the finger like contacts allow an effective injection of carriers mostly in the cavity region, due both to the low resistivity of the arms and to the useful contribution of the isolating trenches. The second reason is that the cavity is in this way in the intrinsic region, which is thought to be fully depleted of carriers already at equilibrium. In fact the depletion region at equilibrium of a junction with 1×10^{19} P/cm^3 and $\sim1\times10^{15}$ B/cm^3 is about 1 μm. We kept however a distance of 500 nm since the doping level of the wafers is not known perfectly and might be a bit higher than 1×10^{15} B/cm^3. This is very important because the depletion region of the junction is the place where most of the electron-hole recombinations occur. Therefore we think this is a key point for obtaining an efficiently-pumped light emitting device.

We measured the electroluminescence intensity by applying a forward polarization voltage across the junction and collecting the emitted light with the same experimental apparatus used for PL measurements from the Hydrogen-related defects. Using the same set up allows a direct comparison between PL and EL emission intensities from the device. An intense EL signal is already observed by applying just 1 V bias. In fig. 3.26 (a) we report the maximum (saturation) power spectral density expressed in pW/nm across the wide spectral range from 1100 nm to 1600 nm for both PL and EL. Photoluminescence is recorded at a pump flux of 0.8 mW under excitation at 640 nm. Electroluminescence is recorded at an applied voltage of 3.5 V, with a current of 156.5 μA. Thus this device consumes an electrical power of 0.55 mW. The signal is a superimposition of the cavity modes, i.e. the sharp peaks, over the broadband background emission from the plasma treated SOI. All the cavity modes can be found both in PL and in EL.

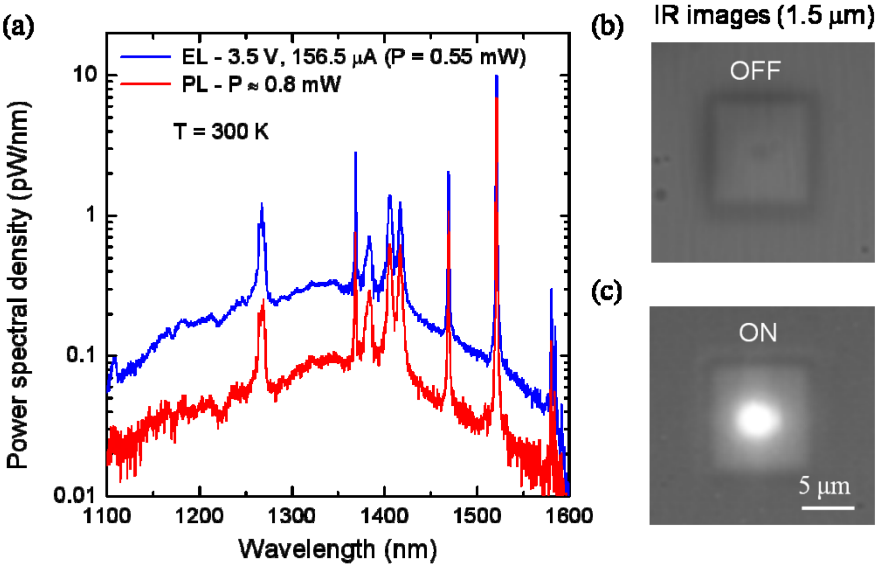

Figure 3.26: (a) Comparison between PL and EL in the saturation regime. Note that 10 pW/nm is reached with EL in forward bias. We also report IR images in OFF (b) and ON (c) state before and after applying a voltage to the device.

Surprisingly, the EL signal is more intense with respect to the PL signal in the whole spectral range investigated, thus indicating the occurrence of a very efficient carrier injection and radiative recombination in the device. It is worth noticing also that in the fundamental cavity mode (at 1521.38 nm for this particular cavity) the spectral density reaches the remarkable value of 10 pW/nm. At that point the linewidth is just 0.5 nm, which is even lower than the linewidth of the III-V nanolaser reported in ref. [53]. Additionally by integrating the curve, the total emitted power is 130 pW in the EL case, while it is 3 times lower in the PL case.

We did not observe linewidth narrowing, which suggests that a lasing threshold has not been reached, so despite the high Purcell factor, the free carrier absorption still outweighs the optical gain. However, though this is not a laser, the emitted spectral density are by far the highest values ever registered in a Si-based electrically-driven nanolight source, working at room temperature and at telecom wavelengths. The emission intensities registered are even comparable with III-V lasers working at cryogenic temperatures [53]. Moreover we notice that the device does not heat up under electrical bias, as demonstrated by the absence of any redshift of the cavity peak between PL and EL.

Figure 3.26 reports also IR images of the device under zero voltage applied (b) and 3.5 V applied (c). The images are registered with an IR camera and the very intense emission spot is clearly visible as soon as the voltage is turned on.

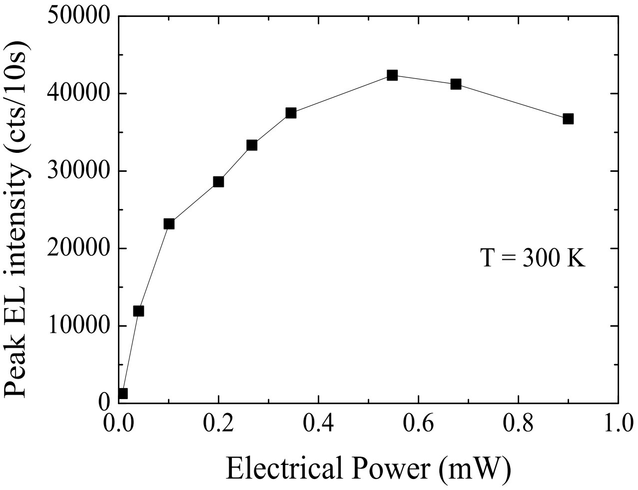

Figure 3.27: EL intensity of the fundamental cavity peak as a function of the electrical power applied. After a saturation at 0.8 mW, the EL intensity decreases because the H_2-related defects anneal out.

We measured the EL intensity of the fundamental cavity mode as a function of the electrical power injected in the device and the data points are reported in fig. 3.27. The intensity starts to increase by raising the voltage applied (and the current consequently); the maximum EL intensity value is reached at about 0.55 mW at 3.5 V applied, and then it decreases because the device starts heating, the cavity peak slightly redshifts (not shown) and the H_2-defects anneal out, thus reducing the number of emitting centers.

We also measured the quality factor of the L_3 cavities under electrical excitation. This experiment was done by using the resonant scattering technique while a bias voltage was applied at the same time. The Q factor was found to be about 4000. The value is a bit lower than those reported in fig. 3.24. We believe this is due to a higher free carrier absorption, owing both to the carriers injected during the electrical pumping and to the high number of free carriers introduced by the strong level of doping.

Conclusions

In conclusion, we have found an interesting way to produce defects in Silicon. By performing a reactive ion etching process with Hydrogen, some optically active centers were incorporated in a SOI wafer, resulting in an intense photoluminescence signal. This signal is further enhanced in presence of a PhC pattern, owing to the benefits of these structures.

After a deep analysis of the electrical conduction across a PhC we found that a depletion region exists around the holes, due to the severe physical process of the etching, and we modeled this effect, by performing some simulation of the current flow. We also found that by doping the SOI with a relatively high doping level, the resulting optical properties of PhC nanocavities are just slightly modified. By using all this information, we found an efficient way for the achievement of the up-to-date most efficient electrically driven nanolight source in Silicon, working at room temperature around telecommunication wavelengths, and also potentially tunable. The emitters are the H_2-related defects, obtained by plasma treatment at RIE and we have shown that they can be actually electrically excited.

We registered in EL for the fundamental cavity mode a spectral density of 10 pW/nm, an extremely high number for Silicon at room temperature, even larger than the value obtained in PL, by applying just 3.5 V to the junction. Moreover we found the narrowest line ever measured for Silicon (0.5 nm). The total emitted power of our device in the near infrared range is 130 pW. This device has therefore performances even comparable with III-V PhC nanolasers. Though we did not realize a laser, we achieved a very efficient Si-based LED, and this remarkable result is due to a perfect injection of carriers, recombining exactly in the middle of a PhC nanocavity. We believe therefore that the so-fabricated prototype can be considered an important milestone for the optoelectronic devices based on the Silicon technology.

References

[1] P. Y. Yu and M. Cardona, *Fundamentals of semiconductors*, Springer Berlin, 1996.

[2] R. B. Hammond and R. N. Silver, Appl. Phys. Lett. **36**, 68 (1980).

[3] M. A. Tamor and J. P. Wolfe, Phys. Rev. Lett. **44**, 1703 (1980).

[4] R. N. Hall, Phys. Rev. **87**, 387 (1952).

[5] W. Shockley and W. T. Read, Phys. Rev. **87**, 835 (1952).

[6] J. T. Cuthbert, Phys. Rev. B **1**, 1552 (1970).

[7] M. A. Green, J. Zhao, A. Wang, P. J. Reece and M. Gal, Nature **412**, 805 (2001).

[8] J. Zhao, M. A. Green and A. Wang, J. Appl. Phys. **92**, 2977 (2002).

[9] W. L. Ng, M. A. Lourenço, R. M. Gwilliam, S. Ledain, G. Shao and K. P. Homewood, Nature **410**, 192 (2001).

[10] C. Kittel, *Introduction to Solid State Physics*, John Wiley & Sons, New York, 1996.

[11] R. Clap, D. Dimitropoulos, V. Raghunathan, Y. Han and B. Jalali, Opt. Expr. **11**, 1731 (2003).

[12] R. L. Espinola, J. I. Dadap, R. M. Osgood Jr., S. J. McNab and Y. A. Vlasov, Opt. Expr. **12**, 3713 (2004).

[13] Q. Xu, V. R. Almeida and M. Lipson, Opt. Expr. **12**, 4437 (2004).

[14] H. Rong, A. Liu, R. Jones, O. Cohen, D. Hak, R. Nicolaescu, A. Fang and M. Paniccia, Nature **433**, 292 (2005).

[15] H. Rong, R. Jones, A. Liu, O. Cohen, D. Hak, A. Fang and M. Paniccia, Nature **433**, 725 (2005).

[16] T. Inokuma, Y. Wakayama, T. Muramoto, R. Aoki, Y. Kurata and S. Hasegawa, J. Appl. Phys. **83**, 2228 (1998).

[17] F. Iacona, G. Franzò and C. Spinella, J. Appl. Phys. **87**, 1295 (2000).

[18] G. Franzò, A. Irrera, E. C. Moreira, M. Miritello, F. Iacona, D. Sanfilippo, P. G. Fallica and F. Priolo, Appl. Phys. A **74**, 1 (2002).

[19] R. J. Walters, G. I. Bourianoff and H. Atwater, Nature Mater. **4**, 143 (2005).

[20] A. Irrera, D. Pacifici, M. Miritello, G. Franzò, F. Priolo, F. Iacona, D. Sanfilippo, G. Di Stefano and P. G. Fallica, Appl. Phys. Lett. **81**, 1866 (2002).

[21] C. D. Presti, A. Irrera, G. Franzò, I. Crupi, F. Priolo, F. Iacona, G. Di Stefano, A. Piana, D. Sanfilippo and P. G. Fallica, Appl. Phys. Lett. **88**, 33501 (2002).

[22] L. Pavesi, L. Dal Negro, C. Mazzoleni, G. Franzò and F. Priolo, Nature **408**, 440 (2000).

[23] A. Polman, G. N. van den Hoven, J. S. Custer, J. H. Shin, R. Serna and P. F. A. Alkemade, J. Appl. Phys. **77**, 1256 (1995).

[24] G. Franzò, S. Coffa, F. Priolo and C. Spinella, J. Appl. Phys. **81**, 2784 (1997).

[25] S. Coffa, G. Franzò and F. Priolo, Appl. Phys. Lett. **69**, 2077 (1996).

[26] R. Serna, J. H. Shin, M. Lohmeier, E. Vlieg, A. Polman and P. F. A. Alkemade, J. Appl. Phys. **79**, 2658 (1996).

[27] A. Reittinger, J. Stimmer and G. Abstreiter, Appl. Phys. Lett. **70**, 2431 (1997).

[28] F. Priolo, G. Franzò, S. Coffa and A. Carnera, Phys. Rev. B **57**, 4443 (1998).

[29] S. Coffa, G. Franzò, F. Priolo, A. Polman and R. Serna, Phys. Rev. B **49**, 16313 (1994).

[30] G. Franzò, F. Priolo, S. Coffa, A. Polman and A. Carnera, Appl. Phys. Lett. **64**, 2235 (1994).

[31] G. Davies, Phys. Rep. **176**, 88 (1989).

[32] S. G. Cloutier, P. A. Kossyrev and J. Xu, Nature Mat. **4**, 887 (2005).

[33] M. O. Watanabe, M. Taguchi, K. Kanzaki and Y. Zohta, Jap. J. Appl. Phys. **22**, 281 (1983).

[34] J. M. Hwang, D. K. Schroder and W. J. Biter, J. Appl. Phys. **57**, 5275 (1985).

[35] L. T. Canham, M. R. Dyball, W. Y. Leong, M. R. Houlton, A. G. Cullis and P. W. Smith, Mat. Sci. Eng. B **4**, 41 (1989).

[36] E. M. Purcell, Phys. Rev. **69**, 681 (1946).

[37] R. Lo Savio, S. L. Portalupi, D. Gerace, A. Shakoor, T. F. Krauss, L. O'Faolain, L. C. Andreani and M. Galli, Appl. Phys. Lett. **98**, 201106 (2011).

[38] K. V. Srikrishnan, U.S. Patent 5882987, 16/03/1999.

[39] L. O'Faolain, X. Yuan, D. McIntyre, S. Thoms, H. Chong, R. M. De La Rue, T. F. Krauss, Electron. Lett. **42**, 1454 (2006).

[40] M. Galli, S. Portalupi, M. Belotti, L. C. Andreani, L. O'Faolain, and T. F. Krauss, Appl. Phys. Lett. **94**, 071101 (2009).

[41] W. M. N. Kessels, R. J. Severens, M. C. M van de Sanden, D. C. Schram, J. Non-Crys. Sol. **227-230**, 133 (1998).

[42] B. L. Sopori, K. M. Jones, X. J. Deng, R. Matson, M. Al-Jassim, S. Tsuo, A. Doolittle and A. Rohatgi, Proc. 22nd IEEE Photovoltaic Specialists Conf., Las Vegas, NV, 833 (1991).

[43] T. Tanabe, K. Nishiguchi, E. Kuramochi and M. Notomi, Opt. Expr. **17**, 22505 (2009).

[44] H. Park. S. Kim, S. Kwon, Y. Ju, J. Yand, J. Baek, S. Kim and Y. Lee, Science **305**, 1444 (2004).

[45] A. Berrier, M. Mulot, G. Malm, M. Östling and S. Anand, J. Appl. Phys. **101**, 123101 (2007).

[46] B. Ellis, T. Sarmiento, M. Mayer, B. Zhang, J. Harris, E. Haller and J. Vuckovic, Appl. Phys. Lett. **96**, 181103 (2010).

[47] F. Priolo, G. Mannino, M. Miccichè, V. Privitera, E. Napolitani and A. Carnera, Appl. Phys. Lett. **72**, 3011 (1998).

[48] P. Cardile, F. Franzò, R. Lo Savio, M. Galli, T. F. Krauss, F. Priolo and L. O'Faolain, Appl. Phys. Lett. **98**, 203506 (2011).

[49] S. M. Sze and K. N. Ng, *Physics of semiconductor devices*, John Wiley & Sons, New York, 2007.

[50] F. Y. Gardes, A. Brimont, P. Sanchis, G. Rasigade, D. Marris-Morini, L. O'Faolain, F. Dong, J. M. Fedeli, P. Dumon, L. Vivien, T. F. Krauss, G. T. Reed and J. Martí, Opt. Expr. **17**, 21986 (2009).

[51] Y. Akahane, T. Asano, B.-S. Song and S. Noda, Nature **425**, 944 (2003).

[52] L. C. Andreani and D. Gerace, Phys. Rev. B **73**, 235114 (2006).

[53] B. Ellis, M. A. Mayer, G. Shambat, T. Sarmiento, J. Harris, E. E. Haller and J. Vuckovic, Nature Phot. **5**, 297 (2011).

4. Light amplification in Er-based materials

Optical fibers represent the symbol of the new incredible era of long-haul, cheap and stable communications. From a corner of the world to another one, today it is possible to talk, send images, share videos and so on, thanks to these cylindrical optical signal carriers, in which information can travel at the light speed, suffering very low losses. This is possible thanks to the amplification of signals: by inserting Erbium in silica optical fibers, its radiative transition at 1.54 μm is exploited to efficiently amplify light signals.

Beyond the relentless success regarding the long-range telecommunications, the limitations of microelectronics, due to the interconnection bottleneck, has led to a development of waveguides and amplifiers, working with the same physical principles of the optical fibers in a micrometric world, in order to replace electrical signals with optical ones .

Besides the waveguides and the passive photonic devices, people start to do strong efforts in order to find Si-compatible materials in which Er could be inserted for realizing planar amplifiers. However, this is not an easy task, since the host material must be fully compatible with the standard Silicon processes, it should be transparent to the pump and the signal wavelengths and it should be able to dissolve many Er ions. Unfortunately when Er concentration is too high (usually at about 10^{20} *at/cm*^{3}*) some detrimental effects strongly limit the optical efficiency of the system, such as clustering and Er-Er interactions.*

Anyway, optical amplifiers were realized on SiO_2*,* Al_2O_3 *or by using Silicon nanostructures: in all these cases, since Er is just a dopant, a reasonable gain was observed only in structures hundreds or even thousands of μm long. This is too much for being integrated on a Silicon chip.*

An interesting strategy regards the use of Er-based materials, in which it is possible to tune Erbium concentration from the typical doping regime of 10^{20} *at/cm*^{3} *to the constitutive element regime of* 10^{22} *at/cm*^{3}*. Y-Er mixed oxide (*$Y_{2-x}Er_xO_3$*), for instance, was demonstrated to be a promising material for applications in microphotonics.*

A more intriguing compounds family is the silicates one. In fact it was demonstrated that Erbium disilicate is a stable compound, characterized by a strong photoluminescence intensity, with 10^{22} *Er ions in an optically active state, thus being really promising for reducing the size of planar amplifiers. In that case, however, the ineluctable Er-Er interactions make the Er de-excitation too fast.*

It is then interesting to study Er in Y-Er mixed disilicate ($Y_{2-x}Er_xSi_2O_7$*) in which Erbium is diluted continuously in order to perfectly control the Er-Er interactions, being* Y^{3+} *an optically inert rare earth ion. Additionally it can be useful to replace* Y^{3+} *with* Yb^{3+}*, being this rare earth a very efficient sensitizer for Erbium.*

4.1 Optical fibers technology

Since ancient times the way to communicate has been one of the most important problems of the human society. The issue of communicating includes how to create a signal carrying information, how to send it and how to detect and translate it. In the 19th century the first communication device was able to answer to all these requests: it was the telegraph, an object through which electric signals were sent along large distances. The electric signal, made of short and long dots and pauses, was read and interpreted by using the Morse code.

The next step in the communication technology was the invention of the telephone, made by the Italian Antonio Meucci, and the wireless telegraph, that allowed to send information through radio waves. For about 100 years, up to the 70s of the last century, almost all the long-range communications were based either on the electrical signals travelling in the electric wires or on the microwaves propagating in the free space. However, both these two important systems have significant limitations: the former needs a high number of repeaters, due to the high losses of the electric wires, while the latter is limited by interference phenomena.

Figure 4.1: Submarine optical fibers network, linking efficiently all the continents [1].

The solutions to these problems came out in 1970, when lasers, semiconductor-based detectors and optical fibers started to be used by the community. In fact, these are the basic components constituting an optical network. Lasers are the optical sources, emitting spatially and temporally coherent optical signals; fibers are the medium through which an optical signal can travels for very long distances; detectors receive and translate an optical signal into an electrical one, which can be then processed. That year can clearly be considered the starting point of a new era for communication technology, because since then electrical signals were gradually and completely supplanted by optical ones.

There are actually many advantages in using optical networks, instead of the previous existing ones: a higher data speed transmission, lower power dispersion and signal losses, and the possibility to send much more data flows. Therefore optical fibers were chosen by the global society to have fast connections among all the continents, as shown in the picture in fig. 4.1. This explains why today it is possible to easily communicate, to buy, sell and lend something, to share videos among some friends by using the many existing social networks, which actually link people from one side to the other in the world, simply by using a personal computer or a smart phone, connected with the World Wide Web. Actually nowadays communications in real time can be considered without doubts the key feature of our society.

Optical fibers are the main responsible of the fast development we assisted in the very last decades, and therefore Charles K. Kao, the first one who understood the potentials of these fibers, obtained the Nobel Prize in Physics in 2009.

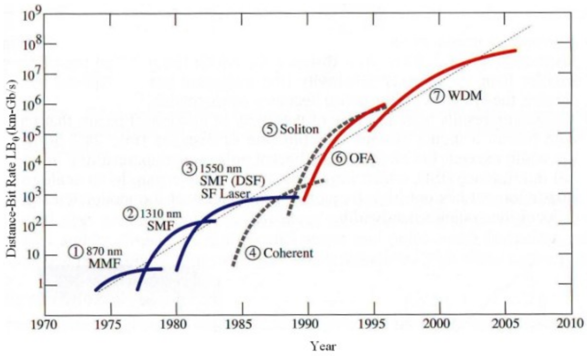

Figure 4.2: Moore's Law for optical communications: exponential increase of the figure of merit LB_0 as a function of the years since 1970 [1].

An optical fiber is a silica-based waveguide characterized by a cylindrical geometry: the inner part is the core, which is surrounded by a cylindrical cladding. The cladding has a refractive index (n_2), which is lower than that of the core (n_1). The difference in the optical density of these media is the responsible in keeping the light guided into the core. Basically, in fact, a light signal can be guided without losses into the core if its striking angle at the interface is below a critical angle $\theta_c = \arcsin(n_1^2 - n_2^2)$: this phenomenon is well known as total internal reflection [2].

With time, optical fibers were characterized by an incredible development. The world assisted to a rapid growth of their most important figure of merit, that is the product LB_0, where L is the mean distance between two repeaters and B_0 is the bit rate, i.e. the number of bits per second that can be sent through the network. At the beginning of the last century, the telephone was able to send 1 bit×km/s. Just seventy years later, the first optical fiber improved that number by nine orders of magnitude, allowing to get 1 Gbit×km/s. In the last forty years the performances of the optical fiber network increased by several orders of magnitude, following an exponential trend against time, as shown in fig. 4.2. This relentless trend is known as the Optical Moore's Law, because of the similarity of this trend with the most famous one, involving the miniaturization of the transistors [3].

The worst problem of the optical fibers network is the loss factor. This physical parameter is measured in dB/km and indicates how much the intensity of a light signal is reduced by travelling through an optical fiber. The loss factor is strongly dependent on the material and on the wavelength of the light signal. One of the most used materials is Silicon oxide, and the loss factor has a trend as a function of the wavelength that is reported in fig. 4.3 [4]. The shape is the envelope of the absorption and of the Rayleigh scattering, since these are the two main physical mechanisms causing losses.

It is possible to see that there are three main windows, at about 0.9 μm, 1.3 μm and 1.55 μm. The last one is the most important and also the most used, corresponding to just 0.2 dB/km. In any case, after a certain distance, because of this loss it is necessary to regenerate the signal, either electrically or optically.

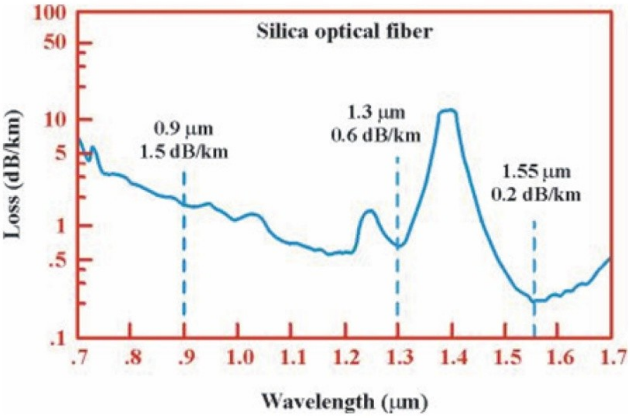

Figure 4.3: Loss factor for silica optical fibers as a function of the wavelength of the light signal [4].

The window at 1.55 µm is the most used because this wavelength corresponds exactly to the radiative transition between the metastable level $^4I_{13/2}$ and the ground state $^4I_{15/2}$ of Erbium. This is the reason why this rare earth is the most common active element present in optical fibers. In particular the introduction of Erbium allowed the realization of optical fiber amplifiers, denoted by OFA in fig. 4.2, known also as EDFA (Erbium Doped Fiber Amplifiers). This is clearly the most significant improvement, since these amplifiers increased the capability to carry signals at longer and longer distances [2, 5].

In an optical amplifier the incoming light signal is increased by several orders of magnitude simply travelling across a portion of the fiber, that is the amplifying medium. As a consequence, the figure of merit LB_0 increases as well and it can reach 1000 Tbit×km/s. This very high number is symbolic, since it represents easily the relentless request of the data transfer speed, required by the internet users.

Fig. 4.4 reports a gain characteristic of an EDFA as a function of the fiber length for different pump powers at 1.48 µm. Note that the optimum length for maximum gain depends on the pump power: by increasing the pump power, the optimum length as well as the maximum gain increases [6]. Since for long-haul communication systems the total length is not a critical parameter, Er concentration in fiber amplifiers is usually very low, only a few ppm. Therefore the Er-doped regions are very long, of the order of several tens of meters.

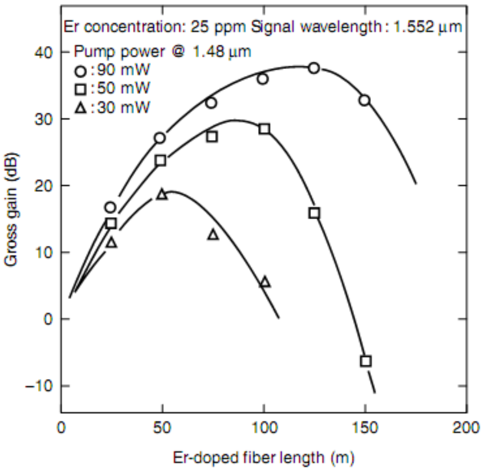

Figure 4.4: Signal gain characteristic as a function of the EDFA length [6].

Although amplifiers play a crucial role in boosting the strength of a signal, they also amplify the noise, present at the input, thus adding noise at the output. Therefore, after an amplifier usually the Signal-to-Noise Ratio (SNR) is lower or at best is the same than SNR at the amplifier input. An ideal amplifier does not produce any noise in excess (i.e. there is a 0 dB loss through it). Tong et al. [7] recently demonstrated that it is possible to achieve almost perfect amplification, with a noise figure of just 1.1 dB, providing a gain of 26.5 dB, being useful for practical applications. Their amplifier is a phase-sensitive amplifier, which exploits phase correlations, in order to amplify the signal and at the same time attenuate the noise. This is considered the next step in the development of optical fiber amplifiers [8], although future work is required in order to properly deploy this mechanism in the optical communication system.

4.2 Planar Si-based waveguides and amplifiers

Beyond the enormous success of optical fibers in long-haul communications, the 20th century has seen the fast development of the Silicon based microelectronics. However, as it was pointed out in the introductory Chapter 1, the progressive miniaturization in microelectronics has important limitations, due essentially to the losses, the signal cross-talks and the electromagnetic interferences. These detrimental effects are ineluctable, since they come from the complexity of the electronic network, with a very high number of metallic microwires. Therefore, in order to improve the performances of the microprocessors, the substitution of the electronic components with optical ones is necessary [9].

The micrometric equivalent of an optical fiber is the waveguide. The technology for the fabrication of passive devices, like waveguides, in Silicon is nowadays well developed. In particular, as in optical fibers, the physical mechanism that allows the light trapping inside the core (with a higher refractive index with respect to the surrounding cladding) of a micrometric waveguide is the total internal reflection. The very big difference is the size: these micrometric waveguides are usually realized by deposition techniques like sputtering or by ion implantation, and different lithographic steps, in order to properly design the structures.

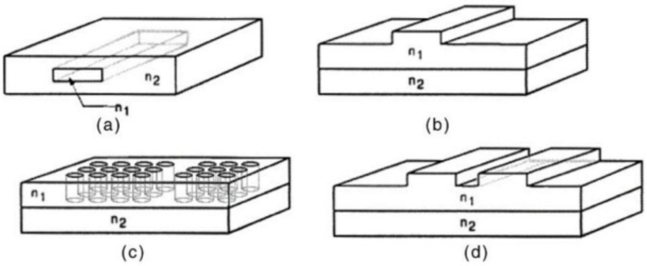

Figure 4.5: Different schemes of Silicon-based waveguides: (a) channel, (b) ridge, (c) photonic crystals-based and (d) slot waveguides [10].

The light confinement in these micrometric structures is provided by a high refractive index contrast, which forces the light to travel in very narrow regions. Particularly the most common material is SOI: in fact, the presence of a thin Silicon layer (n_{Si} = 3.45) onto a thick SiO_2 layer (n_{SiO2} = 1.5) is already helpful for the overall index contrast.

In the micrometric world it is very important to perfectly control the scattering. Scattering of light is actually the principal cause of optical losses in the waveguide. The roughness of the walls is usually the main source of scattering, being characterized by local change of the refractive index or by impurity particles. By smoothing perfectly the sidewalls of SOI waveguides, optical losses as low as 0.8 dB/cm were demonstrated [11].

Fig. 4.5 reports different geometries used to realize Si-compatible waveguides: type (a) is the channel waveguide, in which the core is completely surrounded by the cladding, exactly in the same geometry of optical fibers; type (b) is the ridge waveguide, in which the guiding layer is a strip of a material with a refractive index higher than the substrate and of the air on top. These first two types are the most classical geometries of waveguides. In the last decades, however, other photonic structures were designed in order to have a light confinement in a different way. Type (c) is the photonic crystals-based waveguide, in which the region without the holes is a defect line in the artificial crystal, in which light can propagate through. In this case, light is forced by the Maxwell's Equations to stay in the waveguide. The last type (d) is the slot waveguide: the structure has a low index sub-micrometric slot of air or SiO_2, with two side strips of Silicon. Due to the high index contrast, there is a strong enhancement of the electromagnetic field inside the slot [12], and this let the light signal propagate efficiently in this slot, that can be as small as 50 nm in width [13]. Efficient light confinement and enhanced light emission at 1.54 μm was recently demonstrated in a structure like that, where the slot was a 20 nm thick layer of SiO_2 containing Erbium and Silicon nanocrystals [14].

However, waveguides are passive devices, while it is also important to have on Silicon the equivalent of optical fiber amplifiers. Recently many solutions were proposed for the realization of Si-compatible planar amplifiers, such as Silicon nanocrystals [15] and Raman-based stimulated emission [16, 17]. By following exactly the same principle of Erbium-doped fiber amplifiers, another approach involves the introduction of Erbium as a dopant into a Si-compatible solid host [18].

4.3 Er-doping for planar amplifiers

The introduction of Erbium as an impurity element for the realization of planar optical amplifiers is widely used. In fact Erbium is already used for realizing EDFA or even for solid state lasers (YAG:Er), since the atomic-like 1.54 μm emission from Er is exploited.

In order to fabricate the equivalent of EDFA in a micrometric scale, in a waveguide-like geometry, Erbium is incorporated into a Silicon compatible solid host.

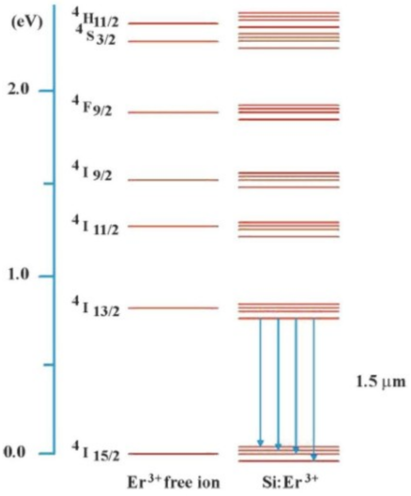

Figure 4.6: Atomic levels for Er^{3+} as a free ion (left) and as a dopant inside a solid host like Silicon (right). In this latter case the splitting due to Stark effect occurs and makes possible the forbidden transitions.

Erbium is a chemical element belonging to the rare earth family, with atomic number Z = 68 and [Xe]-$4f^{11}5d^{1}6s^{2}$ as electronic configuration. When this atom is inserted in a solid host, it loses its outer electrons, remaining with an electronic configuration [Xe]-$4f^{11}$. Like other lanthanides, therefore, Er assumes the oxidation state 3+. However the electrons in the 4f shell are actually shielded by the external closed $5s^2$ and $5p^6$ shells. A scheme of the energy levels of the free Er^{3+} ion is reported in fig. 4.6 (left). Note that the selection rules forbid the electric dipole transitions within the 4f shell, because $\Delta L = 0$. When Er^{3+} ions are inserted into a solid host, like Silicon for instance, they are impurity atoms interacting with the crystalline field of the host (see fig. 4.6 on the right). This crystalline field partially breaks the m_J degeneracy destroying the spherical symmetry of the Er^{3+} ion, splits the atomic levels in multiplets and mixes states of different parity. This is known as Stark effect and it allows some transitions that were actually forbidden in the case of free Er^{3+} ions. The one between the $^4I_{13/2}$ and the $^4I_{15/2}$ manifolds allows the radiative emission of photons at 1.54 μm, which is very important for applications in photonics, as already pointed out in section 4.1. This wavelength does not depend on the solid host, since the outer electrons of Er realize an electronic shield which in some way protects the transitions within the 4f shell.

In a typical optical amplifier, Er^{3+} is inserted in the core of the guiding layer and it is excited optically, from the top for instance, at 980 nm, a wavelength resonant with the jump $^4I_{15/2} \rightarrow {}^4I_{11/2}$. When Er^{3+} is excited to this level, it usually quickly de-excites to the metastable $^4I_{13/2}$ level. In case of high pumping power, it is possible to have a population inversion between the first excited state and the ground state. Therefore, if there is an incoming photon at 1.54 μm, travelling in the waveguide, it can be amplified by stimulated emission [18, 19].

These kinds of amplifiers are realized usually with insulating hosts: in these materials, in fact, Er can be excited by direct photon absorption. This means that the incoming photons must have well defined energies, perfectly matching the jumps between Er levels, in order to be absorbed. The typical absorption cross sections are very weak, being of the order of $\sim 10^{-21}$-10^{-20} cm^2 [5]. However, since in a Silicon chip an Er-doped planar amplifier is confined in a small piece of matter, its length should be ~1-10 μm. This means that, in order to have a significant gain (at least 1 dB/cm), a large number of Er^{3+} ions are required ($\sim 10^{20}$-10^{21} ions per cm^3). On the other hand, too many Er^{3+} ions carry a certain amount of issues: the higher is the Er concentration, in fact, the stronger are detrimental effects for amplification, as it will be discussed in the next subsection.

4.3.1 Limitations of Erbium doping

The total concentration of Er^{3+} ions in an optically active state inside the solid host for the planar amplifier is the most important physical parameter, since it determines the length of the device. Unfortunately, it is not possible to push this number, because two important phenomena take place when Er concentration is too high: clustering and ion-ion interactions.

When the Erbium content overcomes a critical value, which of course depends on the solid host, Er^{3+} ions start to segregate and precipitate, thus leading to the formation of clusters.

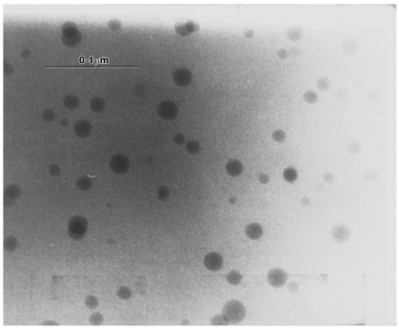

Figure 4.7: Cross-sectional TEM image showing the formation of Erbium clusters (black spots), after Er implantation in a thermally grown SiO_2 film, annealed at 1200 °C for 1h [20].

This phenomenon was clearly observed in Er-implanted thermally grown SiO_2 [20], as reported in the cross sectional TEM in fig. 4.7: Erbium clusters (black spots) were formed after an ion implantation of 5×10^{15} Er/cm^2 and a thermal treatment at 1200 °C for 1 h. The same authors demonstrated that the occurrence of clustering is detrimental for the optical emission of Er^{3+}. In order to show this, the photoluminescence (PL) intensity and Er^{3+} lifetime at 1.54 μm are reported in fig. 4.8 as a function of the annealing temperature.

The PL intensity (a) increases by raising the temperature up to 700 °C; after that, the PL intensity remains constant up to 1000 °C. Finally, for higher temperatures the PL intensity drops quickly down, due to the formation of clusters, as observed in fig. 4.8. The lifetime at 1.54 μm (b) is reported for the same range of temperatures: this is the characteristic Erbium de-excitation time from the $^4I_{13/2}$ level. This measurement is very important because it contains information about radiative and non-radiative mechanisms. Also the lifetime increases up to 700 °C, and then it remains constant.

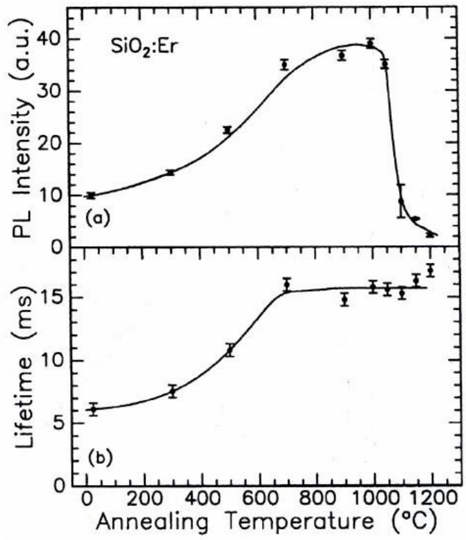

Figure 4.8: PL intensity and lifetime at 1.54 μm as a function of the annealing temperature for Er-implanted thermally grown SiO$_2$ [20].

It is well known that the PL intensity is proportional to the lifetime, according to the relation:

$$I_{PL} \propto \frac{\tau}{\tau_{rad}}, \tag{4.1}$$

where σ is the direct absorption cross section of Er^{3+}, $[Er_{att}]$ is the number of Er^{3+} ions in the film which are in an optically active state, τ_{rad} the radiative lifetime at 1.54 μm and τ the overall lifetime at the same wavelength, including both the radiative and the non-radiative decay paths. The reciprocals of the lifetimes are the decay rates: the ratio between the radiative decay rate ($1/\tau_{rad}$) and the total one ($1/\tau$) represents therefore the probability to obtain the emission of a photon with respect to all the decay processes, both radiative and non-radiative.

Therefore, by considering equation (4.1), up to 700 °C, we can say that the increase of PL intensity is due to an increase of the lifetime, i.e. to a higher probability to have a photon emitted. In fact, after the annealing, some defects in the matrix were removed, thus reducing the number of non-radiative decay paths for Erbium. Between 700 °C and 1000 °C there is no a sensible improvement of the optical emission. However at higher temperatures the PL intensity drops down since there are much less optically active Er^{3+} ions (many of them precipitated in clusters), but the remaining Er^{3+} ions have the same lifetime.

The other issue for optical amplification is the occurrence of Er-Er interactions induced phenomena, particularly concentration quenching and cooperative upconversion.

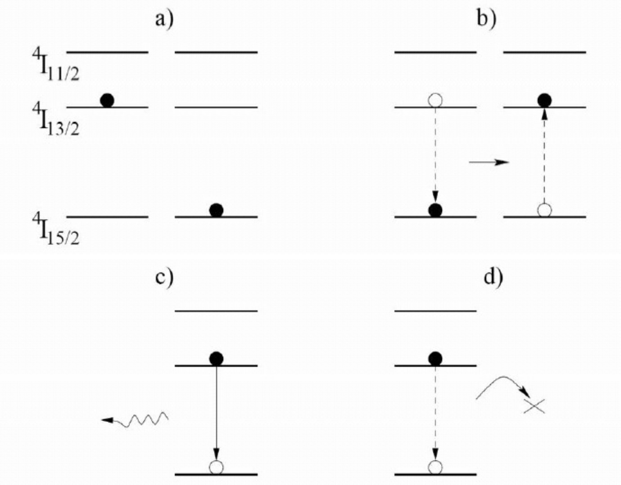

Figure 4.9: Scheme of concentration quenching mechanism: an excited Er^{3+} ion (a) may transfer its energy to a close Er^{3+} ion in the ground state (b). Energy can travel until there is a photon emission at 1.54 μm (c) or it is lost due to a quenching center (d).

Concentration quenching was observed in many rare earth-doped materials. For Erbium in silica or silica-based glasses it occurs for more than 1×10^{20} Er/cm^3, and it strongly reduces Erbium lifetime, by increasing the Er concentration. The mechanism is depicted in fig. 4.9. When an Er^{3+} ion is in the first excited state and it is very close to another Er^{3+} ion in the ground state (a), a dipole-dipole interaction may occur, through which the excitation actually migrates from the first ion to the second one (b). Also this latter ion may transfer its energy to a third ion in the ground state, and so on. This energy migration will stop in two different ways: at some point in fact the excitation is lost either by a radiative transition, i.e. by the emission of a photon at 1.54 μm, or by transferring the energy to a quenching center, i.e. a defect or a center that absorb the energy without emitting any light out. Therefore, when Er concentration is increased, it is more probable that energy travels along the sample, being resonantly transferred from Er to Er, and it is more probable that a quenching center is reached; this is true even if the quenching center is far away from the initial Er^{3+} ion that was excited. This automatically means that the non-radiative processes become stronger by increasing Erbium and the overall lifetime decreases.

It is well accepted in literature that concentration quenching is modeled by expressing the Erbium decay rate W_{Er} in the following way [20-22]:

$$W_{Er} = \quad + \quad N_{Er} N_Q, \tag{4.2}$$

where W_0 is the decay rate in absence of concentration quenching, i.e. in the limit of very low concentrations, $C_{Er\text{-}Er}$ is a coupling constant which represents the interaction between two Er^{3+} ions, N_{Er} is the Erbium concentration in the film and finally N_Q is the density of quenching centers. This relation is valid also for other rare earth ions, but in the case of Erbium the responsible of the quenching are usually the –OH groups [20], since these radicals are characterized by a double harmonic molecular vibration of 0.8 eV, exactly resonant with the Erbium transition ${}^4I_{13/2} \rightarrow {}^4I_{15/2}$. Therefore if there is a coupling between an Er^{3+} ion and these radicals, by concentration quenching, the energy can be lost with this non-radiative channel.

The immediate detrimental consequence for an efficient Er-based planar amplifier is that both a high number of emitting centers and a long lifetime are required in order to achieve the population inversion, necessary for the stimulated emission. Concentration quenching establishes a maximum Er concentration, above which the lifetime starts to decrease (and the decay rate starts to increase).

Another phenomenon detrimental for the achievement of an efficient optical amplification is cooperative upconversion. This phenomenon is strongly dependent on the pumping flux as well as the Erbium content [23].

In fact when Erbium is excited by a high photon flux, it is probable that two close Er^{3+} ions are both in the $^4I_{13/2}$ level. If this is the case, these two Er^{3+} ions can interact via dipole-dipole interaction: one of the two ions gives its energy to the second one, collapsing to the ground state. The acceptor, on the contrary, is promoted to the $^4I_{9/2}$ level, but it quickly and non-radiatively de-excites from this level to the sub-lying ones, and in particular it comes back to the initial state, the $^4I_{13/2}$ level. In the end, the net result is that an excitation is definitively lost, since two incoming photons generate only one excited Er^{3+} ion. The mechanism is schematically depicted in fig. 4.10 and its efficiency depends on the solid host where Erbium is inserted.

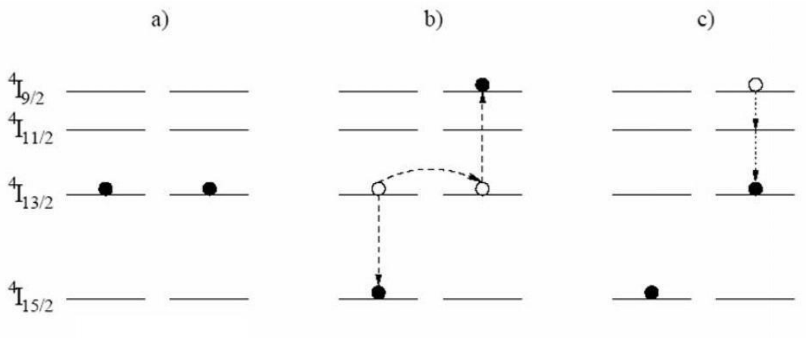

Figure 4.10: Upconversion mechanism: two nearby Er^{3+} ions in the first excited state (a) can interact in such a way that one is promoted to the $^4I_{9/2}$ level and the second goes down to the ground state (b). Then just one photon can be emitted at 1.54 μm at expenses of two excited ions. [20].

The strength of upconversion is described by a coefficient C_{up}, a parameter that is introduced in the Erbium rate equations describing the first excited state. Upconversion has the effect of reducing the number of ions in the first excited state and it is a quadratic term, since it occurs with two excited ions. Therefore the dynamics of the first excited state is ruled by the following equation:

$$\frac{dN_1}{dt} = \qquad - \frac{N}{\tau} - \qquad \tag{4.3}$$

where N_1 is the population of the first excited state ($^4I_{13/2}$), N_0 is the population of the ground state ($^4I_{15/2}$), σ is the absorption cross section, φ is the pumping flux and τ is the Erbium lifetime. The first excited level is in fact populated by the excitation flux, and it is depopulated by the normal decay with a lifetime τ and by upconversion. The product ($C_{up} \cdot N_1$) is a rate: it represents the probability per time unit that upconversion occurs. This is the reason why C_{up} should be as low as possible, in order to have a good amplifier. Additionally this coefficient is proportional to a general coupling probability between two Er^{3+} ions, which can be expressed by the following relation, according to the Dexter theory [24]:

$$C_{da} = \frac{3Q}{64\pi n \cdot \tau_d} \int \quad , \qquad (4.3)$$

where Q_a is the integral absorption cross section of the acceptor, n is the refractive index of the film, Ẽ is the average energy value of the transition between the involved Stark manifolds, τ_d is the donor radiative lifetime, and the last integral is the superimposition integral between the emission spectrum of the donor and the absorption spectrum of the acceptor. This last term is crucial, since if there is no superimposition in the levels' coupling, then there is not any Er-Er interaction.

Upconversion may also involve different Er^{3+} levels, for example $^4I_{11/2}$ and $^4F_{7/2}$: in this case a photon at 560 nm or at 980 nm is emitted at expenses of two excitations at 980 nm. However the occurrence of this phenomenon is less probable than that just analyzed. In fact the population in the $^4I_{11/2}$ level is much less than that in the $^4I_{13/2}$ one, and therefore this phenomenon is called second-order upconversion.

4.3.2 Er-doped Silicon-compatible materials

The occurrence of all the limiting processes already described was deeply investigated in many Silicon-compatible hosts for Erbium. These hosts must be transparent to the wavelength used to excite Erbium ions and to the signal wavelength; moreover the hosts should be able to dissolve Er^{3+} in an optically active state and a waveguide must be realized with a technology compatible with standard Silicon processing.

Silicon oxide was one of the first materials studied as hosts for Er-based planar amplifiers, since it is a well-established material used in optical fibers and in microelectronics.

When Erbium is inserted in this material, it becomes optically active when it is surrounded by six Oxygen atoms, forming an ErO_6 complex, which is fundamental for the optical emission: in fact in presence of Er-Er and Er-Si bonds, the rare earth does not have any luminescence properties [18].

In the low concentration regime, Er^{3+} lifetime in this material is about 15 ms, a very long characteristic time, which is very interesting for optical amplification. However the main limitation in this system is represented by the solid solubility of Er^{3+}, since this is limited to about 2×10^{20} at/cm^3. When this concentration limit is exceeded, clustering occurs, representing a detrimental effect for Er^{3+} luminescence. This limitation can be increased by more than one order of magnitude, by using soda-lime silicate or other glasses, but these materials are not very Si-compatible, being synthesized by melting the constituent oxides at too high temperatures and – after the synthesis – being characterized by a detrimental liquid-glass transition temperature too low (usually less than 600 °C).

In 1993 Hattori *et al.* [25] realized the first Er:SiO_2 planar amplifier, by using an S-shape geometry 8 μm wide, 7 μm thick and 23 cm long. Such a huge length was required, since the Er concentration was very low (4×10^{19} at/cm^3) in order to have the reasonable gain of 7.4 dB, by pumping at 980 nm with a 68 mW power. The length is however too much in order to integrate such a waveguide amplifier in a Silicon chip.

Upconversion was of course studied for Erbium in silica and C_{up} was estimated to be 7×10^{-17} cm^3/s [18]. Yan *et al.* [26] demonstrated that by doping SiO_2 with P_2O_5 a better distribution of the Er^{3+} ions is achieved and this trick can be used to reduce Er-Er interactions.

Another common material that was recently studied for waveguides and amplifiers is Al_2O_3: waveguides with very low losses (about 0.3 dB/km) were demonstrated [27]; moreover Er^{3+} has been successfully introduced as a dopant in Al_2O_3, thanks to its higher solubility (at least 6×10^{20} at/cm^3 [28]) with respect to SiO_2. This is due to the fact that it is easy to substitute Al^{3+} ions with Er^{3+} ones, thanks to the match of the ion valence. Additionally Van den Hoven and coworkers demonstrated that this material is characterized by a very low upconversion coefficient ($2\text{-}4\times10^{-18}$ cm^3/s [29]), thus meaning that when Er^{3+} is excited at high pumping fluxes the detrimental effects of upconversion are shifted at higher fluxes with respect to silica. More recently Er-implanted ridge Al_2O_3 waveguides were realized with spiral geometry, confining a photolithography designed 3 cm long waveguide into a small area of 1 mm^2 and achieving a gain of about 2.5 dB [30].

One of the most intriguing materials in which Er^{3+} was successfully introduced is SiO_2 with a Si excess that leads to the formation of Silicon nanocrystals (Si-nc) embedded in the silica host. A very efficient sensitization of Er^{3+} by the nanostructures was demonstrated [31], with an excitation cross section four orders of magnitude higher than that of Erbium in silica; moreover Er is excited also non-resonantly. For this system it was calculated that under particular conditions it is possible to have a population inversion for Er^{3+} [32] and it was demonstrated an internal gain of 7 dB/cm in ridge waveguides [33].

Another common solution for effectively excite Erbium ions, by increasing the excitation cross section, is to co-dope the host with Ytterbium as well. This technique was successfully used in fiber amplifiers, fiber lasers and microlasers [34-36]. The reason lying beyond the co-doping is the perfect energy matching between the $^4I_{11/2}$ level of Er^{3+} and the $^2F_{5/2}$ level of Yb^{3+}, as reported in fig. 4.11. By exciting an Yb^{3+} ion at 980 nm, due to this matching, it can easily transfer this energy to a nearby Er^{3+} ion.

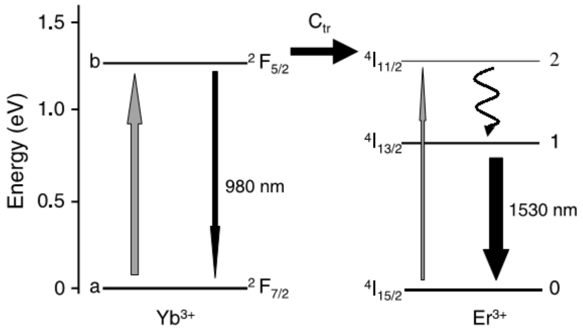

Figure 4.11: Energy levels of Yb^{3+} and Er^{3+}. An Yb^{3+} ion that is excited from the ground state to the $^2F_{5/2}$ level can transfer its energy to a nearby Er^{3+} ion, which is promoted to the $^4I_{11/2}$ level, and then quickly decays to the $^4I_{13/2}$ level [37].

Since Yb^{3+} has an absorption cross section of about 10^{-20} cm^2 at 980 nm [37], i.e. one order of magnitude higher than Er^{3+} [5], and since the energy transfer between the two rare earths has been widely demonstrated in literature in many solid hosts, we can conclude that Er^{3+} ions can be efficiently excited through the sensitization with Yb^{3+} ions.

Though all these materials are promising and have good optical properties, a strong effort must be further done, remarkable improvements are necessary in order to achieve the realization of Si-compatible planar optical amplifier.

4.4 From dopant to constituent: how to increase Er concentration

We have seen that two of the most important issues of the materials acting as hosts for Erbium are the maximum concentration of Er^{3+} that can be inserted and a good distribution of Er^{3+} ions in the matrix, in order to reduce eventually the detrimental ion-ion interactions.

In this section we explore the possibility to have Erbium-rich materials which can be useful for optical communications in Silicon. In particular, we are talking about Er-based compounds; the concentration can be varied continuously from an Er-doped system to another system in which Er^{3+} is a constitutive element itself, thus allowing a perfect control of the ion-ion interactions, since they are strongly dependent on the mean Er-Er distance.

4.4.1 Er-Y mixed oxides

One of these materials is Erbium-Yttrium mixed oxide, $Y_{2-x}Er_xO_3$: in this case, starting from a bare Y_2O_3, it is possible to gradually introduce Erbium, for instance by contemporary sputtering an Er_2O_3 target and an Y_2O_3 one [38], thus exploring both the regime in which Er is a dopant ($\sim10^{20}$ Er/cm^3) and the new interesting regime in which Er is a constituent ($\sim10^{21}$-10^{22} Er/cm^3), reaching eventually the extreme case of Erbium oxide [39].

The possibility to overcome the solubility limitation found in other solid hosts is due to the remarkable similarities between Y^{3+} and Er^{3+} ion properties (similar ionic radius, identical cationic properties), and between the correspondent oxides, since they have the same crystalline centered cubic structure with similar lattice parameters. In fact Yttrium can be considered an added element to the lanthanides family in the periodic table, even though it is a transition metal: as far as inorganic chemistry is concerned it behaves as a rare earth, being characterized by an electronic configuration [Kr]-$4d^1 5s^2$, very similar to lanthanum [Xe]-$5d^1 6s^2$. Therefore Yttrium behaves in a compound as a rare earth, though it is optically inactive, having its 4f shell completely empty of electrons.

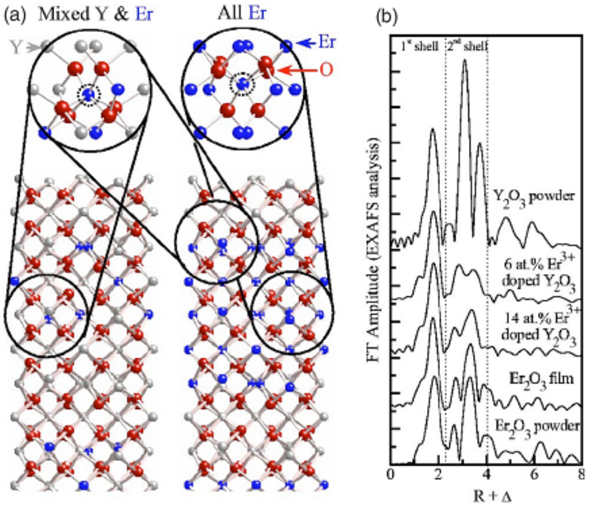

Figure 4.12: (a) Chemical situation for Er in Y_2O_3 matrix. (b) Fourier transformation of EXAFS spectra of Er-Y mixed oxide as a function of Er concentration [40].

These properties permits that Er^{3+} ions can be inserted in substitutional sites instead of Y^{3+} ions, as shown in the scheme reported in fig. 4.12 (a). Each Er^{3+} ion (blue) is surrounded by Oxygen, forming the Er-O complex necessary for its luminescence properties. The second coordination shell is full of Y^{3+} ions for low Er concentrations; as soon as the Er content increases, it starts replacing Y^{3+} ions in the second shell, thus allowing the formation of Er-O-Er bonds. Note that this behavior is well described by the Fourier transformation of the Extended X-rays Absorption Fine Structure (EXAFS) spectra in fig. 4.12 (b): the spectrum is similar to the Y_2O_3 one for low Er doping, while it becomes more and more similar to the Er_2O_3 one by increasing the Er content.

Note that in this material it is easy to see by X-Ray Diffraction (XRD) that gradual substitution of Er in the Y_2O_3 lattice, by looking at the position of the diffraction peaks. They slightly move towards larger angles by increasing Er, since the lattice parameter is shrinking accordingly, as reported in fig. 4.13 (a) and (b) respectively [38].

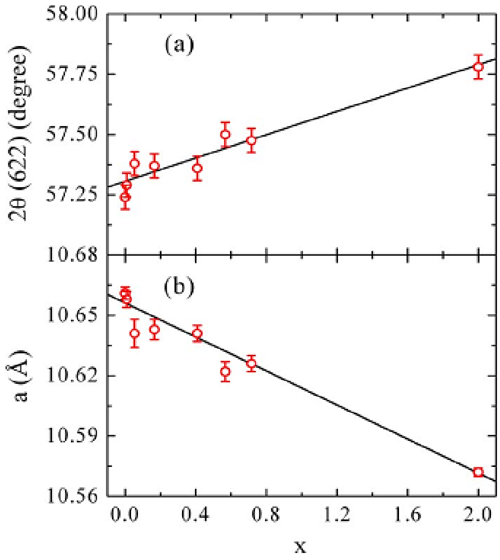

Figure 4.13: (a) Gradual increase of the position of the diffraction peaks and (b) correspondent shrinkage of the lattice parameter by increasing the Er content in $Y_{2-x}Er_xO_3$ films grown by sputtering [38].

By studying the photoluminescence properties and the excitation and de-excitation mechanisms of Er^{3+} in this compound, it was demonstrated that Er^{3+} ions are in an optical active state even without any thermal treatment. Additionally, thanks to the low phononic energy of the host, population inversion between the second and the first excited state was demonstrated in the Er-doping regime, thus being useful for optical amplification at 2.75 μm [38]. On the other hand, in the Er-compound regime, most of the population was found to be in the first excited state, being useful for efficient light emission at 1.54 μm [38].

4.4.2 Er-based silicates

An important class of compounds in which a rare earth like Erbium can be inserted as a constitutive element is the silicates family. This important family will be discussed in detail in this section.

Rare earth silicates are chemically stable compounds formed by mixing Silicon oxide and a rare earth oxide. By mixing these two oxides, different situations are possible, according to Thermodynamics: fig. 4.14 reports the phase diagram of a system including SiO_2 and Er_2O_3. For temperatures up to 1700 °C, two stoichiometric silicates are thermodynamically stable: the first one is Erbium monosilicate Er_2SiO_5, whose stoichiometry is due to a ratio $[SiO_2]/[Er_2O_3] = 1$; the second one is Erbium disilicate $Er_2Si_2O_7$, which on the contrary is characterized by a ratio $[SiO_2]/[Er_2O_3] = 2$. A third stable phase appears at higher temperatures and has an intermediate composition [41].

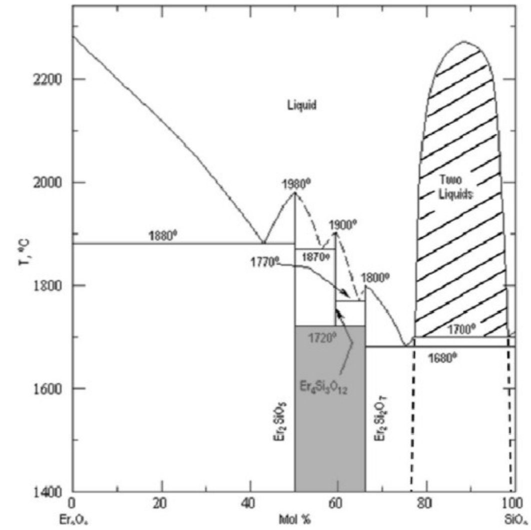

Figure 4.14: Phase diagram of SiO_2 and Er_2O_3 system; both monosilicate and disilicate are indicated in the graph [41].

Since the chemical properties are similar for all the rare earth ions, having them similar ionic radii and electro-negativities, it is not surprising that all the SiO_2+RE_2O_3 systems, where RE is a lanthanide ion or Yttrium, have the same phase diagram showing the very same stoichiometric silicates.

Beyond the stoichiometric ratios, it is well known that both monosilicate and disilicate are characterized by a complex polymorphism, crystallizing in different crystalline phases as a function of the external conditions (temperature and pressure, for instance). Generally RE monosilicates crystallize in two polymorphs [42]: the first one is formed at 1000 °C and it is called A-phase; at a temperature of about 1200 °C the transition to the second polymorph, the B-phase, occurs. On the other hand, RE disilicates are much more complex, since up to six polymorphs were found, usually named y, α, β, γ, δ and η. All these different crystalline structures contain SiO_4 tetrahedral pairs linked each other, thus forming Si_2O_7 diortho groups, characterized by a Si-O-Si bond angle, which depends on the phase [42].

The crystalline structures y-$RE_2Si_2O_7$ is formed at relatively low temperatures (1000 °C) and it is found in nature in a mineral called yttrialite. This phase was successfully synthesized for Y, Tm and Er [43], though only for the former rare earth a pure phase was obtained. This structure is monoclinic, characterized by a space group $P2_1/m$ and cell parameters (for y-$Y_2Si_2O_7$) a = 7.50 Å, b = 8.06 Å, c = 5.02 Å and β = 112.4° [44]. However, given the known similarities of Y^{3+} ions and the RE^{3+} ions, these parameters will not change too much for the other RE y-type disilicates. The unit cell contains two equally populated RE sites, as shown in fig. 4.15 (a): the polyhedra represent the diortho groups, connected with both dark and grey spheres, which indicate the two RE sites.

The α-phase is formed at higher temperatures (about 1200 °C), though it is present usually together with the y-phase. The structure of this polymorph is triclinic, characterized by a space group P-1. For α-$Y_2Si_2O_7$ the unit cell has as parameters: a = 6.59 Å, b = 6.60 Å, c = 12.25 Å and α = 94.0°, β = 89.2°, γ = 93.1 [45]. The cell parameters are a little reduced for α-$Yb_2Si_2O_7$: a = 6.53 Å, b = 6.55 Å, c = 11.89 Å and α = 85.7°, β = 91.2°, γ = 88.2 [46], since the ionic radius of Yb^{3+} is 0.86 Å, a bit smaller than that of Y^{3+} (0.89 Å). The cell is depicted in fig. 4.15 (b): it is worth noticing that there are isolated Si_3O_{10} chains, placed around some SiO_4 tetrahedra. Moreover there are four different sites for both Si and RE [44].

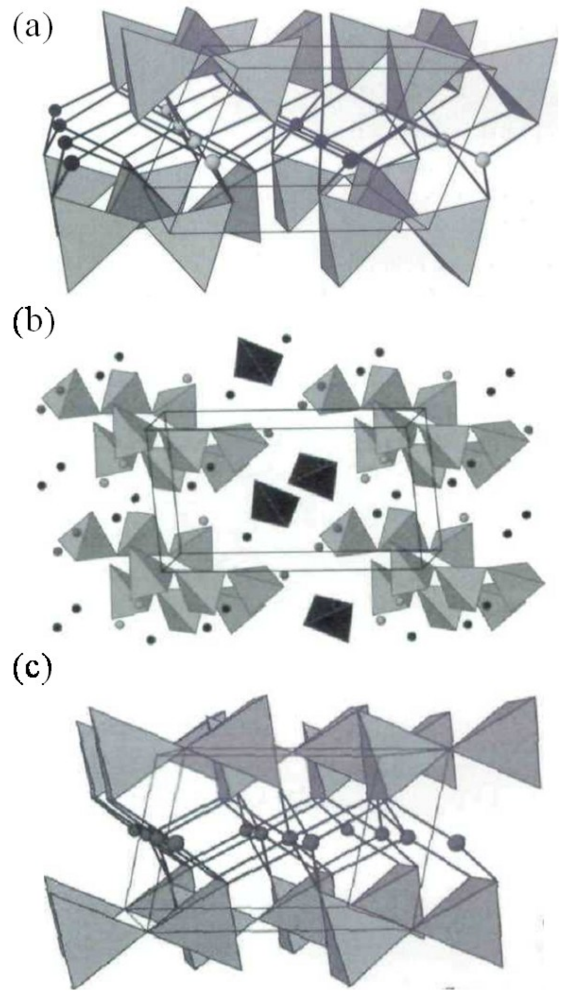

Figure 4.15: Unit cells of y-phase (a), α-phase (b) and β-phase (c) disilicate, according to ref. [44].

The β-phase is isostructural with the mineral thorveitite ($Sc_2Si_2O_7$) and it is a monoclinic structure belonging to the C2/m space group. The unit cell is depicted in fig. 4.15 (c), and it is easy to see that it is very similar to the y-one [44]. For β-$Y_2Si_2O_7$ the unit cell has as parameters: a = 6.88 Å, b = 8.97 Å, c = 4.72 Å and β = 101.7° [47]. Also for this polymorph the cell is a little shrunk for β-$Yb_2Si_2O_7$, becoming: a = 6.80 Å, b = 8.87 Å, c = 4.70 Å and β = 102.1° [48]. The β-phase is formed at even higher temperatures than α-phase and it is favored by increasing the ionic radius of the RE, as depicted in fig. 4.16: this is the diagram in which the temperature of the phase transitions are shown as a function of the ionic radius, i.e. as a function of the RE constituting the silicate [43]. The y-phase is not present, since at that time it was not still synthesized.

Note that the other polymorphs (γ and δ) are stable by increasing the temperature or the ionic radius, while η-phase appears only at very high pressures [49].

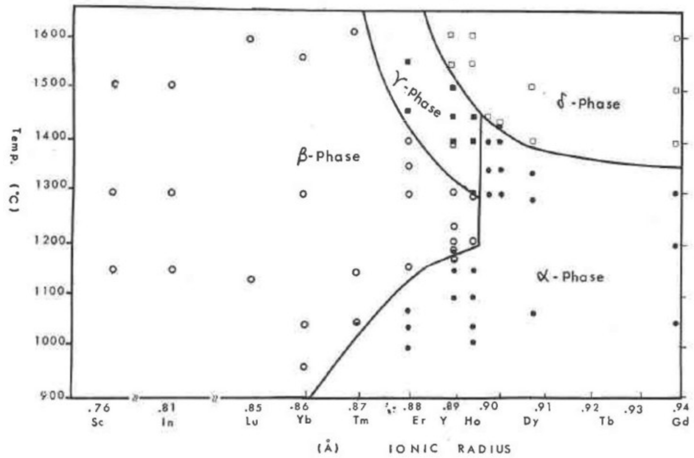

Figure 4.16: Polymorphism of all the RE disilicates: temperature of phase transitions as a function of the ionic radius, i.e. of the RE ion [43].

It is interesting to note that in the diagram Y and Er are very close. Therefore by performing a thermal treatment around 1100°C – 1200 °C, we expect that for both $Y_2Si_2O_7$ and $Er_2Si_2O_7$ α-crystalline structure is formed. On the other hand, at the same temperature, by considering for instance $Yb_2Si_2O_7$, we should find that the formation of β-phase is favored.

As already pointed out for Y-Er mixed oxide, it is possible to use rare earth silicates as hosts for Erbium: also in this case the similarities between the rare earths allow a gradual substitution of any RE^{3+} ion with Er^{3+} one, thus permitting to vary Erbium in this matrix within a two orders of magnitude concentration range, between 10^{20} to 10^{22} at/cm^3. This approach is very interesting in the case of Yttrium, which is an inert ion, permitting a perfect control of Er-Er interactions.

Another possible RE disilicate that can be exploited as host for Erbium is $Yb_2Si_2O_7$, given the known extraordinary absorption cross section and the effective energy transfer rate to Er. In a mixed Er-Yb disilicate we would vary the concentrations of both the rare earths, thus exploring many different Yb/Er ratios, in order to find the most convenient ratio for Erbium excitation. Also in this case the Er concentration (and accordingly the Yb one) can be varied between 10^{20} to 10^{22} at/cm^3. Additionally the high concentration regime for both these two rare earths has never been studied up to now in a disilicate system.

These are the reasons why we decided to study in detail the structural and the optical properties of Er-based disilicates, particularly of $Er_xY_{2-x}Si_2O_7$ and $Er_xYb_{2-x}Si_2O_7$ thin films grown on Silicon.

4.4.3 RE luminescence silicates: state-of-art

In order to understand the state-of-art regarding the possible applications of the just introduced materials in microphotonics, in this subsection we will discuss the results obtained up to now about RE luminescence in silicates.

Yttrium silicates were not deeply investigated in the past. Yttrium monosilicate (Y_2SiO_5) was studied as a phosphor when doped with Ce, Eu and Tb, thanks to the visible luminescence of these RE ions [50]. Moreover it was demonstrated laser action from Er-Yb co-doped B-Y_2SiO_5 single crystals [51].

An interesting work was done about A-$Er_xY_{2-x}SiO_5$ nanocrystals (with *x* varying between 0 and 2), obtained by spinning a solution on a dense array of Silicon nanowires and by performing a thermal treatment [52]. By exciting Er at 488 nm, a wavelength resonant with the transition $^4I_{15/2} \rightarrow {}^4F_{7/2}$, these nanoparticles show photoluminescence (PL) at 1.54 μm and at 980 nm. This last emission is due in particular to upconversion phenomena and it occurs at high pumping fluxes and for an Erbium concentration higher than 5 at.%. The recorded PL spectra are shown in fig. 4.17 for all the studied concentrations. It is remarkable that, for 1×10^{21} Er/cm^3, the upconversion coefficient C_{up} was about 2×10^{-18} cm^3/s, a value one order of magnitude lower than that obtained in silica with just 1×10^{20} Er/cm^3.

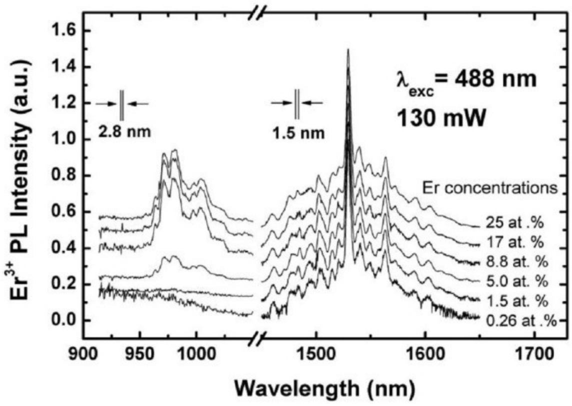

Figure 4.17: PL spectra from $Er_xY_{2-x}SiO_5$ nanoparticles as a function of the Erbium concentration. An intense signal at 980 nm appears at high Erbium contents, due to the occurrence of upconversion [52].

The same research group realized the same material in thin films grown by ion beam sputtering. They demonstrated that an annealing in O_2 at 1100 °C is necessary in order to induce the crystallization and to remove defects and quenching centers for Erbium [53].

As regards Yttrium disilicate, Eu was introduced in $Y_2Si_2O_7$ films grown by metal-organic decomposition sol-gel process, with a concentration of about 1 at.%, for application as a luminescent phosphor [54]. By exciting Eu at 248 nm, a strong luminescence in the visible is found due to the $^5D_0 \rightarrow {}^7F_J$ (with J varying between 0 and 4) radiative transitions. In particular it was demonstrated that the measured PL intensity increases as a function of the annealing temperature. For a thermal treatment at 1050 °C in N_2 the films crystallize in the α-phase, as demonstrated by X-ray diffraction (XRD) measurements. It is important to remark that Eu in α-phase showed the most intense PL signal and the longest lifetime.

One of the most intriguing silicate families is the Erbium silicates one, i.e. compounds in which the Erbium concentration is fixed to be always

~10^{22} at/cm^3. This can be considered the extreme case in which all the Y^{3+} ions in an Y silicate are replaced by Er^{3+} ones. Thin films of Er silicates were synthesized by magnetron sputtering, in which all the Er^{3+} ions were optically active [55, 56].

In both Er_2SiO_5 and $Er_2Si_2O_7$ the Er lifetime is obviously very short (a few hundreds of μs), due to the occurrence of Er-Er interactions that cannot be avoided, being the mean Er-Er distance very short. By considering equation (4.2), describing the concentration quenching phenomenon, it is clear that the only parameter that can be controlled in order to increase the lifetime is the amount of defects. The Er concentration, in fact, is fixed as well as the radiative lifetime. This is the reason why, in order to optimize the PL emission in these materials, strong thermal annealing are required.

By analyzing the stability on Silicon and the optical emission of Er in the two silicates, it was found that Er disilicate is the best one [55]. For this compound it was also demonstrated that after a thermal treatment at 1200 °C either rapid (30 s) or long (1h), either in N_2 or in O_2, there is no reactivity with the Silicon substrate [56]. However the annealing gas has an important influence on the crystallization: in the case of Nitrogen, at 1100 °C the y-phase is formed; on the other hand, Oxygen induces the formation of a mixture of α and y phases. These two phases are recognizable by XRD measurements, by looking at the diffraction peaks, but also by analyzing the photoluminescence spectroscopy, since the Er emission peak shape at 1.54 μm is strongly dependent on the crystalline environment, though the peak position is fixed, as guaranteed by the outer shielding electrons. Among the two polymorphs, it was found that after the thermal treatment, O_2 has a more relevant effect in the Er luminescence and therefore α-$Er_2Si_2O_7$ is surely the most efficient from the optical point of view.

Besides the gas, also the most efficient thermal treatment was successfully identified, by comparing the PL intensity and the lifetime measurements at 1.54 μm. A resume of the experimental data is shown in fig. 4.18 as a function of the temperature for both rapid and long annealing treatments in O_2 [56]. It is worth noticing that the best treatment is 1250 °C, 30 s. The lifetime at 1.54 μm perfectly follows the PL intensity. Since PL is proportional to τ, we can conclude that the progressive increase of PL intensity by increasing the rapid treatment temperature is due to a reduction of defects, such as Oxygen vacancies, i.e. to a reduction of the overall decay rate.

Therefore, in order to optimize the Erbium luminescence in a disilicate environment, we can conclude that we should manage to let the film crystallize in the α-polymorph, which is the most interesting from the optical point of view.

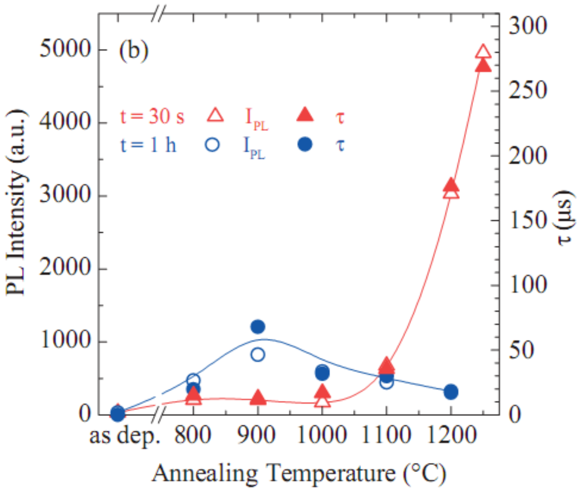

Figure 4.18: PL intensity and lifetime at 1.54 μm for $Er_2Si_2O_7$ thin films grown on Silicon, as a function of the annealing temperature in O_2 both for 30s and 1h [56].

A question arises on the possibility to insert in these silicates also Yb^{3+} ions, acting as sensitizers for Er^{3+}. The influence of Ytterbium in the Erbium luminescence was studied in a monosilicate compound: $Er_{2-x}Yb_xSiO_5$. Thin films were grown both on Silicon and on SiO_2 substrates by spun solutions containing different percentages of Yb and Er [57].

The PL intensity was measured as a function of x at different wavelengths, in order to put in evidence the sensitization, as reported in fig. 4.19. By pumping the samples at 980 nm a 10 times increase of the PL intensity is registered for $x = 1.9$ compared with the 654 nm pump wavelength, and a further factor 20 increase was found on the same film grown on SiO_2. Note that 654 nm is resonant with the $^4F_{9/2}$ Er level, but it is not resonant with any Yb level, while at 980 nm both the rare earths absorb, but with a very different efficiency.

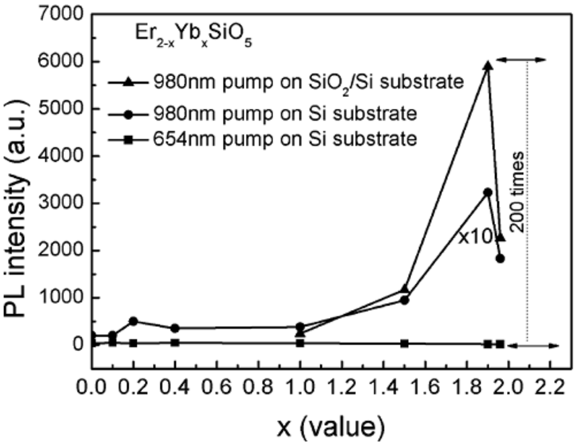

Figure 4.19: PL intensity of $Er_{2-x}Yb_xSiO_5$ thin films grown on Silicon and on silica, at two different pump wavelengths, 654 nm and 980 nm [57].

According to this promising and unique result, our purpose is to investigate the Yb-Er mixed disilicate, since it was already demonstrated that an α-disilicate environment has a better influence on the Erbium PL intensity rather than monosilicate. In the next chapter we will then show how we synthesized and analyzed Y-Er and Yb-Er mixed disilicates, and how we successfully correlated the structural properties to the optical ones.

References

[1] B. E. A. Saleh and M. C. Teich, *Fundamentals of Photonics*, John Wiley and Sons, New York, 2007.

[2] E. Desurvire, *Erbium-doped fiber amplifiers: principles and applications*, John Wiley and Sons, New York, 1994.

[3] G. E. Moore, Electronics **38**, (1965).

[4] T. Miya, Y. Terunuma, T. Hosaka and T. Miyashita, Electron. Lett. **15**, 108 (1979).

[5] W. J. Miniscalco, J. Lightwave Technol. **9**, 234 (1991).

[6] K. Nakagawa, S. Nishi, K. Aida and E. Yoneda, J. Lightwave Technol. **9**, 198 (1991).

[7] Z. Tong, C. Lundström, P. A. Andrekson, C. J. McKinstrie, M. Karlsson, D. J. Blessing, E. Tipsuwannakul, B. J. Puttnam, H. Toda and L. Grüner-Nielsen, Nature Photon. **5**, 430 (2011).

[8] G. Li, Nature Photon. **5**, 385 (2011).

[9] A. Alduino and M. Paniccia, Nature Photon. **1**, 153 (2007).

[10] M. Lipson, J. Lightwave Technol. **23**, 4222 (2005).

[11] K. K. Lee, D. R. Lim, L. C. Kimerling, J. Shin and F. Cerrina, Opt. Lett. **26**, 1888 (2001).

[12] V. R. Almeida, Q. Xu, C. A. Barrios and M. Lipson, Opt. Lett. **29**, 1209 (2004).

[13] Q. Xu, V. R. Almeida and M. Lipson, Opt. Lett. **29**, 1626 (2004).

[14] M. Galli, D. Gerace, A. Politi, M. Liscidini, M. Padrini, L. C. Andreani, A. Canino, M. Miritello, R. Lo Savio, A. Irrera and F. Priolo, Appl. Phys. Lett. **89**, 241114 (2006).

[15] L. Pavesi, L. Dal Negro, C. Mazzoleni, G. Franzò and F. Priolo, Nature **408**, 440 (2000).

[16] H. Rong, R. Jones, A. Liu, O. Cohen, D. Hak, M. Paniccia and A. Fanf, Nature **433**, 725 (2005).

[17] H. Rong, A. Liu, R. Jones, O. Cohen, D. Hak, M. Paniccia, A. Fanf and R. Nicolaescu, Nature **433**, 292 (2005).

[18] A. Polman, J. Appl. Phys. **82**, 1 (1997).

[19] P. G. Kik and A. Polman, MRS Bull. **23**, 4 (1998).

[20] A. Polman, D. C. Jacobson, D. J. Eaglesham, R. C. Kistler and J. M. Poate, J. Appl. Phys. **70**, 3778 (1991).

[21] E. Snoeks, P. Kik and A. Polman, Opt. Mater. **5**, 159 (1996).

[22] F. Priolo, G. Franzò, D. Pacifici, V. Vinciguerra, F. Iacona and A. Irrera, J. Appl. Phys. **89**, 264 (2001).

[23] E. Snoeks, G. N. van den Hoven, A. Polman, B. Hendriksen, M. B. J. Diemer and F. Priolo, J. Opt. Soc. Am. B **12**, 1468 (1995).

[24] D. L. Dexter, J. Chem. Phys. **21**, 836 (1953).

[25] K. Hattori, T. Kitagawa, M. Oguma, M. Wada, J. Temmyo and M. Horiguchi, Electron. Lett. **29**, 357 (1993).

[26] Y. C. Yan, A. J. Faber, H. de Waal, A. Polman and P. G. Kik, Appl. Phys. Lett. **71**, 2922 (1997).

[27] M. K. Smit and G. A. Acket, Thin Solid Films **138**, 171 (1986).

[28] R. Serna, M. Jimenez de Castro, J. A. Chaos, A. Suarez-Garcia, C. N. Alfonso, M. Fernandez and I. Vickridge, J. Appl. Phys. **90**, 5120 (2001).

[29] G. N. van den Hoven, E. Snoeks, A. Polman, C. van Dam, J. M. van Uffelen and M. K. Smit, J. Appl. Phys. **79**, 1258 (1996).

[30] P. G. Kik and A. Polman, J. Appl. Phys. **93**, 5008 (2003).

[31] G. Franzò, V. Vinciguerra and F. Priolo, Appl. Phys. A **69**, 3 (1999).

[32] D. Pacifici, G. Franzò, F. Priolo, F. Iacona and L. Dal Negro, Phys. Rev. B **67**, 245301 (2003).

[33] H.-S. Han, S.-Y. Seo and J. H. Shin, Appl. Phys. Lett. **79**, 4568 (2001).

[34] G. C. Valley, Opt. Fiber Technol. **7**, 21 (2001).

[35] G. C. Vienne, J. E. Caplen, L. Dong, J. D. Minnely, J. Nilsson and D. N. Paine, J. Lightwave Technol. **16**, 1990 (1998).

[36] H. S. Hsu, C. Cai and A. M. Armani, Opt. Expr. **17**, 23266 (2009).

[37] C. Strohhöfer and A. Polman, Opt. Mater. **21**, 705 (2003).

[38] R. Lo Savio, M. Miritello, P. Cardile and F. Priolo, J. Appl. Phys. **106**, 043512 (2009).

[39] M. Miritello, R. Lo Savio, A. M. Piro, G. Franzò, F. Priolo, F. Iacona and C. Bongiorno, J. Appl. Phys. **100**, 013502 (2006).

[40] J. Hoang, T. T. Van, M. Sawkar-Mathur, B. Hoex, M. C. M. van de Senden, W. M. M. Kessels, R. Ostroumov, K. L. Wang, J. R. Bargar and J. P. Chang, J. Appl. Phys. **101**, 123116 (2007).

[41] N. A. Toropov, F. Y. Galakhov and S. F. Konovalova, Bull. Acad. Sci. USSR Div. Chem. Sci. (Eng. Transl.) **8**, 1271 (1961).
[42] A. I. Becerro and A. Escudero, Phase Trans. **77**, 1093 (2004).
[43] J. Ito and H. Johnson, Am. Miner. **53**, 1940 (1968).
[44] JCPDS database, powder diffraction file no. 74-1994.
[45] JCPDS database, powder diffraction file no. 38-0223.
[46] JCPDS database, powder diffraction file no. 30-1439; G. Bocquillon, et al., C. R. Seances Acad. Sci., Ser. B **283**, 343 (1976).
[47] JCPDS database, powder diffraction file no. 38-0440; K. Liddell and D. Thompson, Trans. J. Br. Ceram. Soc. **85**, 17 (1986).
[48] JCPDS database, powder diffraction file no. 72-0649
[49] V. Kahlenberg, R. Kaindl and J. Konzett, Solid State Sci. **9**, 542 (2007).
[50] X. Ouyang, A. H. Kitai and R. Siegele, Thin Solid Films **254**, 268 (1995).
[51] T. Schweizer, T. Jensen, E. Heumann and G. Huber, Optics Comm. **118**, 557 (1995).
[52] K. Suh, J. H. Shin, S.-J. Seo and B.-S. Bae, Appl. Phys. Lett. **92**, 121910 (2008).
[53] K. Suh, H. Go, S.-Y. Lee, J. S. Chang, M.-S. Yang and J. H. Shin, Proc. of SPIE **6897**, 68970G (2008).
[54] Q. Y. Zhang, K. Pita, W. Ye, W. X. Que and C. H. Kam, Chem. Phys. Lett. **356**, 161 (2002).
[55] R. Lo Savio, M. Miritello, F. Iacona, A. M. Piro, M. G. Grimaldi and F. Priolo, Appl. Phys. Lett. **93**, 021919 (2008).
[56] M. Miritello, R. Lo Savio, F. Iacona, G. Franzò, A. Irrera, A. M. Piro, C. Bongiorno and F. Priolo, Adv. Mater. **19**, 1582 (2007).
[57] X. J. Wang, B. Wang, L. Wang, R. M. Guo, H. Isshiki, T. Kimura and Z. Zhou, Appl. Phys. Lett. **98**, 071903 (2011).

5. Er compounds for optical amplifiers

Yttrium-Erbium disilicates thin films, $Y_{2-x}Er_xSi_2O_7$, were synthesized by rf-magnetron sputtering, with different rare earth concentrations, by properly varying the rf powers applied to the SiO_2, Er_2O_3 and Y_2O_3 targets. The Er concentration was successfully continuously varied between the classical doping regime ($\sim10^{20}$ Er/cm^3) and the compound regime ($\sim10^{22}$ Er/cm^3).

After thermal annealing at 1200 °C, for 30 s in O_2 ambient, all the as-grown films crystallize in such a way that the α-polymorph is generated. When Er is embedded in this crystalline structure, it has a very intense photoluminescence signal at 1.54 μm. A strong correlation between the structural and the optical properties is found.

The effect of the Erbium concentration in the films is deeply studied. In particular we found that in low pumping flux regime a very interesting phenomenon takes place: quantum cutting. This phenomenon, thanks to the strong Er-Er interactions and cross-relaxations, actually distributes the energy of an incoming high energy photon in exciting many Er^{3+} ions, according to the conservation of the total energy principle. For instance, a 488 nm incoming photon can be cut in up to three excitations at 1.54 μm. It is possible to see the effect by looking at the effective excitation cross section of Er^{3+}, which increases by increasing the Er concentration, since this phenomenon has a stronger probability to occur. We demonstrated that quantum cutting occurs effectively at 488 nm (with an efficiency of 300%) and at 380 nm (with an efficiency of 370%). We demonstrated moreover that quantum cutting has exactly the same physical mechanism of upconversion (but in the opposite direction), and it is characterized by the same typical interaction times of upconversion, having these two phenomena the same physical root: the dipole-dipole interactions. The only difference is that upconversion occurs at high pumping fluxes.

We also analyzed the importance of Yb^{3+} in the Erbium excitation, by synthesizing $Yb_{2-x}Er_xSi_2O_7$ films. We demonstrated that at 980 nm Yb^{3+} actually excites Er^{3+} with an excitation cross section which is one order of magnitude higher than the direct absorption cross section of Er in silica glasses. In fact Yb^{3+} absorbs the incoming photons and then it effectively transfers its energy to a close Er^{3+} ion. We estimated the efficiency of the energy transfer and the strength of the interaction between Yb^{3+} and Er^{3+}, by looking at the change of lifetimes of Yb^{3+} in absence and in presence of Er^{3+}, which is nothing but a non-radiative channel for the Yb^{3+} decay.

We demonstrated that the interactions between Yb^{3+} and Er^{3+} have a benefic effect on the overall Erbium emission at 1.54 μm. In particular the best sample from the optical point of view was found to be the one with [Er] = 1.6 at.%, which represents the best compromise between emitting centers and Er^{3+} lifetime (about 4 ms). By comparing the two disilicates, we found that Yb-Er silicate has the best properties as a material for efficient optical amplification at 1.54 μm.

5.1 Synthesis and structural properties of $Y_{2-x}Er_xSi_2O_7$ thin films

Er-containing Yttrium silicate thin films were synthesized by rf-magnetron sputtering. This technique is very versatile, since it allows the contemporary sputtering from different sources. It is a technique fully compatible with the ultra-large scale integrated technology, thus contributing efficiently in the realization of Silicon compatible devices. The deposition system is based on an ultra-high vacuum (UHV) chamber, equipped with a load-lock chamber, which is used for loading the wafers. The base pressure before the deposition is about 10^{-9} mbar, which is reached by using a cryogenic pump. All the depositions were done in an Ar atmosphere at a pressure of 5×10^{-3} mbar, by rf cosputtering from three different targets, SiO_2, Y_2O_3 and Er_2O_3, on 5 in. (100) c-Si substrates heated up to 400 °C, and rotating at 30 rpm to guarantee a good uniformity of the film thickness.

The cosputtering was successfully performed thanks to three independent rf power generators that biased three different targets. By properly varying the powers supplied, thin films of $Y_{2-x}Er_xSi_2O_7$ with six different compositions were grown [1]. Apart from the extreme case of $x = 2$, a constant rf power of 300 W is applied to the SiO_2 target, while the powers applied to Y_2O_3 and Er_2O_3 were varied. The ratio between the powers applied to these targets was chosen after a proper calibration, in order to achieve a perfect control of the ratio between the rare earth concentration [RE] and the Silicon one [Si]. In this way a disilicate composition was obtained, such that [RE]:[Si]:[O] = 2:2:7.

The duration of the depositions was changed, in such a way to keep constant the thickness of the films, about 130 nm, as estimated by cross sectional Scanning Electron Microscopy (SEM) analyses.

The areal density of the elements was evaluated by Rutherford Backscattering Spectrometry (RBS), by using a 2 MeV He^+ beam in random configuration. The He^+ ions arrive on the samples and the energy of the backscattered ones is detected. The detector is a Si-Au Schottky diode, placed at an angle of 165°, with respect to the incident beam. This kind of detector gives a current pulse, proportional to the energy of the He^+ ions detected.

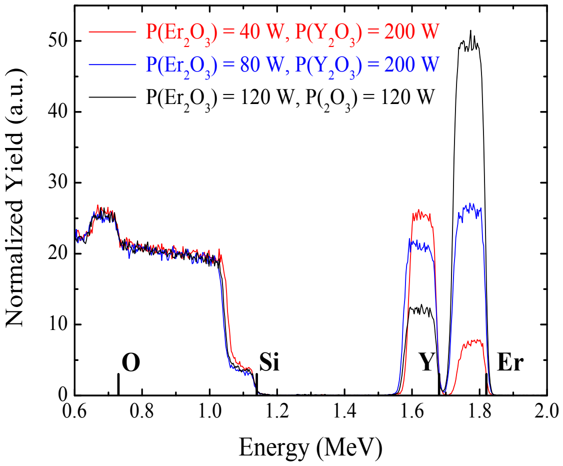

Figure 5.1: RBS spectra of three as-deposited $Y_{2-x}Er_xSi_2O_7$ films, with different powers applied to the targets. The O, Si, Y and Er signals at surface are indicated.

In fig. 5.1 three examples of RBS spectra are reported and they are referred to three different as deposited samples. The powers supplied to the rare earth targets are shown in the label. The spectrum represents the number of backscattering ions as a function of the energy. The energies of the ions backscattered by Oxygen, Silicon, Yttrium and Erbium in the surface are indicated by a bold marker. Each peak represents the profile in depth of a particular atomic species inside the sample. It is worth noticing that the profiles are constant throughout the whole thickness. Moreover, there is no evidence of Ar impurity inside the films.

The area of each peak is proportional to the areal density of the corresponding element. By dividing the areal density by the film thickness, the atomic concentration is obtained for each element.

Note that by increasing the power applied to Er_2O_3 target with respect to the power applied to Y_2O_3 one, the Er related yields increase. In any case, by considering the concentrations, all the grown films exhibit a [Y+Er]/[Si] ratio always equal to 1. The overall stoichiometry was then demonstrated to be [RE]:[Si]:[O] = 2:2:7, or equivalently $Y_{2-x}Er_xSi_2O_7$ films were grown with x varying between 0.03 and 2.

A summary of the growth conditions and the analytical results regarding the Erbium content is reported in table 5.1. This summary demonstrates effectively the versatility of the deposition system, since it is possible to achieve a perfect control of the stoichiometry. Now it is possible to study the optical properties of such films in which Erbium concentration is varied in a very big range, between 2×10^{20} and 1.5×10^{22} Er/cm^3, a two orders of magnitude range. Therefore we can conclude that we synthesized a quaternary compound in which Er concentration was varied by two orders of magnitude, thus moving gradually from the doping regime to the compound regime.

$P(Y_2O_3)$ W	$P(Er_2O_3)$ W	$P(SiO_2)$ W	Er content		Stoichiometry
			at. %	at/cm^3	
200	25	300	0.3	2×10^{20}	$Y_{1.97}Er_{0.03}Si_2O_7$
200	40	300	1.8	1.2×10^{21}	$Y_{1.83}Er_{0.17}Si_2O_7$
200	60	300	4.2	3.0×10^{21}	$Y_{1.60}Er_{0.40}Si_2O_7$
200	80	300	6.3	4.9×10^{21}	$Y_{1.35}Er_{0.65}Si_2O_7$
120	120	300	12.1	8.8×10^{21}	$Y_{0.85}Er_{1.15}Si_2O_7$
0	200	350	18.0	1.5×10^{22}	$Er_2Si_2O_7$

Table 5.1: Summary of the powers applied to the three targets (left) and of the Erbium concentrations and of the stoichiometries of the synthesized films.

In order to induce the crystallization of the as grown $Y_{2-x}Er_xSi_2O_7$ films and to reduce the defects, improving the Erbium luminescence, we thermally treated the samples, according to the phase diagrams of rare earth silicates [2-4]. We annealed the samples at 1200 °C for 30 s, and we observed the role of the atmosphere (O_2 and N_2) in the structural and in the optical properties. This rapid thermal annealing (RTA) was chosen because at this temperature it has been demonstrated that Erbium silicate thin films grown by sputtering [5] efficiently crystallize in the α phase, which is known to be the best one from the optical point of view.

After these annealings, no significant modifications occurred to the Y and Er peaks of the RBS spectrum, thus demonstrating a very good stability of these films on the Silicon substrate, even at these very high temperatures.

In order to analyze the structural properties X-ray diffraction (XRD) measurements were done, by using a Bruker-AXS D5005 diffractometer, with the Cu Kα radiation (λ = 1.54 Å), working at a grazing incident angle of 1.0°. The detection angle was varied between 15° and 60°, scanning with an angular step of 0.05°.

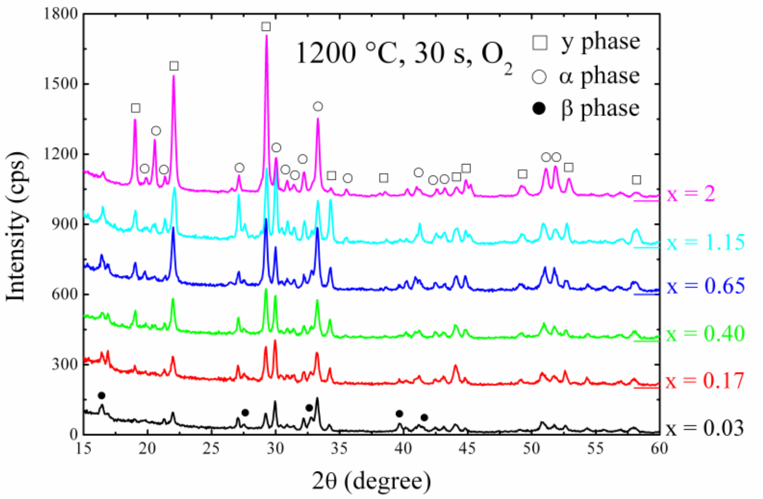

Figure 5.2: X-ray diffraction spectra of $Y_{2-x}Er_xSi_2O_7$ films grown on Silicon, after 1200 °C, 30 s, O_2. The peaks associated to three different polymorphs are indicated as open squares (y phase), open circles (α phase) and full circles (β phase).

Fig. 5.2 reports the XRD spectra of all the samples studied in the case of the annealing at 1200 °C, 30 s, in O_2 ambient. It is worth noticing that in all the cases, the diffraction spectra are characterized by narrow and sharp peaks, superimposed on a flat background, and this is an evidence of the film crystallization. The spectra show almost the same peaks, though a small shift is visible: in particular, by increasing the Er concentration, the peaks appear at larger 2θ. This is due to the fact that in the disilicate lattice Er^{3+} ions have an ionic radius of 0.88 Å, a bit smaller than the Y^{3+} one (0.89 Å). Therefore, by increasing Erbium, the crystal is slightly shrinking, because the lattice parameter is reducing, and this increases the diffraction angle. By comparing these peaks to the ones in literature, there is no evidence of the crystalline phases of Y or Er monosilicate (RE_2SiO_5) or of the relative oxides.

The observed peaks can be associated to the y, α and β polymorphs of Yttrium-Erbium disilicate, as it can be deduced by comparing the peak positions to the reference patterns of the JCPDS database [6-8]. In the figure the peaks related to these polymorphs are indicated with open squares (y), open circles (α) and full circles (β). However the relative intensities are changing by changing the Er content in the compound. In particular the most present peaks are related to y and α phases. A few peaks related to the β phase appear in the samples with the lowest Erbium concentration. Then, by increasing the Er content, this phase is reducing and finally it disappears in the $Er_2Si_2O_7$ film (x = 2). Since it is known that this phase can be formed at higher temperatures with respect to α and y, it can be deduced that the transition y $\rightarrow$ α $\rightarrow$ β are slightly lower in $Y_2Si_2O_7$. This is confirmed by the fact that, by annealing $Er_2Si_2O_7$ at 1300 °C, the β phase appear (not shown), moreover this has been also demonstrated in $Er_2Si_2O_7$ single crystals [9].

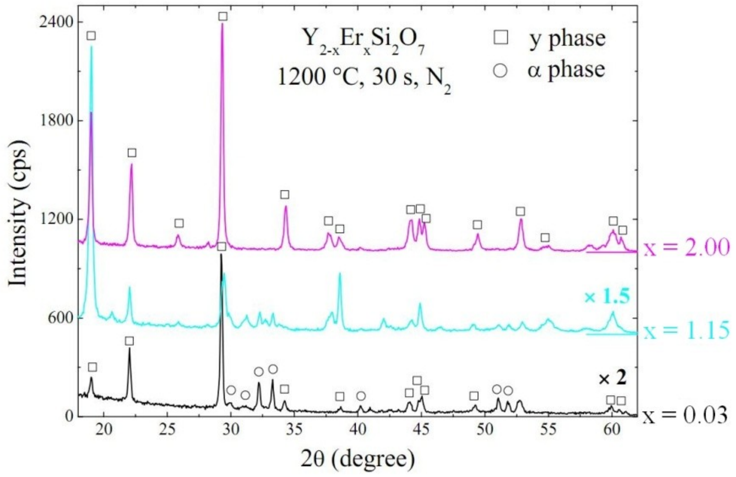

Figure 5.3: X-ray diffraction spectra of three $Y_{2-x}Er_xSi_2O_7$ films, after 1200 °C, 30 s, N_2. In this case only the peaks associated to y and α phases are registered. The spectra with x = 0.03 and 1.15 are multiplied by a factor 2 and 1.5 respectively for clarity.

Fig. 5.3 reports the XRD spectra of some $Y_{2-x}Er_xSi_2O_7$ films ($x = 0.03$, 1.15 and 2), annealed at 1200 °C, 30 s, in N_2. The N_2 environment is not reactive and therefore some differences can be found with respect to the annealing in O_2. Also in this case well defined peaks appear. All these peaks can be associated to a mixture of y and α phases of $Y_2Si_2O_7$. Moreover, by increasing Er content, the α phase decreases with respect to the y one. In fact for $x = 2$ peaks related just to the y phase are registered.

The α phase, therefore, disappears as soon as all the Y^{3+} ions are substituted by the Er^{3+} ones, and this may be due to a different crystallization temperature for the two rare earth silicates. As already said, no peaks related to the β phase are visible. It is then possible to deduce that Oxygen has an active role during the annealing, since additional kinetics lead to the formation of the β phase at lower temperature.

5.2 Optical properties of $Y_{2-x}Er_xSi_2O_7$ thin films

The optical properties of $Y_{2-x}Er_xSi_2O_7$ thin films grown by magnetron sputtering were investigated by photoluminescence spectroscopy (PL) and time-resolved measurements.

The photoluminescence spectroscopy is performed by focusing on the sample surface an incident beam at a fixed wavelength. The beam is modulated with a 11 Hz frequency, by an acousto-optic crystal. The Erbium ions are then excited and their photoluminescence is spectrally separated by using a monochromator (whose resolution is about 5 nm) and then is detected with a photomultiplier or a germanium detector. The detected signal is then sent to a lock-in amplifier. In this case we used two different light sources: an Ar laser, in particular the 488 nm line, and a Xe lamp, from which we selected with a monochromator an UV region around 380 nm.

Both these wavelengths are able to resonantly excite Er^{3+}: 488 nm is in fact resonant with the $^4I_{15/2} \rightarrow {}^4F_{7/2}$ transition (2.54 eV), while 380 nm is resonant with the $^4I_{15/2} \rightarrow {}^4G_{11/2}$ transition (3.26 eV), as shown in fig. 5.4, where a schematic of the Erbium energy levels involved is reported. In our experiments we looked at the Erbium emission at 1535 nm, which is the wavelength of the $^4I_{13/2} \rightarrow {}^4I_{15/2}$ transition (0.81 eV).

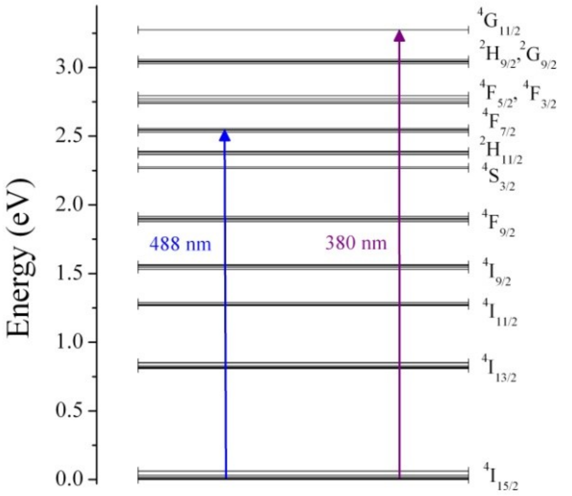

Figure 5.4: Schematic of the Erbium levels: the two excitation wavelengths are depicted in blue (488 nm) and in violet (380 nm).

Time-resolved measurements were performed in order to investigate the characteristic de-excitation times of the excited Erbium ions. When the light source is on, the Erbium ions absorb the incoming light and reach a steady state; when the source is off, on the contrary, the excited ions start decay with a lifetime τ, including the radiative and non-radiative decay paths. By looking at a fixed detected wavelength, the photoluminescence signal is sent to a multichannel analyzer, thus registering the decay curves. In some cases we performed these measurements at low temperatures by using a closed-cycle liquid He cooled cryostat, which is able to reach 11 K.

5.2.1 Correlation between structural and optical properties

The $Y_{2-x}Er_xSi_2O_7$ thin films, annealed at 1200 °C, 30 s, in N_2 and in O_2 ambient were analyzed, in order to understand the effect of the environment during the rapid thermal annealing in the crystallization.

In this case we fixed the excitation wavelength at 488 nm and we observed the Er^{3+} luminescence around 1.5 μm. All the samples exhibit an intense PL at this wavelength. However the emission spectrum is the convolution of all the possible transitions between the two multiplets $^4I_{13/2}$ and $^4I_{15/2}$, i.e. the two levels involved in the optical transition. This convolution is strongly dependent on the Stark splitting due to the crystalline field. In this material, we demonstrated the occurrence of different polymorphs, y, α and β, by performing XRD analyses. A qualitative comparison of the shapes of the emission spectra is reported in fig. 5.5. It is worth noticing that the shapes are deeply dependent on the crystalline environment around Erbium, since the emissions are peaked at slightly different wavelengths and are characterized by different features. However we are particularly interested in the α phase of Yttrium disilicate, since it was demonstrated that for Erbium disilicate this polymorph is the most efficient one from the optical point of view.

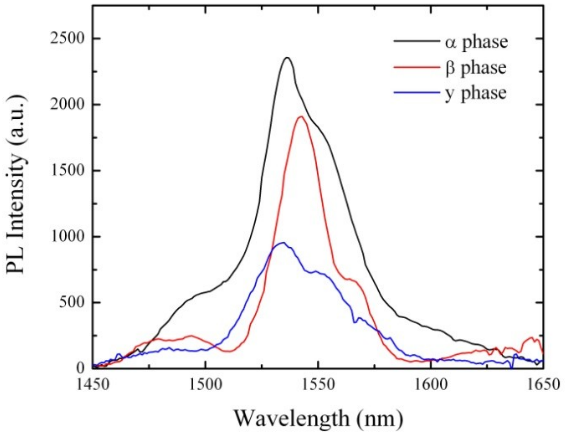

Figure 5.5: Different shapes of the Erbium spectrum associated to different crystalline phases.

Fig. 5.6 (a) reports the PL spectra of $Y_{2-x}Er_xSi_2O_7$ with an Er concentration of 0.3 at. % (x = 0.03), after thermal annealing at 1200 °C, 30 s, in N_2 and O_2. This is a sample in which Er is a dopant inside the $Y_2Si_2O_7$ matrix. For both annealings the spectrum has the same shape, the typical one of the α phase of Yttrium disilicate. Moreover the PL intensity is the same, independently of the annealing ambient.

In fig. 5.6 (b) the corresponding time-resolved measurements are reported at 1535 nm, where the emission is peaked. The decay curves are exactly superimposed, meaning that the lifetimes are the same. Up to x = 0.40 (an Erbium concentration of about 4.2 at.%) the N_2-treated and the O_2-treated samples show the same PL shape, with the same intensity and the same decay time.

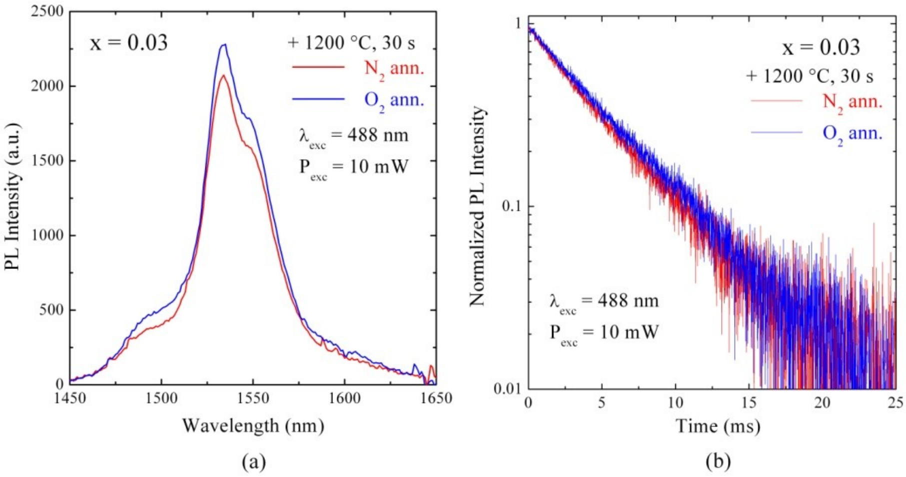

Figure 5.6: (a) Photoluminescence spectra of $Y_{1.97}Er_{0.03}Si_2O_7$ after thermal annealing at 1200 °C, 30 s, in N_2 (red) and in O_2 (blue) and the corresponding decays at 1535 nm as a function of time (b). The excitation power is 10 mW.

Therefore, up to this concentration, the $Y_{2-x}Er_xSi_2O_7$ thin films show a PL emission of Erbium embedded in the α polymorph of $Y_2Si_2O_7$. Moreover this emission does not depend on the annealing ambient. In these cases this particular phase is not sensitive to the presence of Oxygen vacancies, i.e. of defects due to the lack of Oxygen in the matrix. This is not the case for x higher than 0.40. When Er concentration is increased, in fact, as reported in fig. 5.7 (a) for x = 0.65, the shape of the PL spectrum depends on the annealing ambient. In the case of inert gas, N_2, the emission of Erbium can be ascribed to a crystalline environment of y phase. On the other side, in the case of O_2, the shape is the one of the α phase. Additionally the PL intensities are quite different, being the α phase much more optically efficient than the y one. Therefore we conclude that in this regime, in which Er is part of the compound, being inserted with a very high concentration (of the order of 10^{21} Er/cm^3), Oxygen has an important influence on the Er^{3+} emission at 1.5 μm.

These results are in agreement with the XRD analyses already shown in the previous section: in fact we have shown that by increasing Er, an increase of the y phase is registered at expenses of the α phase, after the annealing in Nitrogen. Now we have demonstrated that a prevalence of the y phase is registered also in photoluminescence.

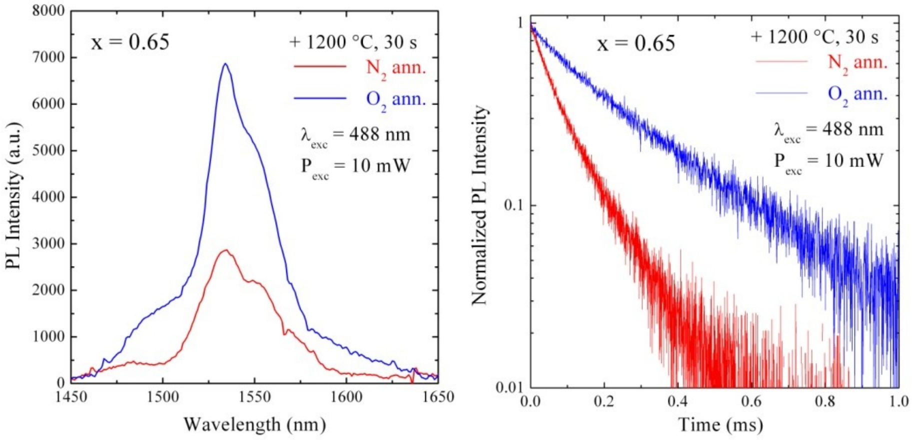

(a) (b)

Figure 5.7: (a) Photoluminescence spectra of $Y_{1.35}Er_{0.65}Si_2O_7$ after thermal annealing at 1200 °C, 30 s, in N_2 (red) and in O_2 (blue) and the corresponding decays at 1535 nm as a function of time (b). The excitation power is 10 mW.

In fig. 5.7 (b) the corresponding PL signal decays are reported. It is easy to see that in the case of Nitrogen, the decay is much faster, i.e. the lifetime is much shorter than for Oxygen. In this case the reduction of the PL intensity is well explained by a reduction of the lifetime. Probably, when the material crystallizes in this particular polymorph, the reduction of lifetime is due to a higher concentration of defects (such as Oxygen vacancies), acting as quenching centers for the Er luminescence.

Since there is such an important influence of the gas used in the thermal treatments, depending on the Er concentration, and given that the α phase of Yttrium disilicate was shown to be the most efficient, we will consider only the $Y_{2-x}Er_xSi_2O_7$ films thermally treated at 1200 °C for 30 s in

O_2 ambient. By using this annealing condition, in fact, all the films show an emission shape related to Er embedded in an α-phase crystalline environment.

5.2.2 Photoluminescence from Er in α-$Y_{2-x}Er_xSi_2O_7$

In order to investigate the optical emission from $Y_{2-x}Er_xSi_2O_7$ thin films, treated at 1200 °C for 30s in O_2, we performed photoluminescence spectroscopy. Erbium was excited by the 488 nm line of the Ar laser, at a pump power of 10 mW, and the emission around 1.54 μm was then analyzed [1].

The PL spectra of all the films are reported in Fig. 5.8: it is worth noticing that they are characterized by the very same shape, with a well defined peak at 1535 nm that can be associated to the α phase of the Yttrium-Erbium disilicate. The PL intensity tends to increase by increasing Er up to $x = 0.65$, then it slightly decreases and finally it increases again, reaching the maximum value for Erbium disilicate ($x = 2$).

At low pump fluxes, the photoluminescence intensity is related to many parameters, according to the equation:

$$I_{PL} \propto \qquad \frac{\tau}{\tau_{rad}}, \tag{5.1}$$

being σ the absorption cross section of Er^{3+} at the particular used wavelength, φ the excitation flux, N_{Er} the number of Er^{3+} ions in the film, τ_{rad} the radiative lifetime at 1.54 μm and τ the overall lifetime at the same wavelength, including both the radiative and the non-radiative decay paths.

According to this equation, the PL intensity is determined by the Er content and by the lifetime. Therefore we performed also the time-resolved measurements, which are useful in order to understand the dynamics of the Er^{3+} de-excitation from a particular energy level. All the measurements are reported in fig. 5.9 for all the x values studied. The PL intensity decay becomes faster when Er concentration is raised: this means qualitatively that the lifetime decreases by increasing x, i.e. by reducing the mean Er-Er distance. This distance is the critical parameter for the occurrence of concentration quenching phenomenon.

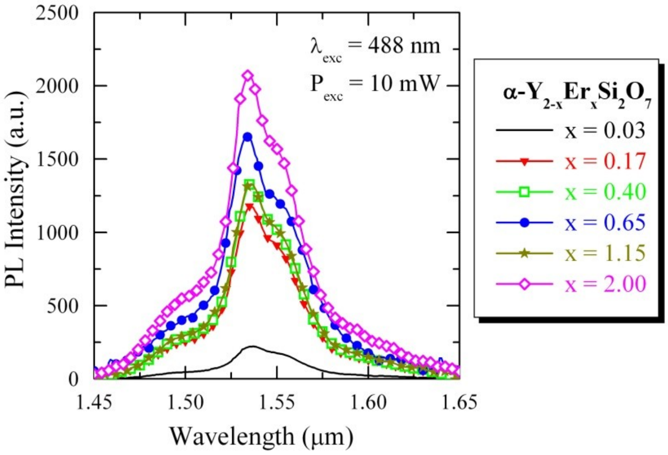

Figure 5.8: PL spectra of $Y_{2-x}Er_xSi_2O_7$ films, treated at 1200 °C, 30 s, in O_2. The excitation wavelength was 488 nm and the pump power was 10 mW.

Note that the decay is a single exponential up to *x* = 0.17, while it becomes slightly stretched by increasing the Erbium content. The reason is that at the used excitation power, cooperative upconversion takes place due to Er-Er interaction. This behavior is well modeled by considering the complete rate equation regarding the first excited state:

$$\frac{dN_1}{dt} = \qquad - \frac{N}{\tau} - \qquad . \tag{5.2}$$

where N_1 is the population of the first excited state ($^4I_{13/2}$), N_0 is the population of the ground state ($^4I_{15/2}$) and C_{up} is the upconversion coefficient. The physical meaning of this equation is that the first excited level is populated by the excitation flux, and is depopulated by the normal decay with a lifetime τ and by the upconversion process. This latter phenomenon occurs if two ions are close one another and are at the same time in the first excited level. They can interact and one ion is de-excited to the ground level, while the other one is brought in a higher level, coming quickly back to the $^4I_{13/2}$ level. Therefore the term in the equation is quadratic.

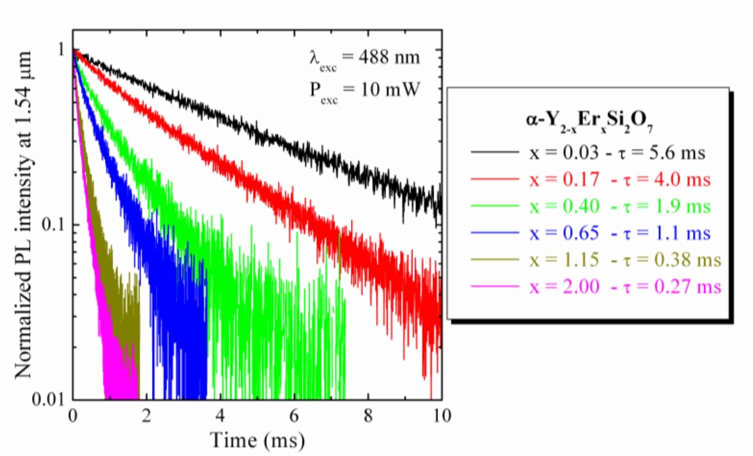

Figure 5.9: PL intensity decay at 1.54 µm for each *x* considered. The excitation wavelength is 488 nm and the pump power is 10 mW. The lifetimes obtained by fitting the decay curves with the equation (5.3) are reported in the legend.

When the excitation source is switched off (φ = 0) the equation can be analytically solved and the solution representing the trend of $N_1(t)$, that is the Er population in the first excited state as a function of time, is the following:

$$\frac{N_1(t)}{N_1(0)} = \lfloor 1 + \quad - \quad - \quad) \tag{5.3}$$

where $N_1(0)$ is the population in the $^4I_{13/2}$ level in steady state condition (laser off). Since the PL intensity is proportional to Er population, we can say that the ratio $N_1(t)/N_1(0)$ can be written as $I_1(t)/I_1(0)$, which is the trend of the normalized PL intensity as a function of time. Therefore we can fit our decay curves and we can find τ as a fitting parameter. The values obtained by the fits are reported in the legend of fig. 5.9: it is worth noticing that τ decreases from 5.6 ms to 0.27 ms, by increasing Er by two orders of magnitude.

5.3 Er-Er interactions in $Y_{2-x}Er_xSi_2O_7$

We have seen that in an Er-containing system such as $Y_{2-x}Er_xSi_2O_7$ films, when Er concentration is increased, many ion-ion interactions may occur, due to the reduction of the distance between two Er ions. These phenomena have strong and detrimental effects on the final optical emission, since concentration quenching reduces the Er lifetime, while upconversion reduces the Er population in the first excited state at high pump fluxes. In this section we analyze properly all the ion-ion interactions, showing that in some cases they can have a positive effect for Erbium.

5.3.1 Influence of Er concentration on the optical emission from $Y_{2-x}Er_xSi_2O_7$

When Erbium concentration is increased in the matrix, ion-ion coupling becomes stronger and stronger, since dipole-dipole interactions start to occur due to the fact that their strength is proportional to $1/d^6$, being d the mean Er-Er distance. The most important physical consequence is that, when the excitation source is switched off, the de-excitation from the first excited level happens in a shorter characteristic time. We have already seen that in our samples the lifetime decreases by one order of magnitude, by increasing the Er concentration by two orders of magnitude. This is the concentration quenching phenomenon, already described in section 4.3.1.

Fig. 5.10 reports the decay rate W_{Er}, which is plotted as a function of N_{Er} (lower axis) and x (upper axis). Note that the decay rate increases monotonically by increasing N_{Er}. Up to $x = 0.65$, the increase has a linear trend, following the equation (4.2), well known to be valid for Er-doped materials [10] and here reported:

$$W_{Er} = \qquad + \qquad N_{Er} N_Q, \tag{5.4}$$

being W_0 the reciprocal of the lifetime in absence of concentration quenching, i.e. in the limit of no Er-Er interactions, $C_{Er\text{-}Er}$ the coupling constant in the particular matrix considered, N_{Er} the Erbium concentration and N_Q the density of quenching centers. Therefore, by performing a linear fit of our data up to $x = 0.65$, it is possible to obtain both W_0 and the slope. From W_0 (130 s^{-1}) we can deduce that the radiative lifetime of Er in $Y_2Si_2O_7$ is 8 ± 1 ms, comparable with the radiative lifetime observed in A-Y_2SiO_5 nanoparticles [11] and B-Y_2SiO_5 single crystals [12, 13].

At x higher than 0.65, the linear regime is not valid anymore, since the law expressed in equation (5.4) is good just for low Erbium concentrations.

However, the decay rate has a further increase, since Er^{3+} is gradually replacing all the Y^{3+} ions in the lattice, implying that Er-Er interactions are more and more probable.

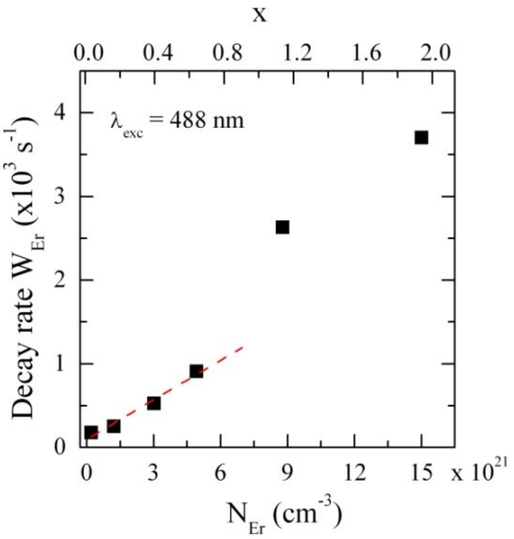

Figure 5.10: Decay rate at 1.54 μm as a function of Er concentration. The linear fit in the limit of $x \leq 0.65$ is reported as a dashed red line.

In order to deeply investigate the Er^{3+} properties in our $Y_{2-x}Er_xSi_2O_7$ films, we fixed a pump power of 1 mW, that corresponds to a photon flux of 1.2×10^{19} photons/($cm^2\cdot s$). This flux was chosen because in this experimental condition we verified that the PL intensity is proportional to the flux for all the samples. This is an important condition, because it means that for all the studied samples we can rewrite equation (5.1) in the following way:

$$I_{PL} = \qquad \frac{\tau}{\tau_{rad}}, \qquad (5.5)$$

in which all the parameters were already described, except for A. This is the detection efficiency, which allows to write the equation as an identity and not as a relation of proportionality. This parameter is the same for all the samples, since it depends on the detection set up. As far as the absorption cross section is concerned, we know the exact value of σ for Erbium at 488 nm, which is 2.2×10^{-21} cm^2 [14], that is valid for direct absorption of Er^{3+} in systems in which is diluted as a dopant. Finally τ_{rad} is constant whatever is x.

In fact, it depends only on the refractive index and for both Yttrium silicate and Erbium silicate the refractive index is 1.9.

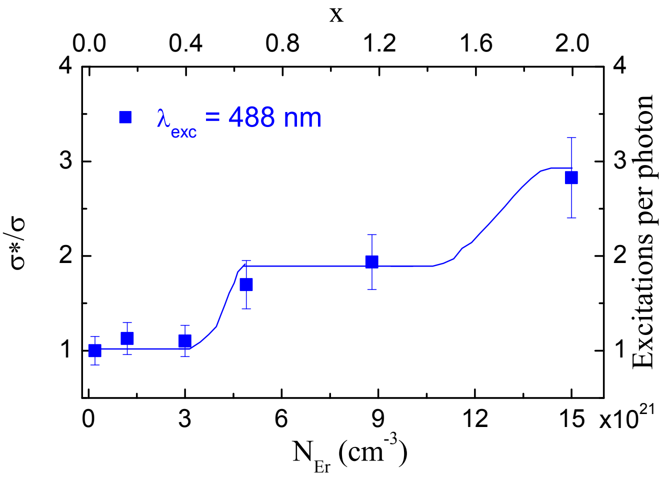

Figure 5.11: I_{PL} / (N_{Er}·τ) ratio, normalized to the value obtained for *x* = 0.03, the most dilute Er-containing system, as a function of the Erbium concentration for λ_{exc} = 488 nm. The line is a guide for the eye [1].

However, by analyzing the ratio $I_{PL}/(N_{Er}\cdot\tau)$, which is reported in fig. 5.11, normalized by the value obtained from the most dilute Er-containing system, we observed that this ratio is not constant, as a function of the Er concentration. Since A and φ are fixed, it is possible to deduce that the normalized ratio represents nothing but an effective cross section. Moreover it is reasonable to suppose that for *x* = 0.03, a sample in which Er is a dopant, the excitation cross section is the one provided by Miniscalco [14], σ = 2.2×10^{-21} cm^2. Therefore the normalized ratio represents exactly σ*/σ, being σ* an effective excitation cross section [1].

Since σ is the probability that an Er^{3+} ion is excited by an absorbed incoming photon, and since σ* increases by increasing the Er content, we can also say that the normalized ratio σ*/σ is a measurement of the number of excitations to the $^4I_{13/2}$ level that can be done by an absorbed photon. It is worth noticing that the number of excitations per photon is 1 up to *x* = 0.40, then it doubles at *x* = 0.65, and finally it becomes 3 for *x* = 2.00, that is the Erbium silicate sample [1].

5.3.2 Quantum cutting effect

In order to explain the trend already described in the previous subsection, we suggest the hypothesis that a quantum cutting phenomenon is occurring. This phenomenon takes place with higher probability by increasing the amount of Erbium.

Quantum cutting is well known (also with the name of downconversion) in the photovoltaics world, since it is studied with the aim of improving the efficiency of solar cells. The phenomenon was demonstrated for different materials, particularly the rare earth-based ones [15]. A high energy incoming photon impinging on a downconverter layer, results in the emission of more than one low-energy photon. The excess of energy with respect to the bandgap of the semiconductor, usually lost by thermalization of carriers [16], here is gained, since there are more than one low energy photons that can be absorbed, thus multiplying the photocarriers [17]. Different mechanisms were identified in literature: a radiative cascade in a single ion, with an efficiency of 140 % (i.e. 1.4 photons emitted per one absorbed) for Pr^{3+} in YF_3 [18] or a coupling between pairs of rare earth ions, like Gd^{3+} and Eu^{3+} in $LiGdF_4$, with an efficiency of 200 % by changing an UV photon into two visible ones [19] or between Tm^{3+} and Yb^{3+}, with an efficiency of about 180 %, by transforming a visible photon into two IR ones [20].

In our case, we excite Er^{3+} with the 488 nm line of the Ar laser. This wavelength corresponds to an excitation energy of 2.5 eV: a photon with this energy brings Er^{3+} from the ground state to the $^4F_{7/2}$ level, as shown in fig.5.12, left panel. In the case of the low concentration regime, it is known that Er^{3+} fastly decays from the excited level to the low lying level $^4S_{3/2}$ (with a characteristic multiphononic relaxation of about 50 ns); in this level the multiphononic relaxation is slower, but it is still of about 5 μs; then usually Er^{3+} decays down to the $^4I_{13/2}$ level and finally an infrared photon at 1.54 μm can be emitted. These multiphononic relaxations characterize the typical non radiative channels of such a cascade for Er^{3+}.

Now let us suppose that in a time equal or shorter than 5 μs, this excited Er^{3+} interacts by dipole-dipole with a neighbor Er^{3+} ion in the ground state. A cross relaxation ($^4S_{3/2} \rightarrow {}^4I_{9/2}$, $^4I_{15/2} \rightarrow {}^4I_{13/2}$) may occur, as indicated in fig. 5.12 middle panel, due to the fact that this involves jumps of the very same energy. This process can take place at high Er concentrations, since it needs a high number of ions in the ground state. Additionally a cross relaxation is more probable by increasing the Er content, i.e. by reducing the distance between two ions. If this mechanism occurs, at least two ions will have the possibility to emit an infrared photon at 1.54 μm, because two ions will certainly arrive in the first excited state, per each 488 nm photon absorbed. This is a quantum cutting phenomenon, since a visible photon has been used to excite two Erbium ions, having finally the possibility to achieve two IR photons emitted.

Furthermore the Er^{3+} ion, brought to the $^4I_{9/2}$ level, can either decay to the $^4I_{11/2}$ level with a multiphononic relaxation of 200 ns, or it can interact again with another Er^{3+} ion in the ground state, with another cross relaxation ($^4I_{9/2} \rightarrow {}^4I_{13/2}$, $^4I_{15/2} \rightarrow {}^4I_{13/2}$). If the cross relaxation is faster than 200 ns, therefore, we could have up to three Er^{3+} ions emitting at 1.54 μm, per each 488 nm photon absorbed. This is thought to happen for the highest Er containing system, where the Er-Er interactions are very easy to take place.

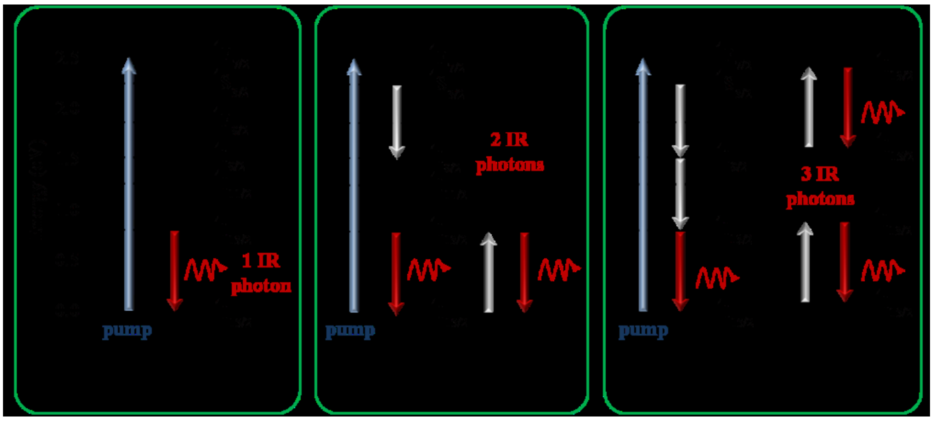

Figure 5.12: Schematic picture of the cross-energy processes, involving Er^{3+} in the three concentration regimes: low (left panel), medium (middle panel) and high Er concentration (right panel). The dashed lines represent non radiative multiphononic relaxation, light grey bold arrows indicate the cross relaxations. Red bold arrows indicate the emission of IR photons at 1.54 μm [1].

The non radiative multiphononic decay rates were taken from ref. [12], and the radiative probability was neglected. This is justified since we performed PL spectroscopy (not shown) and no emission was observed from all the levels beyond the $^4F_{7/2}$ level (with the exception of the first excited level, of course). The situation depicted in fig. 5.12 and just described seems to be in good agreement with our experimental data, reported in fig. 5.11, where we observed an increase by steps of the effective excitation cross section. In fact, a channel for the first cross relaxation is open when Er concentration reaches $x = 0.65$, thus allowing two excitations per photon absorbed; but in this regime the second cross relaxation is still not possible, since it requires faster Er-Er interactions. Finally for $x = 2.00$, also the second cross relaxation becomes possible and three excitations per photon are reached [1].

In order to demonstrate properly that this is the right explanation of our experiment, we performed the same measurements, under different experimental conditions. In particular we used the Xe lamp, by selecting a window around 380 nm with a monochromator. This wavelength, corresponding to an energy of 3.26 eV, is resonant with the $^2G_{11/2}$ Er level. Also in this case we verified that the photoluminescence is the one typical of Er^{3+} in α-$Y_{2-x}Er_xSi_2O_7$.

When Erbium is excited in such a high energy level, many cross relaxations may occur and they are depicted and labeled in fig. 5.13. Note that processes (a), (b) and (c) can individually give four excitations per photon absorbed. In fact the (a) process is ($^2G_{11/2} \rightarrow {}^4F_{7/2}$, $^4I_{15/2} \rightarrow {}^4I_{13/2}$): in this way the first ion in the $^4F_{7/2}$ level can follow the same path described previously, thus giving the possibility to have three Er^{3+} ions in the $^4I_{13/2}$ level, while the second one, arriving in the first excited level, is the fourth excited ion per each UV photon absorbed. This is also true for the (b) process, which is ($^2H_{9/2} \rightarrow {}^4S_{3/2}$, $^4I_{15/2} \rightarrow {}^4I_{13/2}$). In the best case, also here we can achieve at the end a four excitations quantum cutting at 1.54 μm. The (c) process is ($^2H_{9/2} \rightarrow {}^4I_{9/2}$, $^4I_{15/2} \rightarrow {}^4I_{9/2}$): since each ion in the $^4I_{9/2}$ level may give rise in principle to two excitations, also in this case it is possible to have four excitations.

On the other side the (d) process, which is ($^4F_{3/2} \rightarrow {}^4I_{9/2}$, $^4I_{15/2} \rightarrow {}^4I_{11/2}$), is a three excitations quantum cutting mechanism, since one Er^{3+} ion is in the

$^4I_{9/2}$ (two excitations in the best case) and another one is in the $^4I_{11/2}$, and it can just decay to the first excited state.

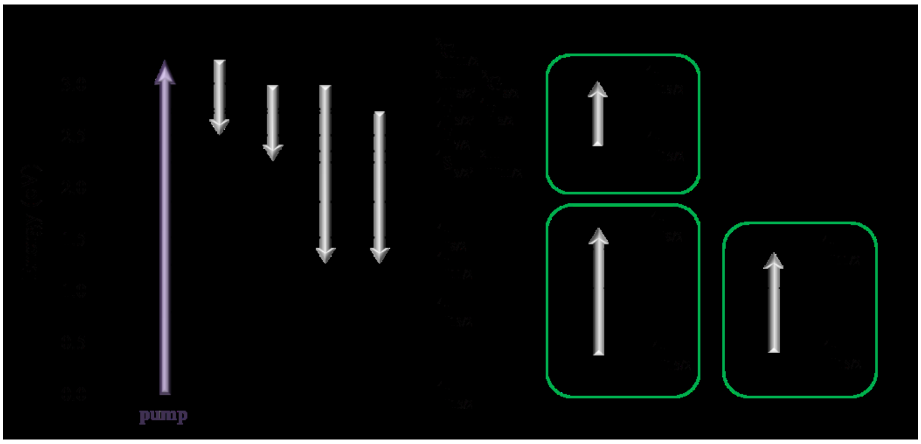

Figure 5.13: Schematic picture of the four possible high energy levels cross relaxation processes. With (a), (b) and (c) four 1.54 μm excitations are possible, whilst with (d) only three. The dashed lines represent non radiative multiphononic relaxation, light grey bold arrows indicate the cross relaxations [1].

More cross relaxations are possible, but they are already encountered in the previous description of the 488 nm excitation source. Moreover, also for the UV excitation it is possible that multiphononic relaxations occur. However in this case, many independent "channels" of cross relaxations can be passed through by the Erbium ions, and therefore the possibility to obtain the maximum number of excitations (four in this case) at 1.54 μm is increased [1].

We analyzed the ratio $I_{PL}/(N_{Er}\cdot\tau)$ by using the 380 nm excitation wavelength and it is reported in fig. 5.14 (a), compared to the one obtained by pumping at 488 nm, placed in the same figure as a reference (b). The power used is 3 mW, and also here it was verified to be in a linear regime of the PL intensity versus power. The lifetimes, moreover, were confirmed not to depend on the excitation wavelength used. The ratio $I_{PL}/(N_{Er}\cdot\tau)$ was normalized to the value obtained for $x = 0.17$, since for the most dilute Er-containing sample the PL intensity was too low to be detected.

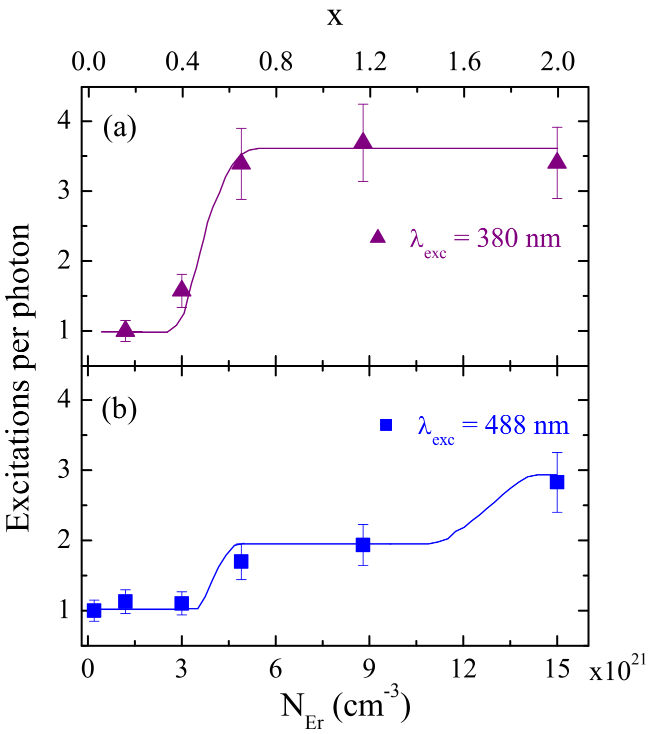

Figure 5.14: (a) I_{PL} / (N_{Er}·τ) ratio at 380 nm, normalized to the value obtained for *x* = 0.17, as a function of the Erbium concentration. The line is a guide for the eye. (b) Reference trend at 488 nm, as shown in fig.5.11 [1].

The trend of $I_{PL}/(N_{Er}\cdot\tau)$ at 380 nm shows a quantum cutting threshold slightly shifted towards lower Er concentrations, with respect to the 488 nm one. In fact, for $x = 0.40$, the number of excitations per photon absorbed is 1.5, due to the existence of the listed cross relaxations that allow to have a quantum cutting effect already for low Er-containing Yttrium α-disilicate films. By increasing the Er content, a further increase of excitations per photon is observed, up to ~3.7, which is very close to 4, and it is constant for $0.40 \leq x \leq 2.00$. Therefore the maximum efficiency of quantum cutting here is reached at $x = 0.40$. A possible explanation for this strange behavior may be due to the fact that, although each cross relaxation competes against the multiphononic decay, the existence of such many different processes guarantees that in some way quantum cutting occurs, involving one of the pairs of levels, listed previously [1].

Note that the effect is efficient when Er concentration is high enough. Moreover this effect competes with upconversion, of course, since also upconversion involves Er-Er interactions, but these are different. At low pumping fluxes, upconversion is negligible, while downconversion has a predominant role in the Er^{3+} dynamics. In particular we have demonstrated that $Y_{2-x}Er_xSi_2O_7$ films are very interesting compounds for the occurrence of the downconversion, being promising as downconverting layers for Ge solar cells. In fact, the quantum cutting effect here cuts photons at 488 nm (2.54 eV) and at 380 nm (3.25 eV) in three and four photons respectively at 1.54 μm, corresponding to an energy of 0.8 eV, which is just above the Ge bandgap.

A further proof that in our material quantum cutting is working comes from low temperature measurements. We performed PL measurements at 11 K, by using the liquid He cooled cryostat. The measurements were done again with the 488 nm line of the Ar laser. Fig. 5.15 (a) reports the complete PL spectrum for Erbium disilicate, i.e. for $x = 2.00$, at 11 K (red line). This spectrum is characterized by three narrow peaks that can be associated with the transitions from the high energy levels to the ground state, as labeled in the figure. The first peak is in the visible, at about 560 nm, and can be associated to the transition $^4S_{3/2} \rightarrow {}^4I_{15/2}$. The other two peaks are in the IR, at 980 nm and at 1.54 μm, respectively related to the transitions $^4I_{11/2} \rightarrow {}^4I_{15/2}$ and $^4I_{13/2} \rightarrow {}^4I_{15/2}$. In the same figure the PL spectrum at 300 K is reported in blue. The spectra were normalized, in order to have the same intensity at 1.54 μm, thus allowing to appreciate in a better way the difference. In order to do this, the PL spectrum at 11 K was multiplied by a factor 10.

The shape of the peak at 1.54 μm is much broader at 300 K, with respect to the one at 11 K. This is due to the different thermal population in the Er^{3+} multiplets: in fact at cryogenic temperatures only the lowest lying sublevels of the manifolds are involved in the transitions. Another important difference is that at 300 K only the peak at 1.54 μm is detectable.

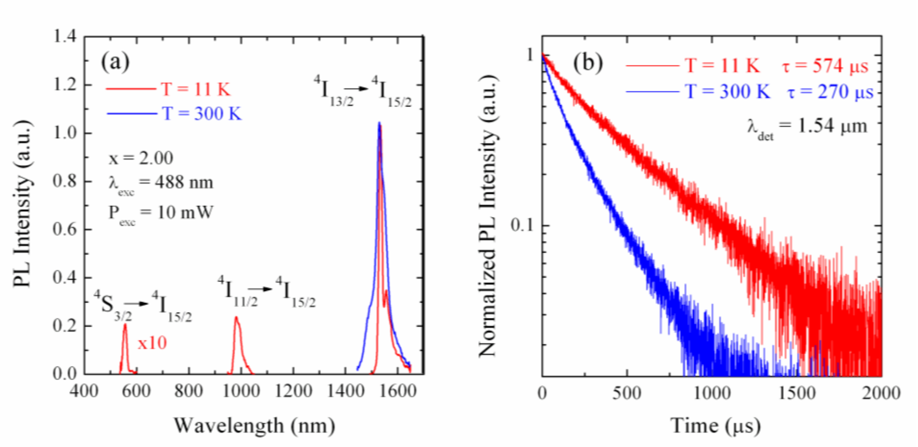

Figure 5.15: (a) PL spectrum at 11 K (red) and at 300 K (blue) for Erbium disilicate ($x = 2.00$); all the peaks were identified and labeled. (b) PL decays at 1.54 μm at 11 K (red) and at 300 K (blue).

Additionally in fig. 5.15 (b) we reported the PL intensity decay at 1.54 μm, at both the temperatures investigated. Note that at low temperature the lifetime is definitely longer, being 574 μs, instead at 300 K it is 270 μs. The reason is that the population of phonons decreases exponentially with the temperature, being regulated by a Bose-Einstein distribution [21]. Therefore an increase of the non-radiative decay time is expected, resulting in a longer overall decay time. This reduction of the non-radiative decay processes probability is also the reason why we observe PL emission at 560 nm visible and at 980 nm from Er^{3+}.

Actually an excited Er^{3+} ion has three different competing decay paths: the non radiative multiphononic decay to the lower lying levels, the cross relaxations and the radiative decay. We can then deduce that at 11 K the fastest path is the last one.

The ratio $I_{PL} / (N_{Er} \cdot \tau)$ at 1.54 μm was studied also at this cryogenic temperature, for three different Erbium concentrations, low ($x = 0.03$), medium ($x = 0.65$) and high ($x = 2.00$), and it is reported in fig. 5.16. The number of excitations per photon is one for the whole Er concentration regime investigated, i.e. the excitation cross section is the same of the absorption cross section for all the Erbium contents and no quantum cutting occurs. This is due essentially to the fact that cross relaxations here are not the preferred path, even at very high Erbium concentrations, thus allowing to have a detectable PL emission in the visible and at 980 nm.

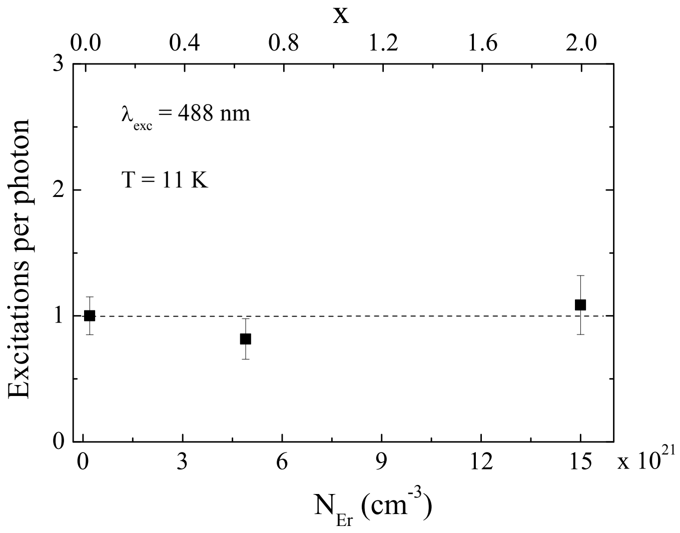

Figure 5.16: Excitations per absorbed photon at λ_{exc} = 488 nm, normalized to the value obtained for $x = 0.03$, as a function of the Erbium concentration, at 11 K. The dashed line is a guide for the eye.

Moreover it is worth reminding that the PL shapes are much narrower at this low temperature, since not all the multiplets are thermally populated with electrons. This was clearly observed at 1.54 μm, but it is a general result. Since the occurrence of quantum cutting is directly related to Er-Er interactions, which are due to the superimposition integral of the involved manifolds, now quantum cutting does not take place, because the manifolds are much narrower and the coupling probability tends to zero, thus increasing the probability of the radiative decay path.

5.3.3 Cooperative upconversion

In this subsection we address the problem of upconversion phenomena in $Y_{2-x}Er_xSi_2O_7$ films as a function of the Erbium content. This is another Er-

Er interaction, known to occur at high pumping fluxes, i.e. in a regime completely different from the quantum cutting.

PL measurements as a function of the pumping flux were done at 488 nm, and the experimental points are reported in fig. 5.17 in a log-log plot, for three different Erbium concentrations: x = 0.03, 0.65 and 2.00, i.e. for low, medium and high Erbium contents.

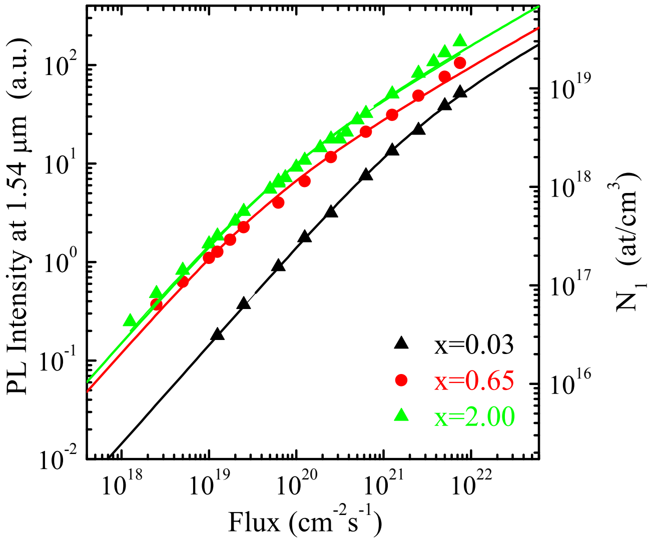

Figure 5.17: PL intensity at 1.54 μm as a function of the pumping flux, for x = 0.03, 0.65 and 2.00. Continuous lines are the fit to the data, according to equation (5.7). The right axis reports the population in the first excited state [1].

For all the samples investigated, in the regime of low pumping fluxes, the PL intensity is linear with the flux, because the trends show a slope 1 in that regime, in the log-log scale. At high fluxes the curves tend to saturate, due to the occurrence of upconversion. Note that the saturation starts at lower fluxes as the Er concentration increases, because lower fluxes are necessary to the onset of upconversion-like interactions.

The rate equation describing the dynamics of the first excited state level is equation (5.2), here reported:

$$\frac{dN_1}{dt} = \qquad - \frac{N}{\tau} - \qquad . \tag{5.6}$$

which can be solved in steady state condition, thus obtaining $N_1(\varphi)$. In fact, in this condition the time derivative is zero, and by using the boundary condition that $N_0 = N_{Er} - N_1$ (i.e. the population in the higher levels is negligible) we have to solve a quadratic equation, with the following solution:

$$N_1(\varphi) = \sqrt{1} + \frac{\qquad + \qquad + \qquad - \quad +}{2C_{up}\tau}. \tag{5.7}$$

Since the PL intensity is proportional to N_1, we can perform a fit to the experimental data with the equation (5.7), by multiplying N_1 by a constant factor B, containing all the proportionality terms. Particularly, B is proportional to the radiative de-excitation rate $1/\tau_{rad}$ that is the probability that a photon is emitted; moreover B is proportional to the extraction efficiency P_e, that is the probability that an emitted photon is extracted out from the sample. By considering that the emitted photons must escape from an interface silicate/air, thus being totally reflected if the angle is larger than the critical angle θ_c, P_e can be expressed by the ratio between the maximum solid outcoming angle and 4π:

$$P_e = \frac{1}{2} \quad - \qquad = \frac{1}{2}\left(\qquad \right) \tag{5.8}$$

where n is the refractive index of the film. Finally B is proportional to the detection efficiency η_D, which depends on the geometry of the apparatus and on the particular detector used.

Among all the parameters in equation (5.7), τ is known because it has been obtained by the fit of all the PL signal decays; σ is the absorption cross section, and it has been fixed, by considering the respective values obtained for each Er concentration, i.e. 2.2×10^{-21}, 4.4×10^{-21} and 6.6×10^{-21}, depending on the Er content. The free parameters of the fit are then B and C_{up}.

The curves fit perfectly the experimental data, and actually this is true only for those specific values of σ. It is indeed impossible to fit the data with just a single value of excitation cross section. This is a further confirmation of the quantum cutting phenomenon [1].

Table 5.2 reports the parameters obtained from the fit to the data in fig. 5.17, by using equation (5.7). The C_{up} coefficient increases by two orders of magnitude, being 2.3×10^{-17} cm^3/s for $x = 0.03$, 6.4×10^{-16} cm^3/s for $x = 0.65$, and 1.1×10^{-15} cm^3/s for $x = 2.00$. The lowest value is the first measurement of Er embedded in α-$Y_2Si_2O_7$ silicate, and it is of the same order of magnitude of Er embedded in silica [22], Al_2O_3 [23]. The noticeable increase of C_{up} when the Er content is increased may be due to the fact that this coefficient has been demonstrated to be dependent also on Er concentrations in some cases [24, 25]. Moreover, in the case of Er disilicate ($x = 2.00$) strong Er-Er interactions are expected to happen, thus increasing the probability of occurrence of upconversion.

x	C_{up} [cm^3/s]	Max N_1/N_{Er} [%]	Interaction time $(C_{up}\cdot N_{Er})^{-1}$
0.03	2.3×10^{-17}	4 %	200 μs
0.65	6.4×10^{-16}	0.4 %	300 ns
2.00	1.1×10^{-15}	0.2 %	50 ns

Table 5.2: Summary of results obtained from the fit to the data points in fig. 5.17 by using equation (5.7). The C_{up} coefficient, the maximum achieved number of ions in the first excited state, and the typical upconversion interaction times are reported.

In the third column of table 5.2, the maximum fraction of population in the first excited state is reported. This parameter can be obtained by converting the PL intensity scale in a population scale, as it is written in the right axis of fig. 5.17. This conversion was done by using the fit parameter B, which was found to be 5.4×10^{-24} cm^3 for all the samples. A direct measurement of N_1 was done also by comparing the measured PL intensity of a reference sample of Er-doped silica, in which 5×10^{19} Er/cm^3 are inserted. For this reference sample, all the Er^{3+} ions are optically active and the excitation cross section is the well known value, given by Miniscalco [14], 2.2×10^{-21} cm^2. Therefore, for low pumping fluxes, we can write:

$$I^r_{PL} = \frac{\tau^r}{\tau_{rad}} = \frac{1}{4n_{SiO_2}} \lceil^r_1 \frac{\tau^r}{\tau^r_{rad}}, \qquad (5.9)$$

where the extraction efficiency has been expressed by equation (5.8). By considering that the radiative lifetime of Er^{3+} in SiO_2 is 15 ms and that the refractive index is about 1.5, and by measuring the overall Er^{3+} lifetime, it is possible to know exactly the number N_1^r at a fixed pumping flux, provided that η_D is known.

Let us consider now the same pumping flux, in such a way that for our $Y_{2-x}Er_xSi_2O_7$ films we can write:

$$I_{PL} = \frac{-}{\tau_{rad}}, \qquad (5.10)$$

being κ = 1, 2 or 3, depending on the Er concentration, according to the quantum cutting effect on the effective excitation cross section. By considering now the ratio between equations (5.9) and (5.10), and by taking into account the expression of the extraction efficiency, we can obtain:

$$\frac{I_{PL}}{I^r_{PL}} = \frac{n^2 \quad \kappa\tau\tau^r_{rad} N_1}{n^{-}_{YSO}\tau^{-}\tau_{rad} N^r_1}, \qquad (5.11)$$

since the detection efficiency is exactly the same, being the experimental conditions the same. Now all the parameters are known (n_{YSO} = 1.9 and τ_{rad} = 8 ms) and we can easily convert the PL intensity into N_1 population. It is important to underline that this method brought to the same result of that obtained by taking the fit parameter B.

The maximum value of N_1/N_{Er} represents the fraction of Er that we managed to put into the first excited level at the highest flux used, that is 7.5×10^{21} photons/($cm^2\cdot s$). The highest fraction (4%) was obtained for the most dilute Er-containing sample.

In the last column of table 5.2 we reported the characteristic upconversion interaction time: this is the product $(C_{up}\cdot N_{Er})^{-1}$, and it represents the typical time of the interaction between Er^{3+} ions in order to start an upconversion mechanism. However basically, the quantum cutting processes described in the previous subsection comes from the same Er-Er interactions of the upconversion ones. Therefore we can consider these times as a rough estimation of more general coupling times. Note that these values are very different and allow us to explain also the efficiency of the quantum cutting as a function of Er, shown in fig. 5.4.

The slowest time is that of $x = 0.03$, and it is about 200 μs, which is much longer than the multiphononic relaxation times of the Er^{3+} levels. This means that the non-radiative multiphononic relaxations win over the quantum cutting processes. Its probability is almost zero, thus demonstrating that in this system only one excitation per photon absorbed is possible. As the Er concentration increases up to $x = 0.65$, the interaction time is about 300 ns and two excitations are possible at 488 nm, since this time is shorter than the multiphononic relaxation of the level $^4S_{3/2}$, but it is longer than that of the level $^4I_{9/2}$. When $x = 2.00$, the interaction time becomes even faster (50 ns), thus allowing a complete quantum cutting process, achieving three excitations at 1.54 μm per each photon absorbed.

Therefore, by using these coupling times, we have demonstrated that it is possible to explain both upconversion and downconversion. These two physical phenomena are deeply related one another, because they involve the very same levels since Er^{3+} ions talk one another in the very same way; the only difference is the pumping flux regime: downconversion is predominant at low fluxes, multiplying the absorption cross section in the first excited state, while upconversion takes place at high fluxes, quickly depleting the first excited state and causing a saturation of the PL intensity versus pump power. The occurrence of both these twin phenomena is more probable and more effective as the Erbium concentration increases, because they are related to the same dipole-dipole interactions, whose strength is proportional to the inverse of the main Er-Er distance [1].

5.4 The effect of Yb sensitization: synthesis and structural properties of $Yb_{2-x}Er_xSi_2O_7$ thin films

As already mentioned in the previous chapter, Yb^{3+} sensitization is very useful in exciting Er^{3+}, because the absorption cross section of Yb^{3+} at 980 nm is one order of magnitude higher than of that of Er^{3+} at the same wavelength [26]. Additionally, Er^{3+} is efficiently sensitized, as a result of the perfect overlap between the multiplets of the two rare earths, as shown in fig. 4.11.

In order to study if there is an effective sensitization of Er^{3+} in a disilicate matrix, we gradually introduced Er^{3+} in an $Yb_2Si_2O_7$ matrix, thanks to the chemical similarities between Er^{3+} and Yb^{3+} ions, which then induce the formation of the very same compounds. The purpose is to understand how strong the effect of Yb^{3+} in the Er^{3+} sensitization is in a mixed Er-Yb compound, which is very different from the most studied Er-Yb doped hosts. In fact, here we explore very high rare earth concentrations and we already demonstrated that in such compounds the rare earth interactions are very strong.

Therefore $Yb_{2-x}Er_xSi_2O_7$ thin films, about 150 nm thick, with different x values were grown by rf co-sputtering from three different targets, SiO_2, Yb_2O_3 and Er_2O_3, on 5 in. (100) c-Si substrates heated up to 400 °C, and rotating at 30 rpm to guarantee a good uniformity of the film thickness. By properly varying the powers applied to the three targets we have synthesized $Yb_{2-x}Er_xSi_2O_7$ thin films, with different compositions, having $0 \leq x \leq 2.00$ [27].

5.4.1 Elemental characterization of the $Yb_{2-x}Er_xSi_2O_7$ films

In order to quantify the elemental composition of the as-grown samples, RBS analyses were performed for all the $Yb_{2-x}Er_xSi_2O_7$ thin films, and some of the spectra are reported in fig. 5.18. The vertical lines in the bottom axis indicate the surface energy edges of O, Si, Er and Yb atoms. Note that the RBS signals are constant, indicating that the chemical composition is uniform throughout the whole film thickness.

The RBS spectrum of the $Yb_2Si_2O_7$, corresponding to $x = 0$, was easily fitted, thus confirming that the concentration ratio [Yb]:[Si]:[O] = 2:2:7. However, in the mixed disilicate $Yb_{2-x}Er_xSi_2O_7$ it is not possible to distinguish between Yb and Er, because the energy difference between their surface edges is lower than the energy resolution of the detector. This is due to the fact these two ions very close in the periodic table. In addition, the backscattering cross section of Er and Yb is almost the same. Therefore only the overall rare earth content, [RE], (where [RE]=[Yb]+[Er]) and then the concentration ratio [RE]:[Si]:[O], can be estimated. We can conclude that all the films have a disilicate composition, although nothing can be said about [Yb] and [Er] separately.

We evaluated the exact composition of the films by performing Particle-Induced X-ray Emission (PIXE) analyses which were realized by using a 2.4 MeV He^+ beam in random configuration as a particle source. A Si pin junction covered by a thin Be window was used as a detector; an Al filter was placed in front of the detector, in order to cut the low energy X-rays originating from the Si substrate.

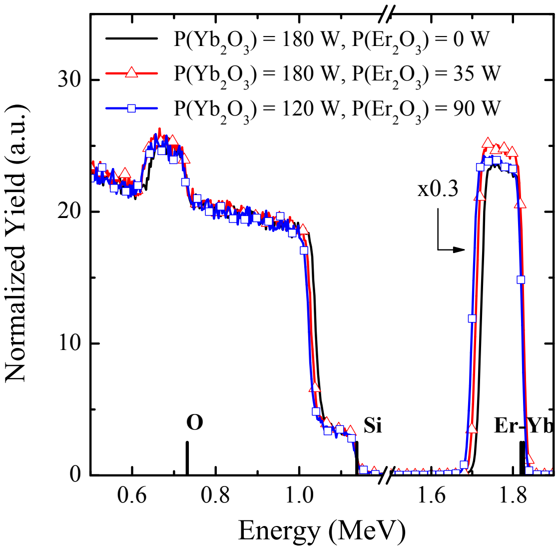

Figure 5.18: RBS spectrum of three different YbErSiO samples, obtained with different sputtering powers applied to the targets. The RE peaks were multiplied by 0.3 in order to compare them with the rest of the spectrum. The edges of O, Si, Er and Yb are indicated: note that the Er and Yb have the same energy edge [27].

Fig. 5.19 reports the PIXE spectra of four disilicate films, two pure reference samples ($Yb_2Si_2O_7$ and $Er_2Si_2O_7$), whose stoichiometry is controlled by RBS measurements, and two mixed $Yb_{2-x}Er_xSi_2O_7$ films obtained for different powers applied to the targets. Several peaks can be observed, corresponding to X-rays emitted from Lα, Lβ, and Lγ transitions of Yb and Er atoms, as labeled in the figure. Note that in the $Yb_2Si_2O_7$ film only the Yb related X-ray peaks are visible (black line). In the mixed disilicate film grown by using a lower $P(Er_2O_3)$ (red line) a small peak around 7 keV appears; it is associated to the L$\alpha_{1,2}$ line of Er; moreover the Yb peaks have the same intensity, since the power applied to the Yb_2O_3 target during the growth was not varied. By further increasing the power applied to the Er_2O_3 target (green line), new peaks related to the Er Lβ and Lγ lines are distinguishable, and at the same time the Yb X-ray peaks decrease, since we reduced the power applied to the Yb_2O_3 target. Finally for Er disilicate, only the Er related X-ray peaks are visible (blue). It is worth noticing that by using this technique, the peaks associated to both Yb and Er are well separated, and then it is possible to analyze them quantitatively.

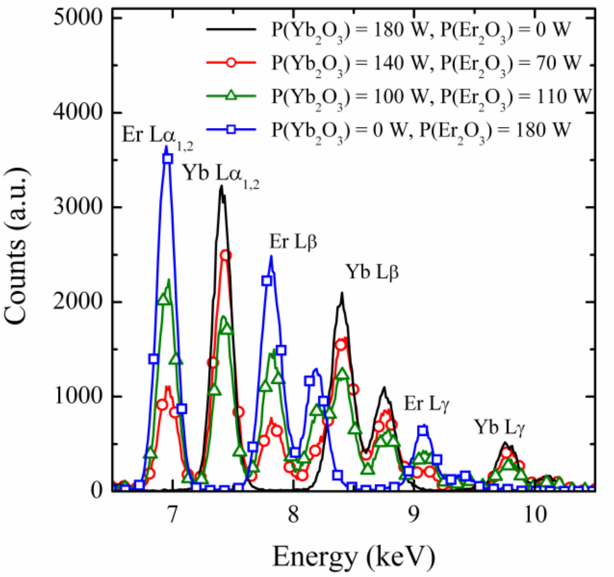

Figure 5.19: PIXE spectra of four $Yb_{2-x}Er_xSi_2O_7$ thin films obtained by varying the power supplies applied to the two RE targets, Yb_2O_3 and Er_2O_3. The X-ray peaks are labeled both for Er and Yb [27].

The quantitative estimation of the single RE concentrations was done by combining RBS and PIXE measurements. In fact, in both kinds of measurement the area of the detected signal (the backscattered He^+ ions and the emitted x-rays, respectively) is directly proportional to the element concentration. As far as RBS is concerned, in fact, the number of detected He^+ ions, which are backscattered from a given species A of atoms is:

$$Y_{RBS}(A) \propto \quad \sigma_R(A), \tag{5.12}$$

being Q the total number of incident He^+ ions, N_A the atomic areal density and $\sigma_R(A)$ the Rutherford backscattering cross-section, related to the atomic species A.

On the other hand in PIXE analyses, the number of X-rays emitted from the same atomic species A is given by:

$$Y_{PIXE}(A) \propto \quad \sigma_I(A) \times \eta_F(A), \tag{5.13}$$

where Q and N_A are again the total number of incident He^+ ions and the atomic areal density respectively, while $\sigma_I(A)$ is the ionization cross section, and $\eta_F(A)$ is the fluorescence yield.

$P(Yb_2O_3)$ [W]	$P(Er_2O_3)$ [W]	PIXE Yb $L\alpha_{1.2}$	PIXE Er $L\alpha_{1.2}$	N_{Yb} [at.%]	N_{Er} [at.%]
180	0	614.46	0	18.0	0
180	15	633.3	6.24	17.8	0.2
180	25	655.19	22.89	17.4	0.6
180	35	672.02	60.14	16.4	1.6
180	45	666.82	104.26	15.3	2.7
160	55	547.95	128.76	14.5	3.5
140	70	506.21	216.45	12.3	5.7
120	90	410.19	302.25	9.8	8.2
100	110	354.81	410.01	7.4	10.6
60	140	173.13	542.27	3.9	14.1
40	160	79.76	630.56	1.5	16.5
0	200	0	696.63	0	18.0

Table 5.3: Summary of all the $Yb_{2-x}Er_xSi_2O_7$ samples: powers applied to the Yb_2O_3 and Er_2O_3 targets, corresponding PIXE area of the $L\alpha_{1,2}$ peaks for Yb and Er (expressed in counts×keV), and calculated atomic concentration of Yb and Er [27].

Therefore we used the two pure disilicates, namely $Yb_2Si_2O_7$ and $Er_2Si_2O_7$, as calibration samples. In fact through RBS analyses it is possible to determine N_{Yb} and N_{Er} for both the two samples, and by comparing them with the respective PIXE signal, it is possible to find a parameter that directly correlates the surface areal density to the area under the $L\alpha_{1,2}$ peak of Yb and Er, (3.26×10^{-3} and 3.44×10^{-3} $cm^{-2}keV^{-1}$ for Yb and Er respectively). We chose the $L\alpha_{1,2}$ peaks in order to have the best resolution, because of their higher intensity with respect to the other peaks.

Now that we have the calibration parameters, by measuring the area of the $L\alpha_{1,2}$ peaks corresponding to the of Er and Yb in all the as-deposited $Yb_{2-x}Er_xSi_2O_7$ samples, we can directly extract both N_{Yb} and N_{Er} values, known the total RE areal density by RBS spectra and under the reasonable assumption that both σ_I and η_F do not depend on the film composition. This is a reasonable assumption since the ionization process induced by an ion strike is an atomic process, which does not involve the material structure in which the atom is embedded and the X-ray absorption of the materials can be considered unchanged by going from $Yb_2Si_2O_7$ to $Er_2Si_2O_7$.

All the data are resumed in table 5.3, where the area of the $L\alpha_{1,2}$ peaks and the atomic concentrations of the two rare earths are listed together with the powers applied to Yb_2O_3 and Er_2O_3 targets during the growth by sputtering. In particular, the atomic concentrations were obtained by considering the total atomic density estimated by RBS measurements [27].

Note that in all the as-grown samples the total concentration [Yb]+[Er] is 18 at.%. Moreover [Si] and [O] were found to be 18 at.% and 64 at.% respectively. Therefore we can conclude that all the as-grown films have a disilicate composition, and that it was possible to determine the Er concentration (and the Yb one accordingly) in a very wide range, spanning over three decades, with a minimum [Er] value of 0.2 at.% (corresponding to 5×10^{20} at/cm^3).

5.4.2 Crystallization properties of $Yb_{2-x}Er_xSi_2O_7$ thin films

Also in the case of this new series of disilicate samples, as we did for $Y_{2-x}Er_xSi_2O_7$ described in the previous sections of this chapter, the films were treated at 1200 °C for 30s in O_2 ambient in a rapid thermal annealing (RTA) system, in order to induce the crystallization in the α-phase.

We performed XRD measurements on the annealed films. As already demonstrated for $Er_2Si_2O_7$ [28] and for $Y_{2-x}Er_xSi_2O_7$ (see previous sections of this chapter), where Er^{3+} can gradually substitute the Y^{3+} ions in the same crystalline structure, given the similarity of the chemical properties of Y^{3+} and Er^{3+} ions and of their ionic radii; in the same way here Er^{3+} can substitute Yb^{3+} ions in the same crystalline environment of $Yb_2Si_2O_7$.

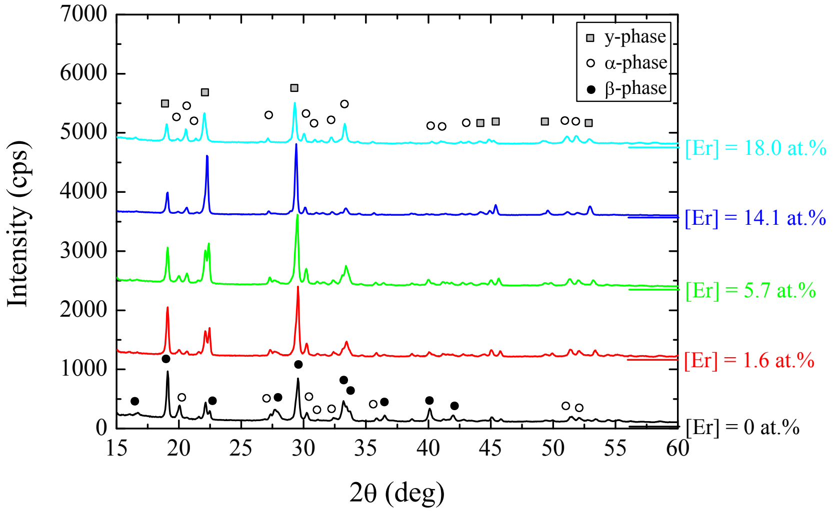

Figure 5.20: X-ray diffraction spectra of $Yb_{2-x}Er_xSi_2O_7$ films grown on Silicon, after 1200 °C, 30 s, O_2 for five different Er concentrations. The peaks associated to three different polymorphs are indicated as grey squares (y-Er disilicate), open circles (α-Yb disilicate) and full circles (β-Yb disilicate).

According to ref. [3, 4], Ytterbium silicate crystallizes in the β phase up to 1700 °C, since its ionic radius (0.86 Å) is smaller than that of Er^{3+} (0.88 Å) or Y^{3+} (0.89 Å). For Er^{3+}, on the contrary, at 1200 °C, y and α phases are registered and their occurrence in our disilicates is demonstrated in fig. 5.2. The XRD measurements are reported for five samples with different Er concentrations in fig. 5.20. We can immediately see that after the annealing the sample without Er (i.e. the $Yb_2Si_2O_7$ sample) crystallize in a mixture of α [29] and β phases [30]. Note that the monoclinic y phase of

$Yb_2Si_2O_7$ does not exist in literature. As Erbium is gradually introduced in the films, we observed that the α phase-related peaks are still there, while the β phase gradually disappears and it is substituted by y-phase of $Er_2Si_2O_7$, which is easier to be formed in our sputtered Er-based silicate films. In fact, for the sputtered Er disilicate the β phase is formed at higher temperatures (1300 °C).

Apart from this aspect, it is worth reminding that we are interested in the triclinic α phase, which is known to be the most efficient from the optical point of view. As far as this phase is concerned, given the similarities between the two triclinic polymorphs α-$Er_2Si_2O_7$ [28] and α-$Yb_2Si_2O_7$ [29], we can insert gradually Er^{3+} ions in substitution of the Yb^{3+} ones in the α-disilicate compounds. Therefore, in the next section we are going to discuss the optical properties of α-$Yb_{2-x}Er_xSi_2O_7$, and we will refer to the photoluminescence of Er and Yb only in this particular crystalline environment.

5.5 Optical properties of $Yb_{2-x}Er_xSi_2O_7$ thin films

The optical emission from α-$Yb_{2-x}Er_xSi_2O_7$ films was investigated by performing photoluminescence measurements at room temperature. In order to deeply study the excitation mechanisms of Er^{3+} through Yb^{3+} ions, we compared the excitation in presence and in absence of Yb^{3+}. In fig. 5.21 we report the photoluminence excitation spectroscopy (PLE). These measurements were performed by using a Ti:sapphire laser, tunable in a very wide range of wavelengths, between 700 and 1000 nm [27].

By resonantly exciting Erbium at 980 nm, we analyzed one of the α-$Y_{2-x}Er_xSi_2O_7$ films already described in section 5.1. In particular we considered the film with [Er] = 4.2 at.%. The PL emission has a peak at 1.54 μm, typical of Er emission in α-crystalline phase, as shown in fig. 5.21(a). The PL shape is the verysame of the spectra obtained for all the $Y_{2-x}Er_xSi_2O_7$ films at λ_{exc} = 488 nm (fig. 5.8). By varying the excitation wavelength between 750 nm and 1000 nm, the PLE spectrum for this sample, recorded at 1.54 μm, is characterized by two sharp peaks centered respectively at 800 nm and at 980 nm. These two peaks correspond respectively to the well

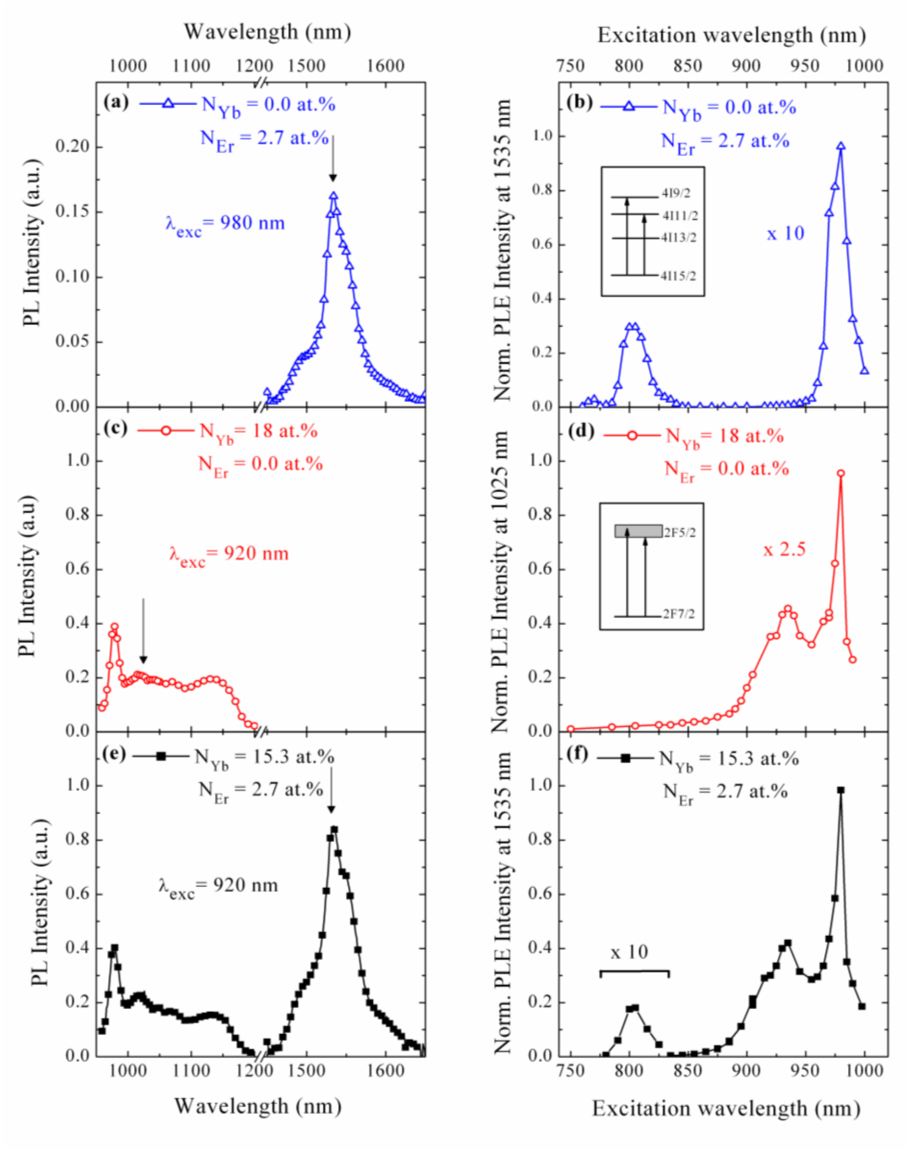

Figure 5.21: PL spectra (a) from α-$Y_{2-x}Er_xSi_2O_7$ at 980 nm, (c) from α-$Yb_2Si_2O_7$ and (e) from α-$Yb_{2-x}Er_xSi_2O_7$ at 920 nm. PLE spectra (b, d and f panels respectively) at 1.54 μm from the same samples. The inserts report the levels schemes of the Er and Yb ions [27].

known $^4I_{15/2}\rightarrow^4I_{9/2}$ and $^4I_{15/2}\rightarrow^4I_{11/2}$ Er^{3+} transitions, as depicted in fig. 5.21(b). In fact, Y^{3+} ions are optically inactive and do not participate in the excitation mechanism for Er^{3+}. Therefore in these first two panels we can observe the typical behavior of Er^{3+} inserted in a solid host: here Er can be excited just by a direct excitation from the incoming photons.

A different behavior is observed for α-$Yb_2Si_2O_7$ (N_{Yb}= 18 at.%), as shown in fig. 5.21 (c) and (d). The PL emission at λ_{exc}= 920 nm is reported in the former panel. It is possible to observe that this emission from Yb^{3+} is the typical broad band shape between 900 and 1100 nm associated to the $^2F_{5/2}\rightarrow^2F_{7/2}$ Yb^{3+} de-excitation, with a further band between 1100-1200 nm due to the band edge recombination of carriers in Si. Also for this sample we measured the PLE spectrum by recording the PL intensity at 1025 nm as a function of λ_{exc}. It is worth noticing that there is a main peak at 980 nm and another band around 920 nm, both associated to the $^2F_{7/2}\rightarrow^2F_{5/2}$ transitions of Yb ions typically observed in several other matrices [31-37].

After these two reference samples we can analyze an $Yb_{2-x}Er_xSi_2O_7$ sample, with [Er] = 2.7 at.%. By exciting it at λ_{exc}= 920 nm, that is not resonant with any Er^{3+} transitions, the PL spectrum shows not only the Yb^{3+} emission between 900-1200 nm but also the typical peak of Er^{3+} at 1.54 μm, as reported in fig. 5.21 (e). This is a strong evidence that Er^{3+} can be excited in this matrix by mediated excitation from Yb^{3+} ions, thanks to the good matching existing between the Yb^{3+} $^2F_{5/2}$ level and the Er^{3+} $^4I_{11/2}$ one [35, 36]. We then performed the PLE spectroscopy, by looking at 1.54 μm and by exciting again from 750 nm to 1000 nm as it is shown in fig. 5.21(f). Note that the shape of this spectrum is a superposition of the two PLE spectra already described for Er^{3+} in α-Y_{2-x}-$Er_xSi_2O_7$ and Yb^{3+} in α-$Yb_2Si_2O_7$. We can then conclude that Er^{3+} in α-$Yb_{2-x}Er_xSi_2O_7$ can be excited in two different and independent ways: one is the direct absorption of an incoming photon, and the other one is the mediated excitation from Ytterbium, that gathers the incoming photons and then transfers this energy to Erbium.

Another interesting point regards the PL intensities at 1.54 μm by exciting at λ_{exc}= 800 nm: for the samples in panels (b) and (f) PL scales with the Er concentration. This is not true at λ_{exc}= 980 nm. In fact, for α-$Yb_{2-x}Er_xSi_2O_7$, the PL intensity at 1.54 μm is surprisingly one order of magnitude higher with respect to the case in which Yb^{3+} is not present. The reason lies in the superposition of the two contributions, the direct Er^{3+} excitation and the mediated excitation from Yb^{3+} ions [27].

5.6 Er sensitization by Yb ions

We have just demonstrated that in the $Yb_{2-x}Er_xSi_2O_7$ samples there is a noticeable effect of Yb^{3+} in the Er^{3+} excitation process. This is due to the higher absorption cross section and to the resonant energy transfer between the two rare earths. In this section we address this subject from a quantitative point of view. In particular we try to understand how strong the mediated contribution in the Er^{3+} excitation is. Moreover, the trade-off between Er concentration and lifetime is found, by looking at the photoluminescence properties of Er^{3+} in $Yb_{2-x}Er_xSi_2O_7$ films. Finally a comparison between the silicates in presence and in absence of Yb^{3+} is done.

5.6.1 Sensitization of Er^{3+} through Yb^{3+} ions: energy transfer between the two rare earths

In order to quantify the sensitization efficiency, we performed PLE spectroscopy for all the $Y_{2-x}Er_xSi_2O_7$ films as a function of x, by looking the emission of Er^{3+} at 1.54 μm. In all the cases, the PLE shape is the same and in particular we found a relevant mediated contribution of Yb^{3+} in the Er^{3+} excitation mechanism (i.e by exciting at a wavelength not resonant with the Er levels). This demonstrates that the energy transfer between Yb and Er is very strong in all the films [27].

We observed that by increasing the Yb concentration, the PL intensity observed by exciting at 935 nm, i.e. under pure mediated excitation condition, increases with respect to the PL intensity measured by exciting Er^{3+} at 980 nm, i.e. in presence of both the direct and the mediated excitations. The ratio of the PL intensity at 1.54 μm recorded at 935 nm and at 980 nm then gives important information about excitation. For pure resonant excitation this ratio is zero, while for pure mediated excitation this ratio is 0.45, as can be deduced from fig. 5.21 (d) for $Yb_2Si_2O_7$, which is a sample where no transfer can take place, since there is not any Er^{3+} ion.

The ratio PL(λ_{exc} = 935 nm)/ PL(λ_{exc} = 980 nm) is reported in fig. 5.22 as a function of the Yb content N_{Yb} (lower axis) or of the Er content N_{Er} (upper axis). Note that the ratio increases by increasing Yb and it reaches its maximum value for $N_{Yb} \geq 10.0$ at.%, corresponding to $N_{Er} \leq 8.0$ at.%. This is a regime in which the Yb^{3+} ions are present in a number that overcomes the Er^{3+} ions in the films. This maximum value (0.45) is exactly the same value of the ratio PL(λ_{exc} = 935 nm)/ PL(λ_{exc} = 980 nm) recorded at 1025 nm for just Yb^{3+} ions in $Yb_2Si_2O_7$. This value is characteristic of Yb and it comes from the dependence of the Yb absorption cross section on the excitation wavelength. By normalizing the ratio to the maximum value, we obtain the percentage of the mediated contribution at 980 nm, as reported in the right axis of the graph. Therefore, for $N_{Yb} \geq 10.0$ at.%, Er^{3+} ions are efficiently sensitized, and their excitation is totally due to mediated energy transfer from Yb^{3+} ions [27].

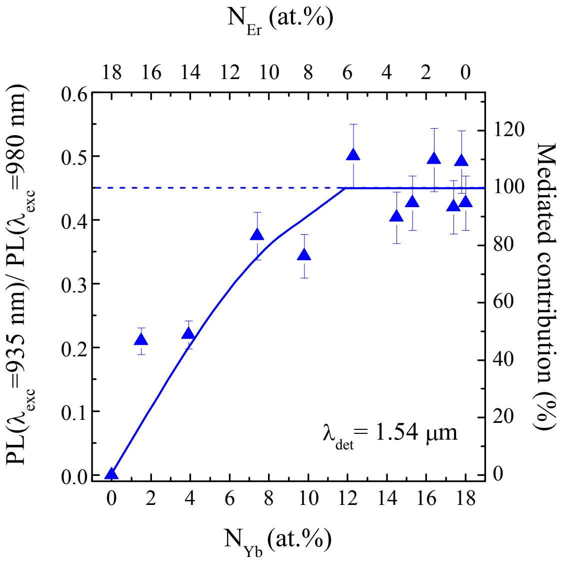

Figure 5.22: Ratio PL(λ_{exc}=935 nm)/ PL(λ_{exc}=980 nm) measured at 1.54 µm, as a function of N_{Yb} (lower axis) and N_{Er} (upper axis). This ratio, normalized by its maximum value, represents the mediated contribution in the Er^{3+} excitation (right axis) [27].

In order to have quantitative information about this energy transfer we analyzed the decay rate of Yb^{3+} in presence and in absence of Er^{3+}. In fact it is expected that the intrinsic Yb^{3+} decay rate W_{Yb} is modified by the presence of Er^{3+} (becoming $W_{Yb\text{-}Er}$), being this rare earth a non-radiative channel for the Yb^{3+} decay, according to the following equation:

$$W_{Yb\text{-}Er} = \quad + \qquad (5.14)$$

where C_{ET} is the Yb-Er energy transfer coefficient. It is a coefficient which represents the strength of the communication between the two rare earths. The higher is C_{ET}, the faster is the new decay of Yb^{3+} in presence of a certain amount of Er^{3+}.

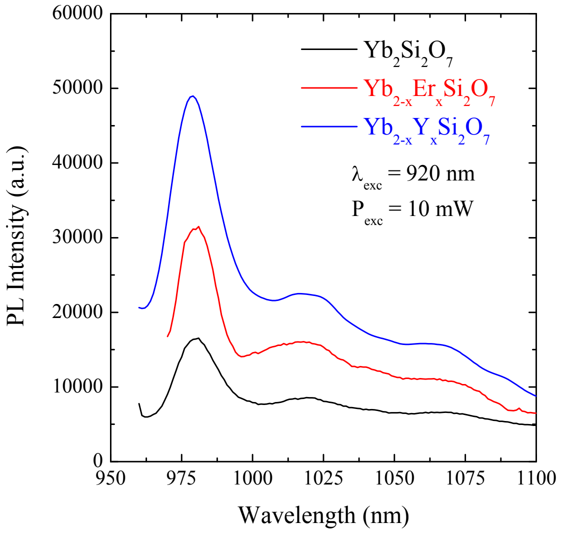

Figure 5.23: PL spectra of Yb^{3+} from α-Yb disilicate, α-Yb-Er mixed disilicate and from α-Yb-Y mixed disilicate, obtained by pumping at 920 nm.

In order to find properly C_{ET} for our $Yb_{2-x}Er_xSi_2O_7$ films, we had to synthesize properly $Yb_{2-x}Y_xSi_2O_7$ films in which Yb is embedded in the very same compound, but it is not in presence of Er. Therefore we used the known similarities of the rare earths and Y^{3+} and the optical inactivity of Y^{3+} to analyze the intrinsic decay rate of Yb in absence of Er. We synthesized these samples by substituting the Er_2O_3 target with the Y_2O_3 one. These reference samples were demonstrated to be perfectly stoichiometric (not shown) and after 1200 °C, 30s, O_2, crystallized in a mixture of α and β phases (not shown), as it was observed for $Yb_{2-x}Er_xSi_2O_7$ compounds. The

PL spectra of these samples were the typical of the α phase: the shape is compared in fig. 5.23.

The reference samples' lifetimes are also useful for the transfer efficiency, defined as:

$$\eta = \; - \; \frac{W}{W_{\text{Yb-Er}}} \tag{5.15}$$

since it comes from the fact that, in a particular matrix, given a certain number of non radiative decay paths due to the defects, the Yb^{3+} decay rate is modified when Er^{3+} is inserted. If the lifetime of Yb^{3+} in presence of Er^{3+} tends to zero, it means that there is a very efficient energy transfer and η tends to 1, i.e. 100%. On the other side, if the Yb^{3+} ions are insensitive when Er^{3+} is inserted, i.e. their lifetime is the same, there is no energy transfer and η is zero.

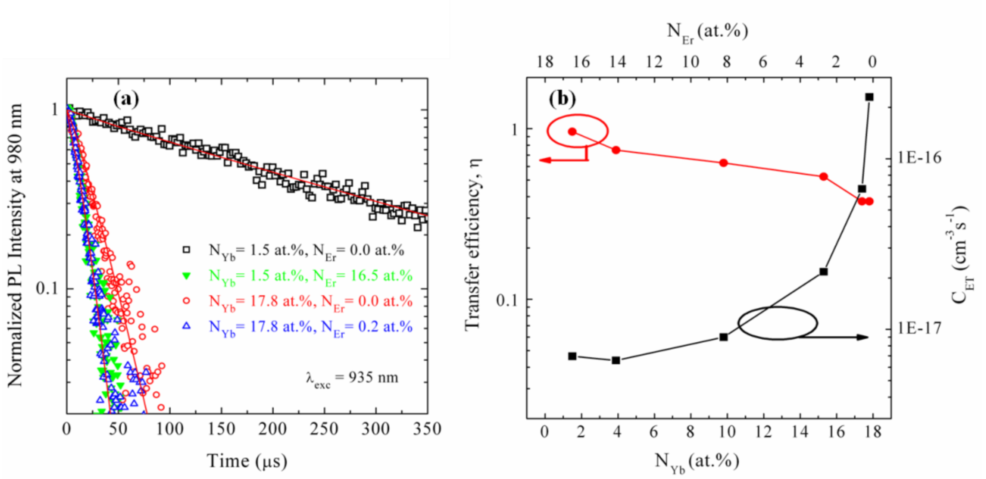

Figure 5.24: (a) PL intensity decay recorded at 980 nm for N_{Yb}= 1.5 at.% and N_{Yb}= 17.8 at.% in absence and in presence of Er (i.e. in $Yb_{2-x}Y_xSi_2O_7$ and $Yb_{2-x}Er_xSi_2O_7$ respectively). Continuous lines are the single exponential fits of the experimental data. (b) Transfer efficiency and C_{ET} coefficient calculated according to equations (5.14) and (5.15) respectively as a function of N_{Yb} (lower axis) and N_{Er} (upper axis) [27].

We measured the lifetimes of Yb^{3+} at 980 nm, by pumping at 935 nm the $Yb_{2-x}Er_xSi_2O_7$ samples and we found that for each value of N_{Yb} the decay rate is $W_{Yb\text{-}Er} = 0.1\ \mu s^{-1}$, which is much faster than the typical radiative decay time of Yb^{3+} (0.7 ms^{-1}) [26]. We measured W_{Yb} by using the $Yb_{2-x}Y_xSi_2O_7$ and we found the typical concentration quenching phenomenon: in fact by increasing N_{Yb} from 1.5 at.% to 9.8 at.%, W_{Yb} increases from 3.9 ms^{-1} to 37 ms^{-1} and it reaches 62 ms^{-1} for N_{Yb} = 17.8 at.%. For all the samples, these values are smaller than $W_{Yb\text{-}Er}$, thus confirming that Er^{3+} is a competitive non-radiative channel in the Yb^{3+} decay whole mechanism. This can be observed by looking at the decay curves reported in fig. 5.24 (a) for two values of N_{Yb} (in absence and in presence of Er). By using all the data extrapolated from the fits we can now calculate both C_{ET} and η, and they are plotted in fig. 5.24 (b) [27].

It is worth noticing that the trend of the transfer coefficient has a slight increase at the beginning; then when N_{Yb} becomes higher than 10.0 at.%, the increase has a very high slope. The maximum value is reached for N_{Yb} = 17.8 at.% (2×10^{16} $cm^{-3}s^{-1}$). This means that when the Yb concentration overcomes the Er ones (i.e. after the threshold of 10.0 at.%), each single Er^{3+} ion feels a stronger and stronger coupling with the Yb^{3+} donors. In fact, by increasing N_{Yb}, and by simultaneously decreasing N_{Er}, the number of donors per acceptor is larger and larger. At N_{Yb} = 17.8 at.%, each Er^{3+} ion present in the film is completely surrounded by Yb^{3+} ions, and therefore the strength of the coupling is very high. The maximum C_{ET} value is comparable with the best coupling coefficient reported in literature for Er-Yb codoping in many hosts, like phosphate glasses, containing usually about 10^{19} Er/cm^3 and 10^{20} Yb/cm^3 [38]. Note that these concentrations are about one order of magnitude lower than those of our mixed disilicate films. Therefore the Er excitation through Yb^{3+} sensitizers is very efficient also in the compound regime of rare earth concentrations (i.e. ~10^{21} RE/cm^3) [27].

5.6.2 Efficient Er PL emission in $Yb_{2-x}Er_xSi_2O_7$ films

In order to study the PL emission of Er in this particular system, we have measured the PL intensity at 1.54 μm and the characteristic decay time from the Er^{3+} $^4I_{13/2}$ level, as a function of N_{Yb}, and consequently of N_{Er}. These measurements were done by exciting the system at 980 nm and are resumed in fig. 5.25. The lifetimes were evaluated by fitting the decay with a single exponential function and they are reported in the right hand axis of the figure. It is evident that by increasing Erbium, its lifetime in $Yb_{2-x}Er_xSi_2O_7$ decreases from 5.3 ms to 270 μs. Note that the trend of the lifetime is exactly the same than that of Erbium in $Y_{2-x}Er_xSi_2O_7$. Since these two hosts can be considered exactly the same from the structural point of view, this means that the Erbium lifetime in a disilicate host depends just on the Er-Er interactions. The only mechanism that modifies the Erbium lifetime is the concentration quenching: by increasing N_{Yb}, the deleterious Er-Er interactions are reduced, and hence the lifetime is increased. This means also that in the Ytterbium disilicate, Er de-excitation is not affected by the presence of the Ytterbium ions. This is also an indirect demonstration that the back-transfer from Er^{3+} to Yb^{3+} is negligible, whatever is the Erbium concentration.

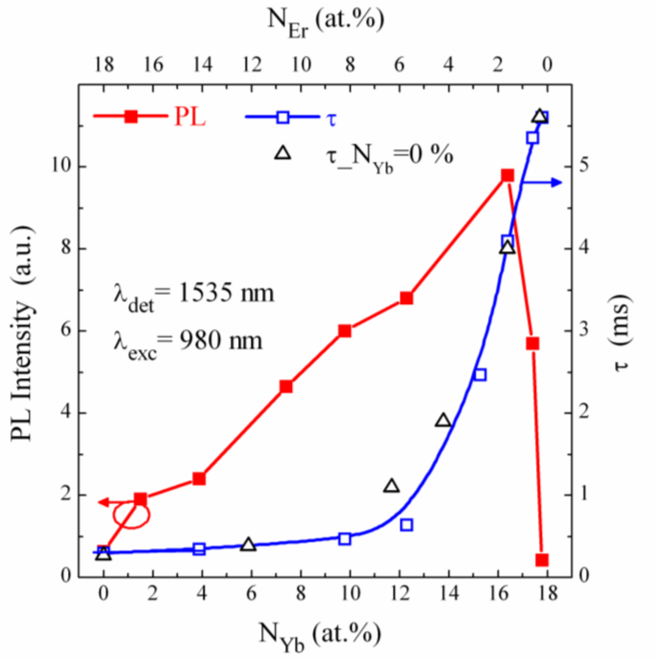

Figure 5.25: PL intensity from Er^{3+} $^4I_{13/2}$ level at 1.54 μm (red full squares) and Er^{3+} decay time from the same level (blue open squares) for $Yb_{2-x}Er_xSi_2O_7$ as a function of the two rare earths, by exciting at 980 nm. The lifetimes measured in the $Y_{2-x}Er_xSi_2O_7$ film are reported as a reference set (black open triangles) [27].

As far as the PL intensity is concerned, it is worth reminding that in the case of $Er_2Si_2O_7$ (N_{Yb} = 0 at.%) a very strong signal has been already demonstrated [5], since in that case all the Er^{3+} ions are optically active. However by introducing just 1.5 at.% of Yb^{3+} ions, hence reducing by the same quantity the N_{Er}, the PL intensity increases by a factor three, with a similar decay rate. This is due to the benefic effect of the sensitization of Yb^{3+} ions.

Moreover, by further increasing the Yb content in the film and further reducing the Er content, the PL intensity keeps growing up, and this trend cannot be justified only by the increase of the Er lifetime. This is mainly due to the increase of the mediated contribution in the Er excitation at 980 nm, already observed in fig. 5.22.

When N_{Yb} becomes higher than 10 at.%, i.e. when the maximum mediated contribution is reached, the PL intensity is still increasing, but it reaches the highest intensity for N_{Er} = 1.6 at.% and N_{Yb} = 16.4 at.%. This further increase is justified by the steep increase of the Er lifetime. This concentration represents the best compromise between the lifetime and the number of emitting centers. In fact, by increasing further N_{Yb}, though there is 100 % of mediated contribution in the Er excitation and the maximum C_{ET} is found, the number of Er^{3+} ions available for the excitation is too low, and the overall Er^{3+} emission at 1.54 μm drops quickly down [27].

5.6.3 Comparison between the two rare earth silicates for optical amplifiers

We have observed that the sputtered $Yb_{2-x}Er_xSi_2O_7$ films are characterized by a very intense PL signal. Particularly, despite we did not make a direct comparison yet, we have registered that this PL signal is always more intense than that of $Er_2Si_2O_7$, whose signal is more intense than all the $Y_{2-x}Er_xSi_2O_7$ films, as reported in fig. 5.8. This is another demonstration of the benefic existence of Yb-Er energy transfer, for the Erbium excitation.

In this subsection we analyze the trend of the PL intensity as a function of the pumping flux φ, in the range between 10^{18} and 10^{22} photons/($cm^2 \cdot s$) for both Y-Er and Yb-Er mixed disilicates. The sample under investigation is the best one from the optical point of view, the one with N_{Er} = 1.6 at.%. A comparison between this sample and a twin one with the same Erbium concentration, but with Y instead of Yb, is reported in fig. 5.26.

In both cases the PL trend is very similar: in fact there is a linear increase at low pumping fluxes, while at high pumping fluxes there is a sublinear increase, associated with the occurrence of upconversion, since there is a high probability to have two Er^{3+} ions both excited and very close one another. The curves can be fitted by using equation (5.7), in order to find the upconversion coefficient C_{up} and the excitation cross section. Moreover, as already described in section 5.3, it is possible to properly calibrate and correlate the scale in PL to a scale in an absolute Er population in the first excited state.

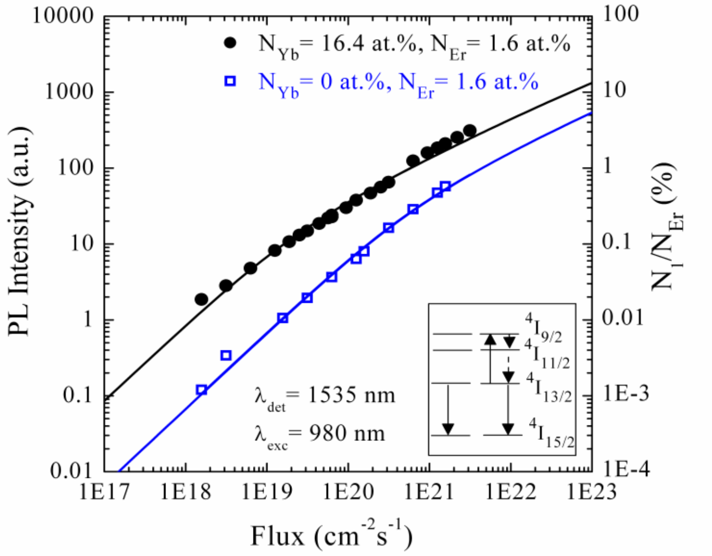

Figure 5.26: PL intensity at 1535 nm as a function of pump photon flux φ for $Yb_{2-x}Er_xSi_2O_7$ and $Yb_{2-x}Er_xSi_2O_7$ having the same N_{Er}. The excitation wavelength is λ_{exc}= 980 nm. The continuous curves are fits of the experimental data, obtained by using Eq. (5). A scheme of the up-conversion phenomenon is depicted on the right-hand corner [27].

We obtained a value of 2.0×10^{-21} cm^2 in $Y_{2-x}Er_xSi_2O_7$, corresponding to the typical absorption cross section of Er ions at 980 nm, as observed in silica glasses [14], and 2.0×10^{-20} cm^2 in $Yb_{2-x}Er_xSi_2O_7$. This is a further confirmation that in the Yb-Er mixed compound Erbium is efficiently excited by energy transfer from Yb^{3+} ions, because the excitation cross section is one order of magnitude higher than in the case of Y-Er mixed compounds, with almost the same Er concentration [27]. Note that this excitation cross section is the same measured in $Yb_2Si_2O_7$ (not shown) and also reported in literature [26].

As far as the C_{up} estimation is concerned, in the two cases we obtained the same value of about 6×10^{-17} cm^3/s. This is another proof that, as demonstrated to be for concentration quenching, the upconversion-like interactions between the Er^{3+} ions in the first excited state are not influenced by the presence of Yb^{3+} ions.

Despite this C_{up} is three times higher than that obtained for the best case of $Y_{2-x}Er_xSi_2O_7$ sample (see table 5.2), it is worth noticing that, thanks to Yb^{3+}, about 20% of Er^{3+} ions can be excited at the first excited level at a flux of 10^{23} photons/cm^2·s, more than one order of magnitude with respect to the twin sample with Y^{3+} instead of Yb^{3+}. Moreover this inverted population (20%) is about five times higher than that of the best $Y_{2-x}Er_xSi_2O_7$ sample (4%), as reported in table 5.2, thus demonstrating that Yb-Er mixed silicate is a very promising material for optical amplifiers at 1.54 μm [27].

Conclusions

In this chapter we have demonstrated that it is possible to efficiently synthesize Y-Er and Yb-Er mixed disilicate thin films, thanks to the versatility of the sputtering deposition technique. In these systems, Er concentration was varied in a two orders of magnitude range, between the classical doping regime (~10^{20} Er/cm^3) and the compound regime (~10^{22} Er/cm^3). We have shown that the stoichiometry of such silicates is exactly the disilicate one, RE:Si:O = 2:2:7, by performing RBS analyses. This experimental technique allows also to estimate the atomic concentrations of all the elements. However in the case of Yb-Er disilicate, also PIXE analyses were necessary in order to distinguish between the two rare earths. All the films crystallize after thermal annealing and their crystallization was investigated through XRD measurements, demonstrating that in all the cases α-phase can be formed.

By analyzing the optical properties of Er in α-$Y_{2-x}Er_xSi_2O_7$ disilicate, we observed that it is characterized by intense photoluminescence at 1.54 μm. We have demonstrated that by exciting Er at two different wavelengths (488 nm and 380 nm), at low pumping fluxes, the interesting phenomenon of quantum cutting occurs. Its effect is detectable by looking at the effective excitation cross section. In fact, by increasing Er concentration, i.e. by increasing the probability of Er-Er interaction, different cross-relaxations occur and can distribute the energy of the incoming photon, by exciting one, two or even three and four Er ions. Efficiencies of this mechanism as high as 300% (488 nm) and 370% (380 nm) were registered for the sample with the highest Er content, in which the mean distance Er-Er is the minimum possible. These efficiencies are the highest ever observed for this particular quantum cutting and actually imply that this material is very promising as converter for Ge solar cells.

Moreover we demonstrated that quantum cutting has the same physical root of upconversion, being these two phenomena deeply related to the very same cross-relaxations involving Er levels.

On the other hand, Yb-Er disilicate compound was studied in order to understand whether it is possible to more effectively excite Er, by exploiting the well-known properties of Yb sensitization. We investigated the coupling between the two RE ions for an extended range of concentrations, by keeping fixed $N_{Er}+N_{Yb}$= 18 at.%. In all the cases Yb^{3+} ions can efficiently transfer energy to Er^{3+}. We calculated the physical parameters describing the energy transfer, and we found an energy transfer coefficient as high as 2×10^{-16} $cm^{-3}s^{-1}$, comparable to the best coupling coefficient reported in literature in phosphate glasses containing typically about 10^{19} Er/cm^3 and 10^{20} Yb/cm^3. Therefore we demonstrated that Er sensitization through Yb is still efficient in Yb-Er disilicate, even by increasing the RE concentrations up to one order of magnitude. We analyzed the PL emission at 1.54 μm and the best compromise between Er population and lifetime was found for 1.6 at.% of Er.

We finally compared the PL emission as a function of pump power from two samples of Yb-Er and Y-Er silicates with the very same Er content and we found that a much higher excited population (about 20%) at $^4I_{13/2}$ level was registered in presence of Yb. In this case the excitation cross section was one order of magnitude higher, due to the Yb sensitization. Despite the same upconversion coefficient (6×10^{-17} cm^3/s), therefore, the presence of Yb has a positive effect for Erbium making Yb-Er disilicate very promising as active medium for optical amplifiers at 1.54 μm.

References

[1] M. Miritello, R. Lo Savio, P. Cardile and F. Priolo, Phys. Rev. B **81**, 041411R (2010).

[2] N. A. Toropov, F. Y. Galakhov and S. F. Konovalova, Bull. Aca. Sci. USSR Div. Chem. Sci. (Eng. Transl.) **8**, 1271 (1961).

[3] J. Ito and H. Johnson, Am. Miner. **53**, 1940 (1968).

[4] J. Felsche, J. Less-Common Metals **21**, 1 (1970).

[5] M. Miritello, R. Lo Savio, F. Iacona, G. Franzò, A. Irrera, A. M. Piro, C. Bongiorno and F. Priolo, Adv. Mater. **19**, 1582 (2007).

[6] JCPDS database, powder diffraction file no. 74-1994.

[7] JCPDS database, powder diffraction file no. 38-0223.

[8] JCPDS database, powder diffraction file no. 38-0440; K. Liddell and D. Thompson, Trans. J. Br. Ceram. Soc. **85**, 17 (1986).

[9] A. I. Becerro and E. Escudero, Phase Transit. **77**, 1093 (2004).

[10] A. Polman, J. Appl. Phys. **82**, 1 (1997).

[11] K. Suh, J. H. Shin, S.-J. Seo and B.-S. Bae, Appl. Phys. Lett. **92**, 121910 (2008).

[12] C. Li, C. Wyon and R. Moncorgé, IEEE J. Quantum Electron. **28**, 1209 (1992).

[13] T. Schweizer, T. Jensen, E. Heumann and G. Huber, Opt. Comm. **118**, 557 (1995).

[14] W. J. Miniscalco, J. Lightwave Technol. **9**, 234 (1991).

[15] B. S. Richards, Sol. Energy Mater. Sol. Cells **90**, 1189 (2006).

[16] W. Shockley and H. J. Queisser, J. Appl. Phys. **32**, 510 (1961).

[17] T. Trupke, M. A. Green and P. Würfel, J. Appl. Phys. **92**, 1668 (2002).

[18] W. W. Piper, J. A. De Luca and F. S. Ham, J. Lumin. **8**, 344 (1974).

[19] R. T. Wegh, H. Donker, K. D. Oskam and A. Meijerink, Science **283**, 663 (1999).

[20] L. Xie, Y. Wang and H. Zhang, Appl. Phys. Lett. **94**, 061905 (2009).

[21] C. Kittel, *Introduction to Solid State Physics*, John Wiley and Sons, New York, 1996.

[22] M. Federighi and F. Di Pasquale, IEEE Phot. Technol. Lett. **7**, 303 (1995).

[23] G. N. van den Hoven, E. Snoeks, A. Polman, C. van Dam, J. W. M. van Uffelen and M. K. Smit, J. Appl. Phys. **79**, 1258 (1996).

[24] A. Przhevuskii and N. Nikonorov, Opt. Mater. **21**, 729 (2003).

[25] N. Nikonorov, A. Przhevuskii and A. Chukharev, J. Non-Cryst. Solids **324**, 92 (2003).

[26] X. Zou and H. Toratani, Phys. Rev. B **52**, 15889 (1995).

[27] M. Miritello, P. Cardile, R. Lo Savio and F. Priolo, Opt. Expr. 19, 20761 (2011).

[286] R. Lo Savio, M. Miritello, A. M. Piro, F. Priolo and F. Iacona, Appl. Phys. Lett. **93**, 021919 (2008).

[29] JCPDS database, powder diffraction file no. 30-1439; G. Bocquillon, et al., C. R. Seances Acad. Sci., Ser. B **283**, 343 (1976).

[30] JCPDS database, powder diffraction file no. 72-0649.

[31] J. K. Sahu, Y. Jeong, D. J. Richardson and J. Nilsson, Opt. Commun. **227**, 159 (2003).

[32] G. C. Valley, Opt. Fiber Technol. **7**, 21 (2001)

[33] G. G. Vienne, J. E. Caplen, L. Dong, J. D. Minnely, J. Nilsson and D. N. Payne, J. Lightwave Technol. **16**, 1990 (1998).

[34] H. S. Hsu, C. Cai and A. M. Armani, Opt. Expr. **17**, 23266 (2009).

[35] C. Strohhöfer and A. Polman, Opt. Mater. **21**, 705 (2003).

[36] C. Strohhöfer and A. Polman, J. Appl. Phys. **90**, 4314 (2001).

[37] W. G. Quirino, M. J. V. Bell, S. L. Oliveira and L. A. O. Nunes, J. Non-Cryst. Solids **351**, 2042 (2005).

[38] B. C. Hwang, S. Jiang, T. Luo, J. Watson, G. Sorbello and N. Peyghambarian, J. Opt. Soc. Am. B **17**, 833 (2000).

List of Publications

This thesis is based on the following publications:

- *Laser-like room temperature electroluminescence from Silicon at telecommunication wavelengths*
  A. Shakoor, **P. Cardile**, S. Portalupi, R. Lo Savio, M. Galli, G. Franzò, D. Gerace, S. Boninelli, C. Spinella, F. Priolo, L. O'Faolain, L. C. Andreani and T. F. Krauss.
  (Submitted)

- *Electrical conduction and optical properties of doped Silicon-on-Insulator Photonic crystals.*
  P. Cardile, G. Franzò, R. Lo Savio, M. Galli, T. F. Krauss, F. Priolo and L. O'Faolain.
  Applied Physics Letters **98**, 203506 (2011)

- *Energy transfer and enhanced 1.54 μm emission in Erbium-Ytterbium disilicate thin films.*
  M. Miritello, **P. Cardile**, R. Lo Savio and F. Priolo.
  Optics Express **19**, 20761 (2011)

- *Enhanced down-conversion of photons emitted by photo-excited $Y_{2-x}Er_xSi_2O_7$ films grown on Silicon.*
  M. Miritello, R. Lo Savio, **P. Cardile** and F. Priolo.
  Physical Review B **81**, 041411R (2010)

- *Er^{3+} excitation and upconversion processes in $Y_{2-x}Er_xSi_2O_7$ films for planar optical amplifiers.*
  M. Miritello, R. Lo Savio, **P. Cardile** and F. Priolo.
  Proceedings of the 6th IEEE Conference on Group IV Photonics (2009)

Other publications:

- *Erbium-Oxygen interactions in crystalline Silicon.*
  G. Franzò, E. Napolitani, **P. Cardile**, S. Boninelli, A. Marino and F. Priolo.
  Semiconductor Science and Technology **26**, 055002 (2011).

- *Concentration dependence of the Er^{3+} visible and infrared luminescence in $Y_{2-x}Er_xO_3$ thin films on Si.*
  R. Lo Savio, M. Miritello, **P. Cardile** and F. Priolo.
  Journal of Applied Physics **106**, 043512 (2009).

Acknowledgements

One can think that after concluding the writing of scientific content of the PhD thesis, most of the job is done. It’s not true, because something very important is missing: the “Acknowledgements” section. Here I need to thank all the people that, in many ways and in many places, helped me in this three years long work.

First of all, I would like to express my sincere gratitude to my tutor, Prof. Francesco Priolo, a true guide for me in the research field of Silicon Photonics. He gave me the possibility to work in his group and to be active part of an important European project. His precious suggestions and help really let me grow and become a scientist. I am not able to put in words how much I am grateful to Maria and Roberto. They taught me from the beginning how to behave in an experimental lab and I am really proud today to be part of the same team. Thanks for the friendship they demonstrated me. Many thanks to Alessia, for her advices, availability and kindness. I am happy to have started to study something “new”, together with her expertise.

I would like to sincerely acknowledge all the colleagues close to me, in particular thanks to Egidio and Giorgia: we were student together, we are “workers” now. We passed through examinations, degrees, seminars, conferences all together. *Ad maiora*!

A special acknowledge is due to Ciambra and Ciccio, for their friendship, the discussions about everything, especially football, fantasy football, politics, economy and travels. I am extremely grateful to Emanuele, for his affection, his suggestions, his kindness. Italy usually loses the best people.

Thanks to Alessandro, Antonio, Federico, Roberta and Salvo C., for all the discussions, the meetings, the spirit of initiative and their friendship. I am grateful to Pietro and Gabriele, for sharing the office, the keys and new ideas in photonics.

I want to thank also the Scuola Superiore di Catania. In particular I am grateful to the coordinators of my PhD course, Prof. Rimini, Prof. Grimaldi and Dr. Raineri and all the "Nanoscience" colleagues.

Thanks to Dr. Privitera for his capability to attract trust and confidence, Dr. Iacona and Dr. Franzò for the scientific discussions, and to all the other people in MATIS: Prof. Terrasi, Lucia, Simona (especially for the last-minute TEM images reported in this thesis!), Elena, Francesco, Giuliana, Isodiana, Salvo M., Salvo C., Sewerin and Stefano. Many thanks to Daniele and Salvo B., for their sympathy and the volleyball matches at CUS.

I would like to acknowledge also Dario, Matteo, Simone and Prof. Andreani, for their added-value in photonics, for their kind hospitality whenever it's time to go to Pavia, and for the μPL and RS measurements regarding the big device we obtained and the simulations reported in the thesis.

During my PhD course, I spent a wonderful period in St. Andrews, in Scotland. I lived there and worked in the "Microphotonics and Photonic Crystals Group" for ten months, under the supervision of Prof. Thomas Krauss. I would like to thank him, first of all, because he welcomed me, giving me the occasion to meet many special people. In particular I want to acknowledge Will, for his constant support in the clean room, for all the scientific discussions and for being always helpful. Then I would like to thank Armando. He demonstrated me how peculiar are our Italian roots, even just after a lunch break. Many thanks to all the colleagues I found there: Abdul, Andrea, Anna Chiara, Annette, Chris, Damiano, Dong, Doughlas, Emiliano, Gil, Kapil, Karl, Isabella, Li, Lucia, Marcel, Marcello, Mark, Ronan, Salvatore, Sebastian K., Sebastian S., Shu, Tim. It has been a

pleasure to share with them the office, the labs, the drawers of the clean room, all the coffee breaks at 11 am and 4 pm, the football matches at the Sports Center, and the seats at the Whey Pat for the group beer! And I am particularly thankful to my flatmates, Davo, Martin and Walshy. Though I was far away from Italy, they really made me feel at home. Thanks also to their girlfriends Magda, Liz and Willemijn, for the wonderful dinners spent all together.

Then I acknowledge Carmelo Percolla, Salvo Tatì, Giuseppe Pantè, Steve Balfour and George Robb for their technical support, both in Catania and in St. Andrews.

I would also thank Laura and Aldo, for their friendship and the spare time spent together, Diego, for his affection and kindness, and Alessio M., Alessio S. and Enzo, for the weekly appointment with Risk.

The last lines are usually dedicated to the relatives. The reason lies probably in the fact that their importance is almost obvious. Thanks to my grandparents, my parents and all my sisters, for demonstrating me every day that we are a nonpareil family. I acknowledge the whole Rachele’s family. They supported me in many cases, with their affection and exceptional bounty.

Finally I haven’t enough words to thank my beloved girlfriend and FW, Rachele. I can just say that your invaluable Love is (and is going to be) my strength in every second of my life.